Electronic Supplementary Material (ESI) for Dalton Transactions.
This journal is © The Royal Society of Chemistry 2024

Supporting Information
for
Adsorbents for Hydrogen-Bond Accepting Hazardous Chemicals by Post-Synthetic Modification of UiO-66-NH_2

Daniel A. Corbin,[a] Michael R. Papantonakis,[b] Viet K. Nguyen,[b] Christopher J. Breshike,[b,*] R. Andrew McGill[b]

[a] National Research Council Research Associateship Program, Washington, DC 20375
[b] Materials and Sensors Section, US Naval Research Laboratory, 4555 Overlook Ave SW, Washington, DC 20375
*Corresponding author, e-mail: christopher.breshike@nrl.navy.mil

Distribution Statement A: Approved for public release. Distribution is unlimited.

Table of Contents

1. Materials and Methods 3

Purchased Chemicals 3

Instrumentation 3

2. Procedures 4

MOF Syntheses 4

Details for Individual MOF Functionalization Reactions 4

3. Characterization of Functionalized MOFs 9

FT-IR Spectroscopy 9

NMR Spectroscopy of Digested MOF Linkers 17

*UV-Vis of **A1** – **A6** Suspensions* 36

Synthesis and Characterization of an Imine Small Molecule Analogue 37

*Reduction of Imine **I6** with Sodium Borohydride* 41

Powder X-Ray Diffraction 44

Thermogravimetric Analysis 46

Surface Area Measurement Nitrogen Gas Adsorption 54

Measurement of DMMP Uptake Capacity 72

Measurement of Henry's Law Binding Constants 82

4. References 97

1. Materials and Methods

Purchased Chemicals

The following chemicals were purchased from Sigma-Aldrich: zirconium(IV) chloride, terephthalic acid, 2-hydroxy-1,4-benzenedicarboxylic acid, 2-amino-1,4-benzenedicarboxylic acid, *N,N*-dimethylformamide, methanol, toluene, 4-hydroxybenzaldehyde, 3-fluoro-4-hydroxybenzaldehyde, 2-methoxy-4-hydroxybenzaldehyde, 3-trifluoromethyl-4-hydroxybenzaldehyde, 3-methoxy-4-hydroxybenzaldehyde, 4-hydroxybenzoic acid, 3-fluoro-4-hydroxybenzoic acid, 3-methoxy-4-hydroxybenzoic acid, sodium borohydride, and dimethyl methylphosphonate (DMMP). 3-Trifluoromethyl-4-hydroxybenzoic acid, 2,3,5,6-tetrafluoro-4-hydroxybenzoic acid, 2-fluoro-4-hydroxybenzoic acid, 2-fluoro-4-hydroxybenzaldehyde, and 2-trifluoromethyl-4-hydroxybenzaldehyde were purchased from Ambeed. Deuterium oxide for was obtained from Cambridge Isotopes. Ethanol (200 proof) was purchased from the Warner-Graham company. Concentrated hydrochloric acid was obtained from Fisher Chemical. Sodium bicarbonate was obtained from Oakwood Chemical, and Ultra High Purity Nitrogen (UN1066) was purchased from Matheson Tri-Gas.

Instrumentation

Infrared (IR) spectroscopy was performed on a Bruker Vertex 80v FT-IR spectrometer with a PIKE Technologies MIRacle Single Reflection attenuated total reflectance (ATR) attachment equipped with a ZnSe crystal. Spectra were collected under vacuum and background corrected. Nuclear magnetic resonance (NMR) spectra were collected on a Bruker Ascend spectrometer (400 MHz) and are reported in parts per million (ppm, δ). ^{1}H NMR spectra are referenced to the residual solvent peak at 4.79 ppm for D_2O. ^{19}F NMR spectra were also collected in D_2O but are not referenced to a certain peak. Powder x-ray diffraction data was collected on a Rigaku SmartLab powder diffraction system equipped with a D/tex ultra 1D detector and a Cu x-ray source using a Bragg-Brentano geometry.

Thermogravimetric analysis (TGA) was performed on a Netzsch STA 449 F1 Jupiter in a flowing Ar atmosphere (15 mL min^{-1}). The approximate sample weight was 10 mg in all experiments and the heating rate was 5 °C min^{-1}. Nitrogen gas adsorption measurements were performed on a Micromeritics Tristar II Plus at 77K. Samples were activated prior to measurement on a Micromeritics Smart VacPrep system by heating at 200 °C under vacuum for 8h. Vapor uptake studies were performed using a Biolin Scientific QSense Analyzer quartz crystal microbalance (QCM) and a custom NRL developed vapor generation system. Details related to vapor generation are provided in each section describing QCM experiments.

2. Procedures

MOF Syntheses

Synthesis of Zirconium 1,4-benzenedicarboxylate MOF (UiO-66). UiO-66 was synthesized according to a published literature procedure.[1]

Synthesis of Zirconium 2-hydroxy-1,4-benzenedicarboxylate MOF (UiO-66-OH). UiO-66 was synthesized according to a published literature procedure.[1]

Synthesis of Zirconium 2-amino-1,4-benzenedicarboxylate MOF (UiO-66-NH_2). UiO-66 was synthesized according to a published literature procedure.[1]

Details for Individual MOF Functionalization Reactions

All MOF functionalization reactions were performed according to modified literature procedures.[2–4]

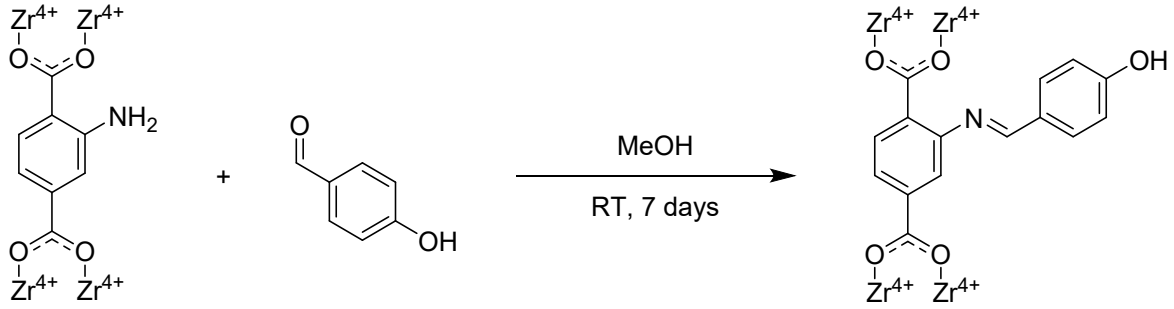

UiO-66-NH_2 **I1**

Functionalization with 4-Hydroxybenzaldehyde (I1). UiO-66-NH_2 (208.8 mg, 0.714 mmol, 1 eq) was reacted with 4-hydroxybenzaldehyde (174.6 mg, 1.43 mmol, 2 eq). The product was a dark yellow / light orange powder (yield = 0.1979 g). After initial purification, soaking overnight in methanol was necessary to remove residual 4-hydroxybenzalehyde.

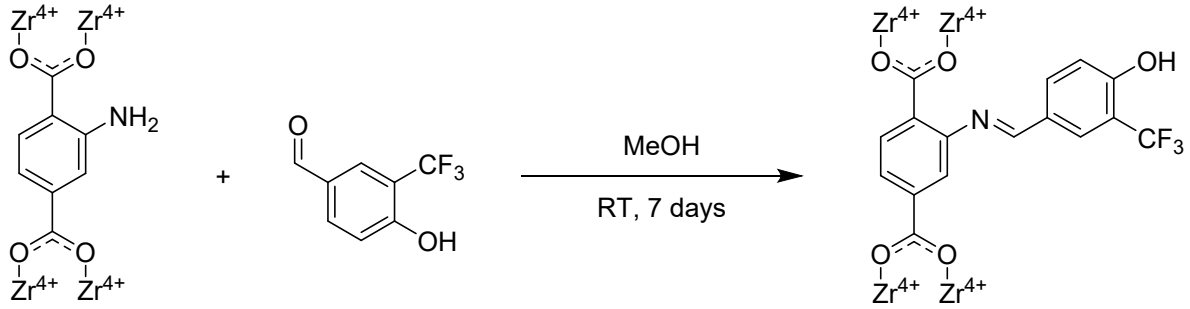

UiO-66-NH_2 **I2**

Functionalization with 3-Trifluoromethyl-4-hydroxybenzaldehyde (I2). UiO-66-NH_2 (177.3 mg, 0.606 mmol, 1 eq) was reacted with 3-trifluoromethyl-4-hydroxybenzaldehyde (210.3 mg, 1.11 mmol, 2 eq). The product was a dark yellow / light orange powder (yield = 0.1666 g). After

initial purification, soaking overnight in methanol was necessary to remove residual 3-trifluoromethyl-4-hydroxybenzalehyde.

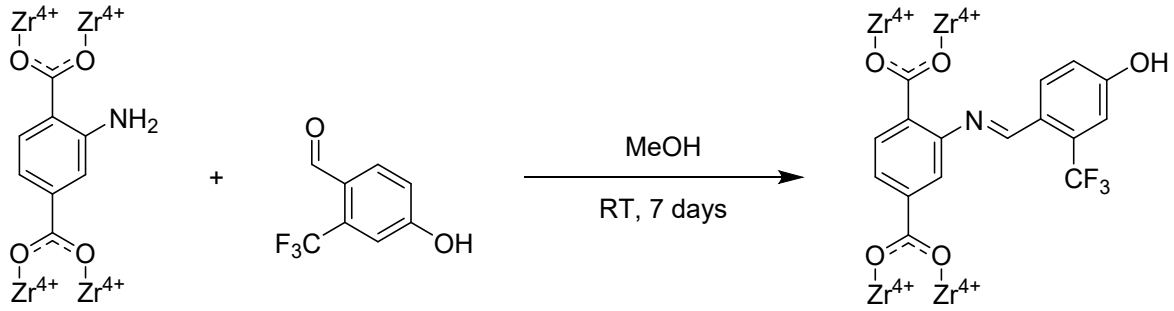

UiO-66-NH$_2$ **I3**

Functionalization with 2-Trifluoromethyl-4-hydroxybenzaldehyde (I3). UiO-66-NH$_2$ (156.4 mg, 0.535 mmol, 1 eq) was reacted with 2-trifluoromethyl-4-hydroxybenzaldehyde (199.4 mg, 1.05 mmol, 2 eq). The product was a dark yellow / light orange powder (yield = 0.1546 g). After initial washing, no further purification was needed.

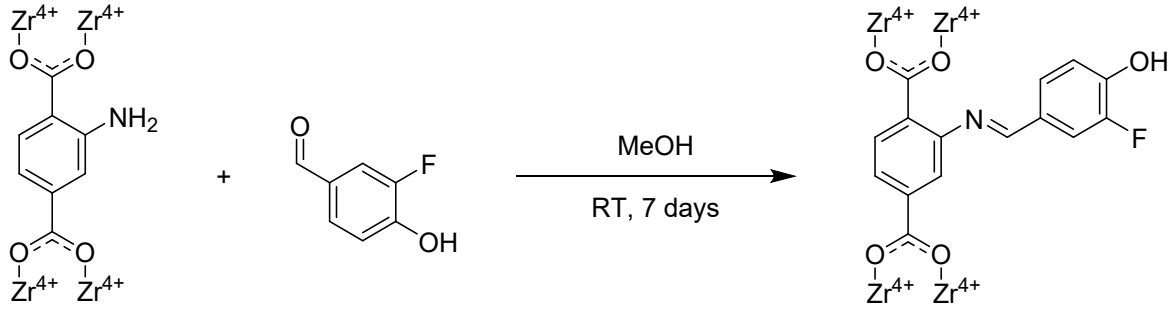

UiO-66-NH$_2$ **I4**

Functionalization with 3-Fluoro-4-hydroxybenzaldehyde (I4). UiO-66-NH$_2$ (199.9 mg, 0.684 mmol, 1 eq) was reacted with 3-fluoro-4-hydroxybenzaldehyde (198.9 mg, 1.42 mmol, 2 eq). The product was a dark yellow / light orange powder (yield = 0.1923 g). After initial purification, no further purification was needed.

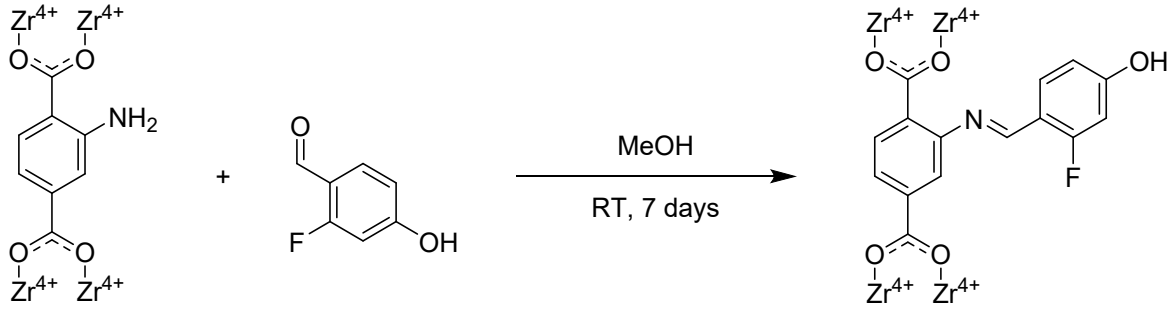

UiO-66-NH$_2$ **I5**

Functionalization with 2-Fluoro-4-hydroxybenzaldehyde (I5). UiO-66-NH$_2$ (200 mg, 0.684 mmol, 1 eq) was reacted with 2-fluoro-4-hydroxybenzaldehyde (196.3 mg, 1.40 mmol, 2 eq). The

product was a dark yellow / light orange powder (yield = 0.1992 g). After initial purification, no further purification was needed.

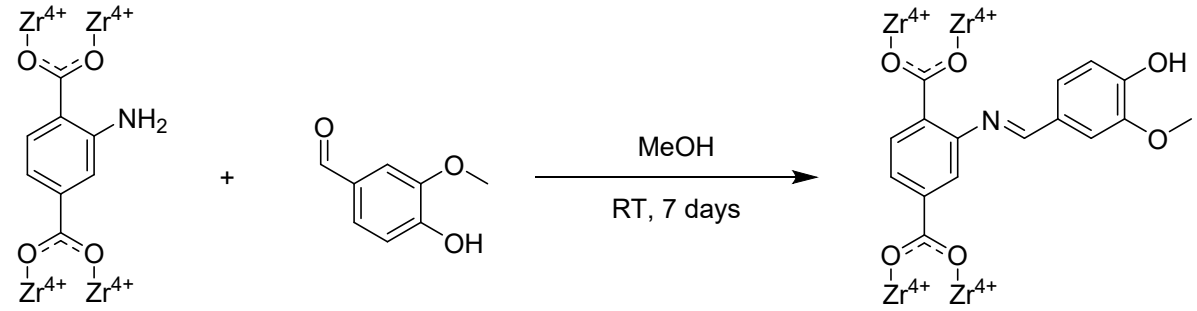

UiO-66-NH$_2$ **I6**

Functionalization with 3-Methoxy-4-hydroxybenzaldehyde (I6). UiO-66-NH$_2$ (200 mg, 0.684 mmol, 1 eq) was reacted with 3-methoxy-4-hydroxybenzaldehyde (212.0 mg, 1.39 mmol, 2 eq). The product was a dark yellow / light orange powder (yield = 0.1792 g). After initial washing, no further purification was needed.

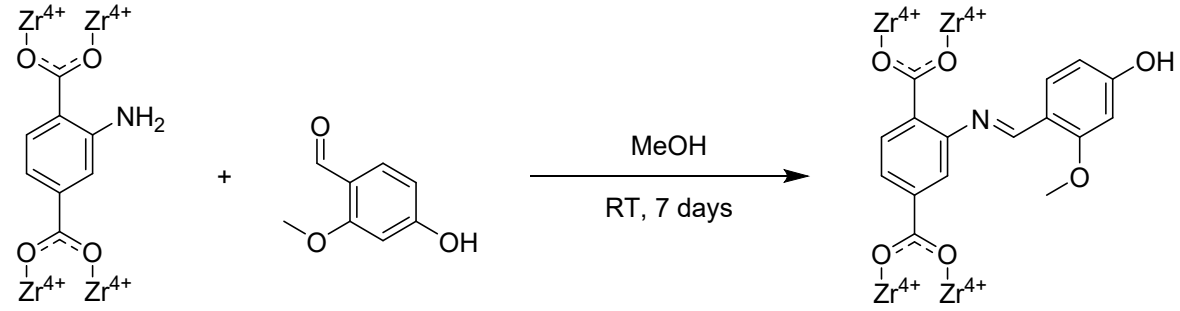

UiO-66-NH$_2$ **I7**

Functionalization with 2-Methoxy-4-hydroxybenzaldehyde (I7). UiO-66-NH$_2$ (196.8 mg, 0.673 mmol, 1 eq) was reacted with 2-methoxy-4-hydroxybenzaldehyde (209.7 mg, 1.38 mmol, 2 eq). The product was a dark yellow / light orange powder (yield = 0.2066 g). After initial purification, soaking overnight in methanol was necessary to remove residual 2-methoxy-4-hydroxybenzalehyde.

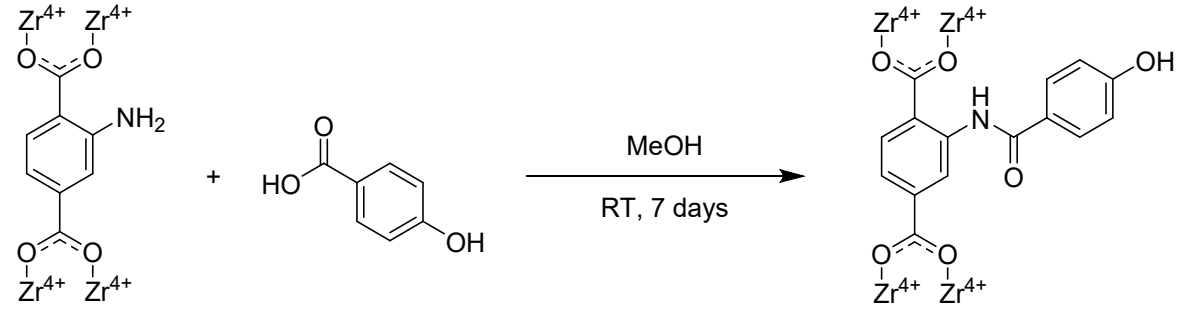

UiO-66-NH$_2$ **A1**

Functionalization with 4-Hydroxybenzoic Acid (A1). UiO-66-NH_2 (198.1 mg, 0.678 mmol, 1 eq) was reacted with 4-hydroxybenzoic acid (187.0 mg, 1.35 mmol, 2 eq). The product was a light yellow powder (yield = 0.1851 g). After initial purification, soaking overnight in methanol was necessary to remove residual 4-hydroxybenzoic acid.

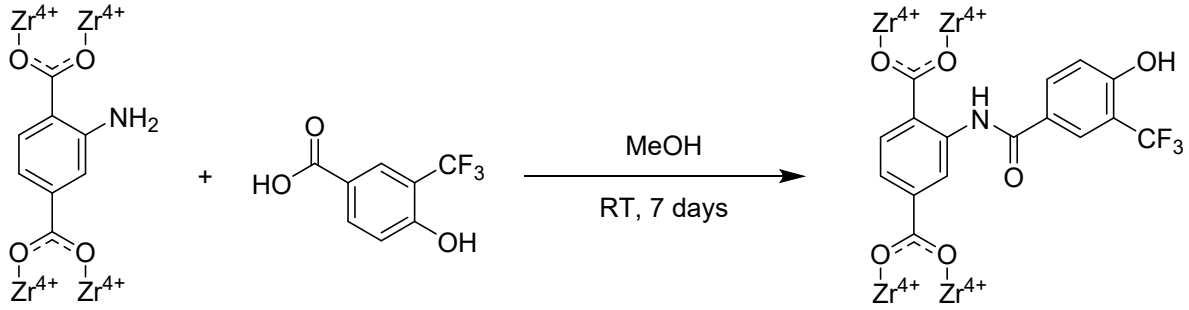

UiO-66-NH_2 **A2**

Functionalization with 3-Trifluoromethyl-4-hydroxybenzoic Acid (A2). UiO-66-NH_2 (201.0 mg, 0.687 mmol, 1 eq) was reacted with 3-trifluoromethyl-4-hydroxybenzoic acid (284.8 mg, 1.38 mmol, 2 eq). The product was a light yellow powder (yield = 0.1799 g). After initial purification, soaking overnight in methanol was necessary to remove residual 3-trifluoromethyl-4-hydroxybenzoic acid.

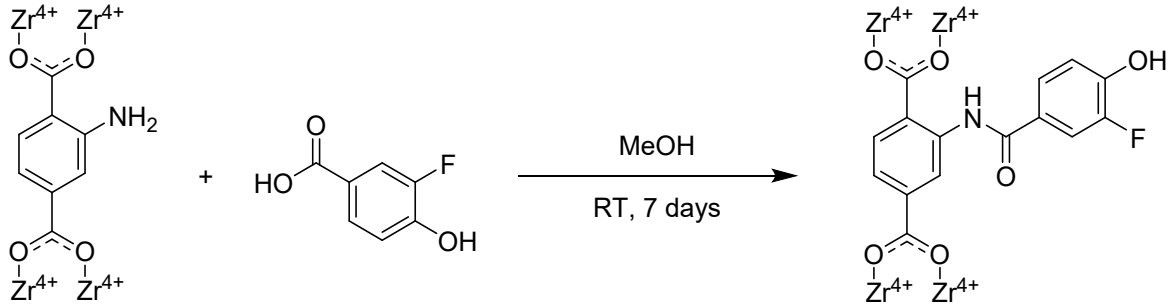

UiO-66-NH_2 **A3**

Functionalization with 3-Fluoro-4-hydroxybenzoic Acid (A3). UiO-66-NH_2 (206.1 mg, 0.705 mmol, 1 eq) was reacted with 3-fluoro-4-hydroxybenzoic acid (212.7 mg, 1.36 mmol, 2 eq). The product was a light yellow powder (yield = 0.1851 g). After initial purification, soaking overnight in methanol was necessary to remove residual 3-fluoro-4-hydroxybenzoic acid.

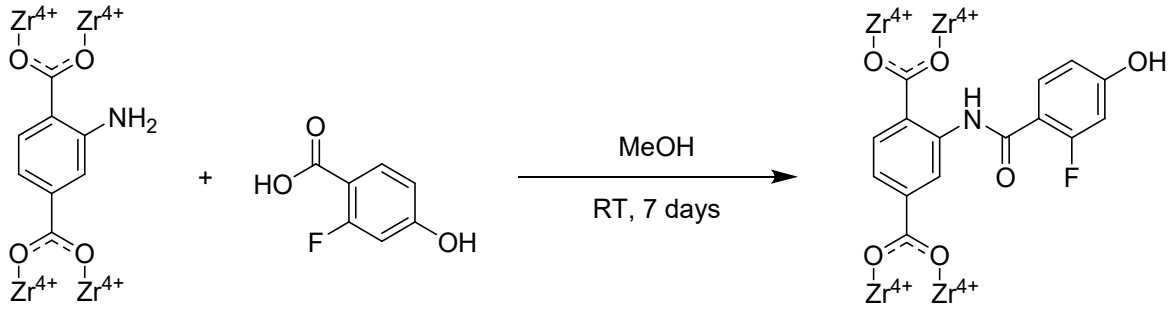

UiO-66-NH_2 **A4**

Functionalization with 2-Fluoro-4-hydroxybenzoic Acid (A4). UiO-66-NH_2 (196.8 mg, 0.673 mmol, 1 eq) was reacted with 2-fluoro-4-hydroxybenzoic acid (232.4 mg, 1.49 mmol, 2 eq). The product was a light yellow powder (yield = 0.1933 g). After initial purification, soaking overnight in methanol was necessary to remove residual 2-fluoro-4-hydroxybenzoic acid.

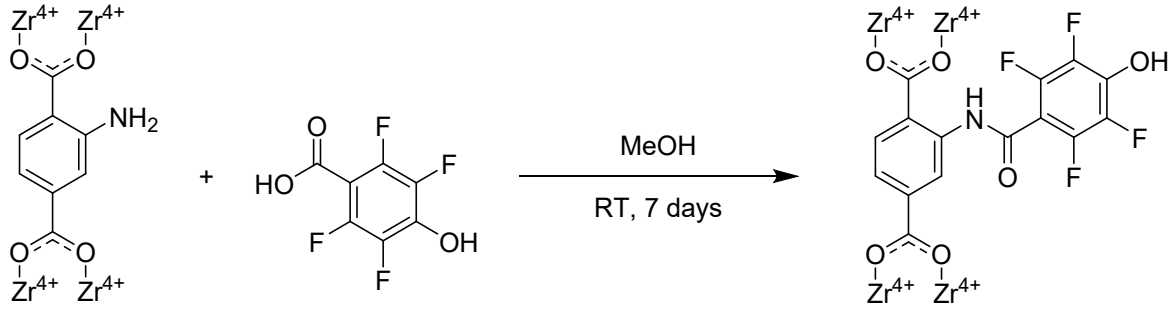

UiO-66-NH_2 **A5**

Functionalization with 2,3,5,6-Tetrafluoro-4-hydroxybenzoic Acid (A5). UiO-66-NH_2 (196.4 mg, 0.672 mmol, 1 eq) was reacted with 2,3,5,6-tetrafluoro-4-hydroxybenzoic acid (303.1 mg, 1.44 mmol, 2 eq). The product was a light yellow powder (yield = 0.2150 g). After initial purification, soaking overnight in methanol was performed to remove possible residual 2,3,5,6-tetrafluoro-4-hydroxybenzoic acid.

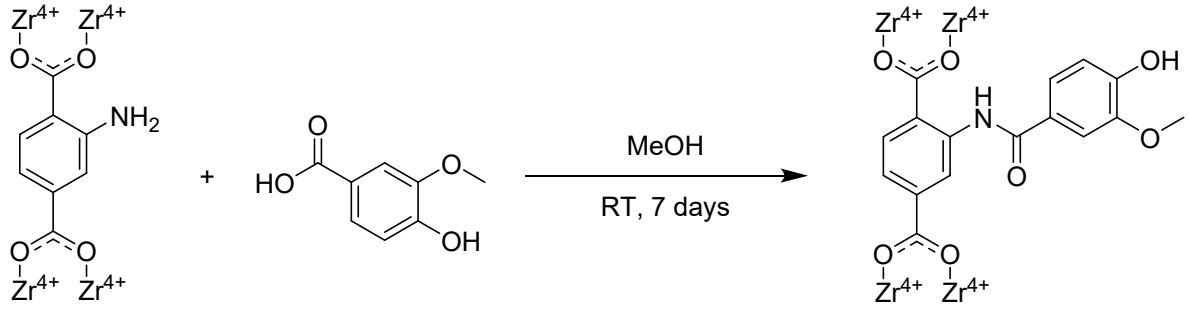

UiO-66-NH_2 **A6**

Functionalization with 3-Methoxy-4-hydroxybenzoic Acid (A6). UiO-66-NH_2 (196.8 mg, 0.673 mmol, 1 eq) was reacted with 3-methoxy-4-hydroxybenzoic acid (229.8 mg, 1.37 mmol, 2 eq). The product was a light yellow powder (yield = 0.1570 g). After initial purification, soaking overnight in methanol was necessary to remove residual 3-methoxy-4-hydroxybenzoic acid.

3. Characterization of Functionalized MOFs

FT-IR Spectroscopy

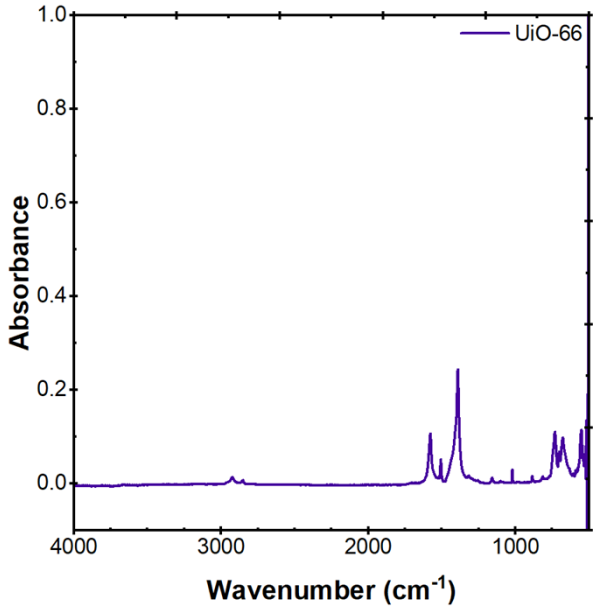

Figure S1. IR spectrum of UiO-66.

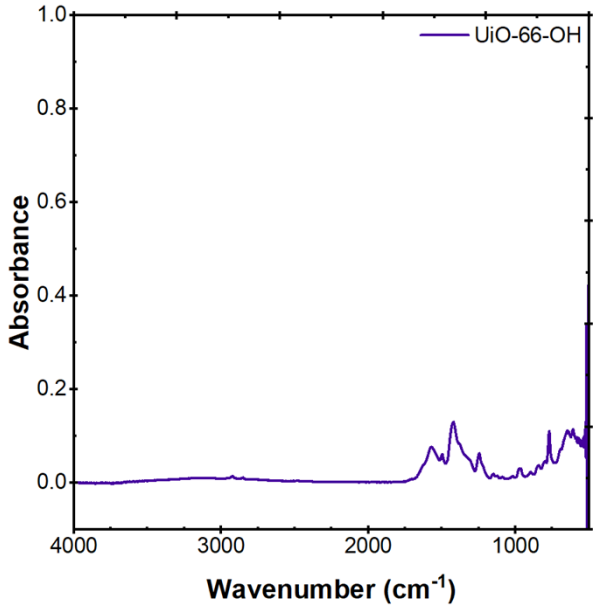

Figure S2. IR spectrum of UiO-66-OH.

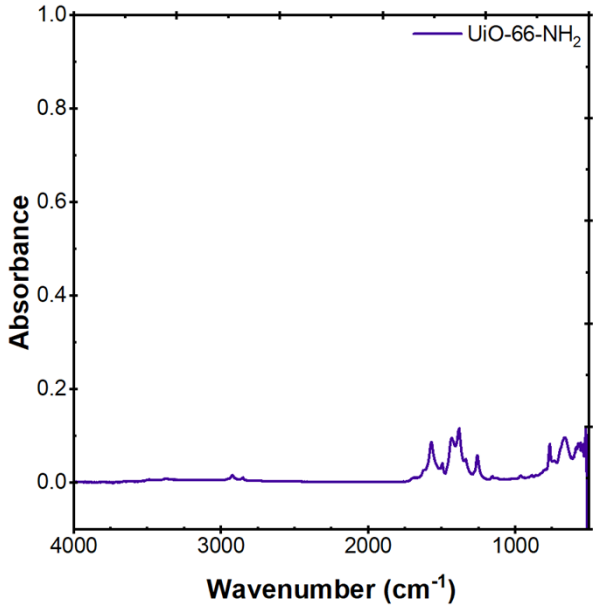

Figure S3. IR spectrum of UiO-66-NH_2.

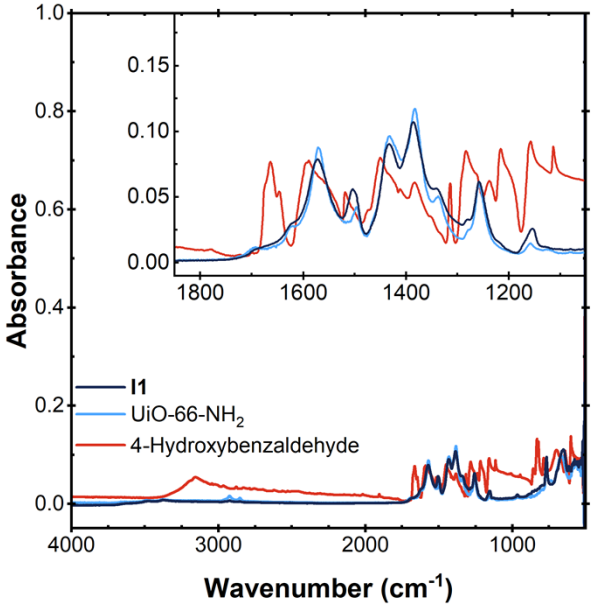

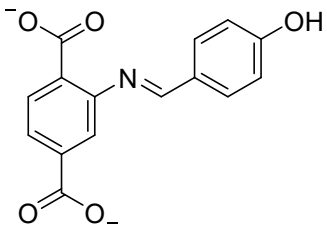

Figure S4. IR spectrum of **I1** (dark purple), UiO-66-NH_2 (light purple), and 3-trifluoromethyl-4-hydroxybenzaldehyde (light pink).

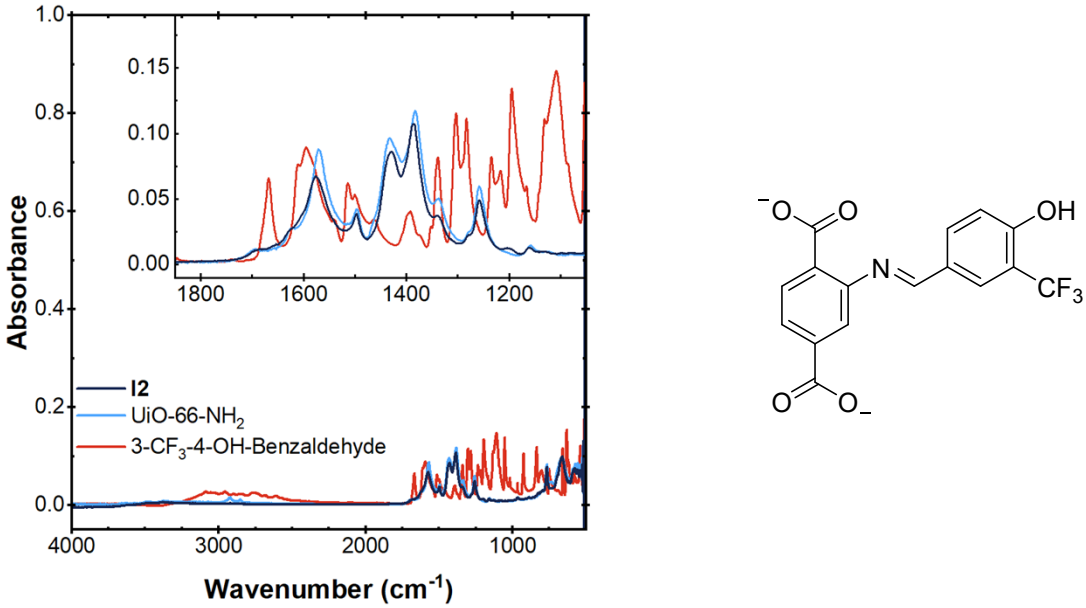

Figure S5. IR spectrum of **I2** (dark purple), UiO-66-NH_2 (light purple), and 3-trifluoromethyl-4-hydroxybenzaldehyde (light pink).

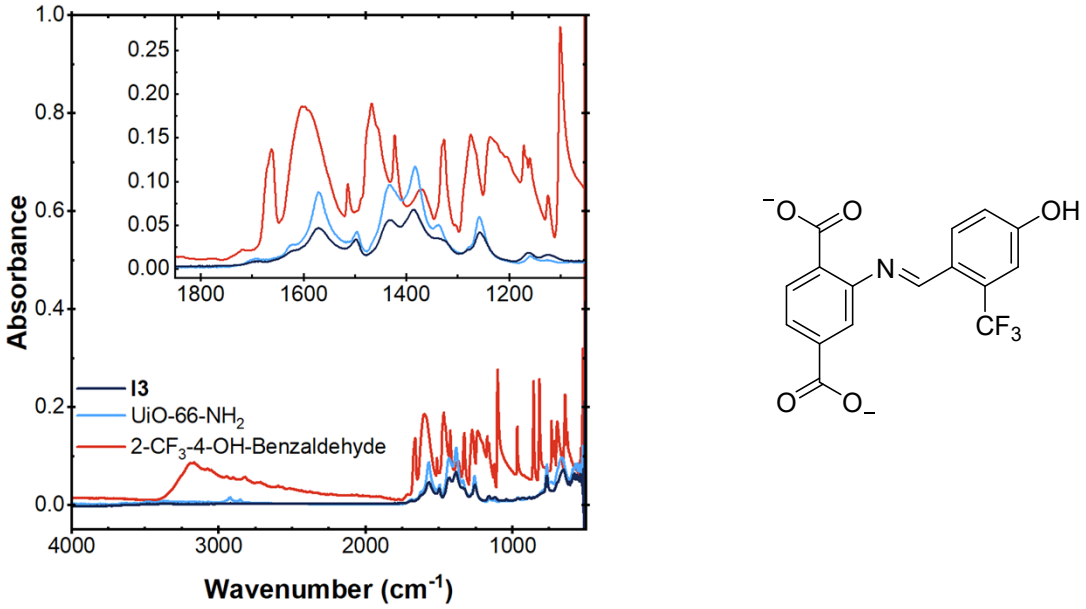

Figure S6. IR spectrum of **I3** (dark purple), UiO-66-NH_2 (light purple), and 2-trifluoromethyl-4-hydroxybenzaldehyde (light pink).

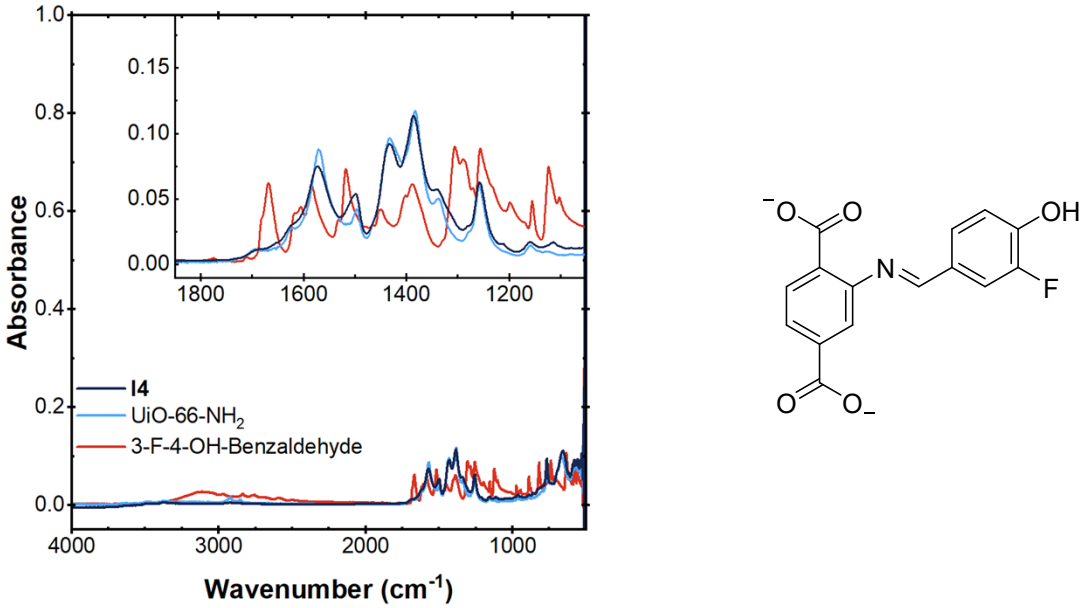

Figure S7. IR spectrum of **I4** (dark purple), UiO-66-NH_2 (light purple), and 3-fluoro-4-hydroxybenzaldehyde (light pink).

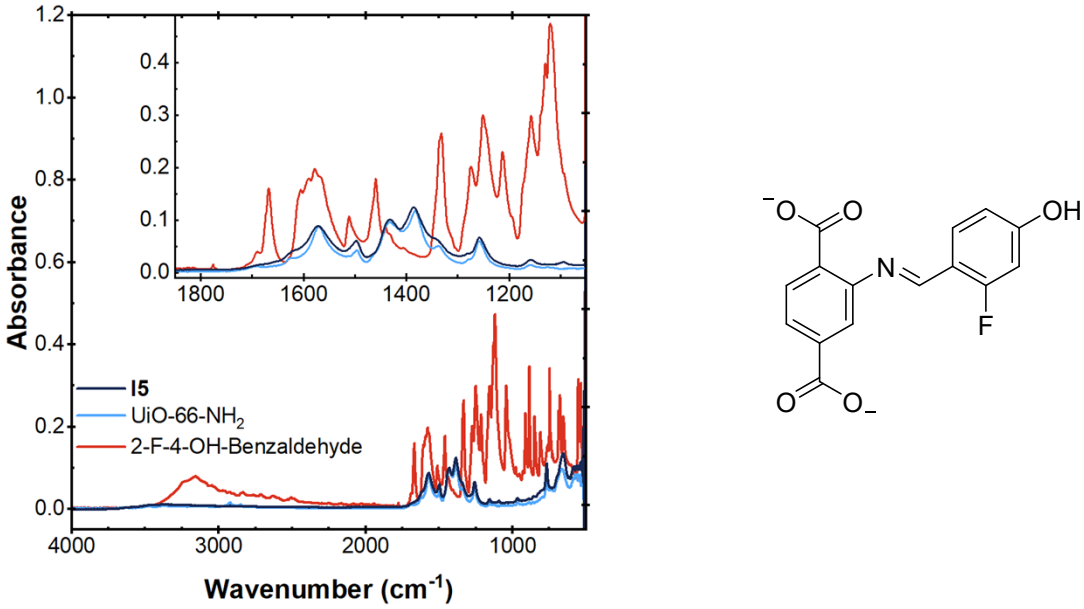

Figure S8. IR spectrum of **I5** (dark purple), UiO-66-NH_2 (light purple), and 2-fluoro-4-hydroxybenzaldehyde (light pink).

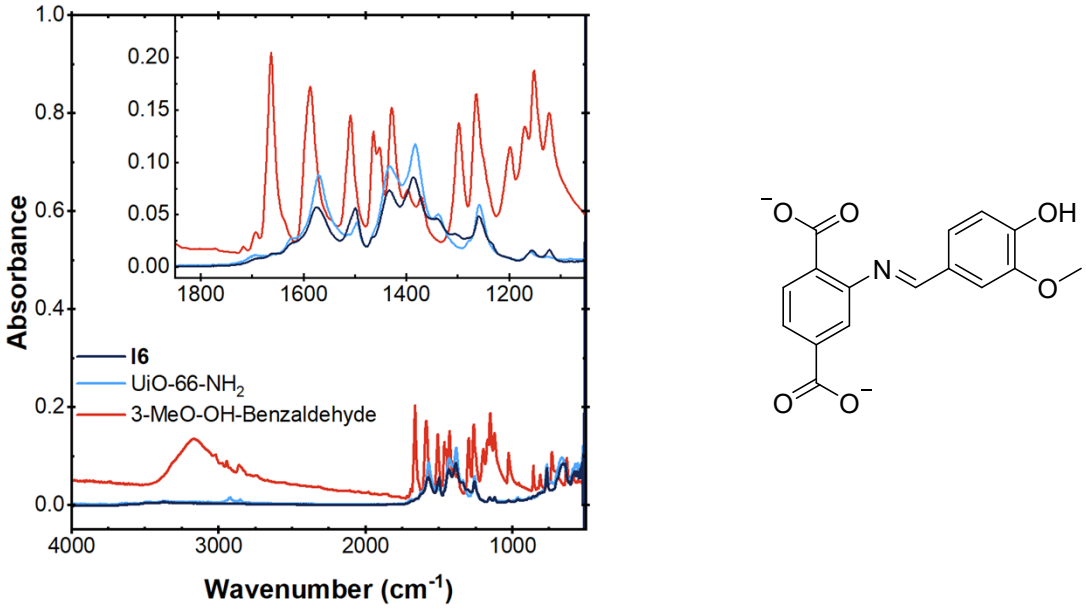

Figure S9. IR spectrum of **I6** (dark purple), UiO-66-NH_2 (light purple), and 3-methoxy-4-hydroxybenzaldehyde (light pink).

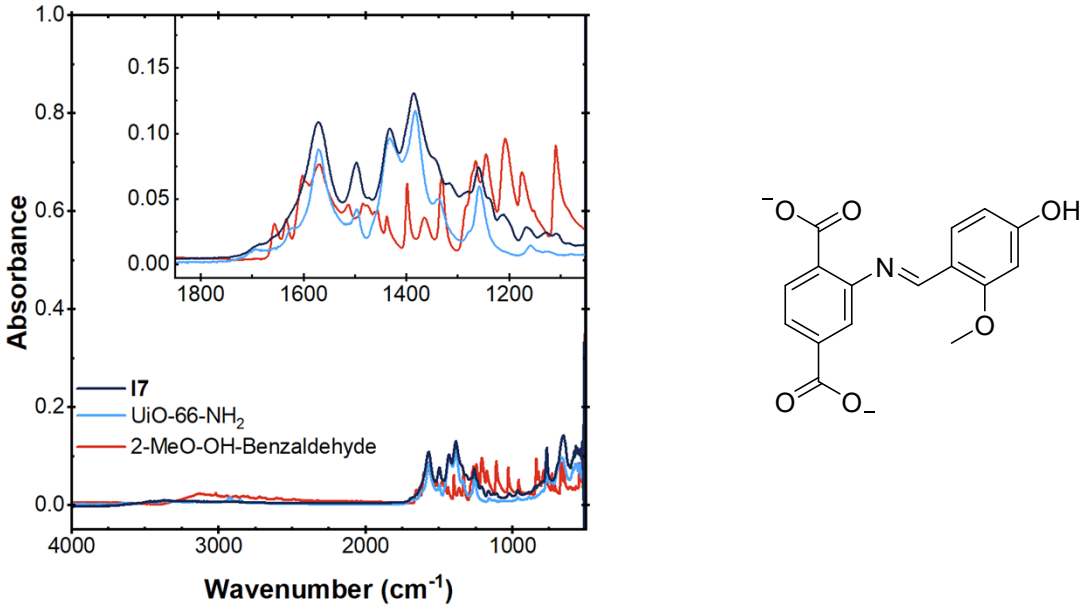

Figure S10. IR spectrum of **I7** (dark purple), UiO-66-NH_2 (light purple), and 2-methoxy-4-hydroxybenzaldehyde (light pink).

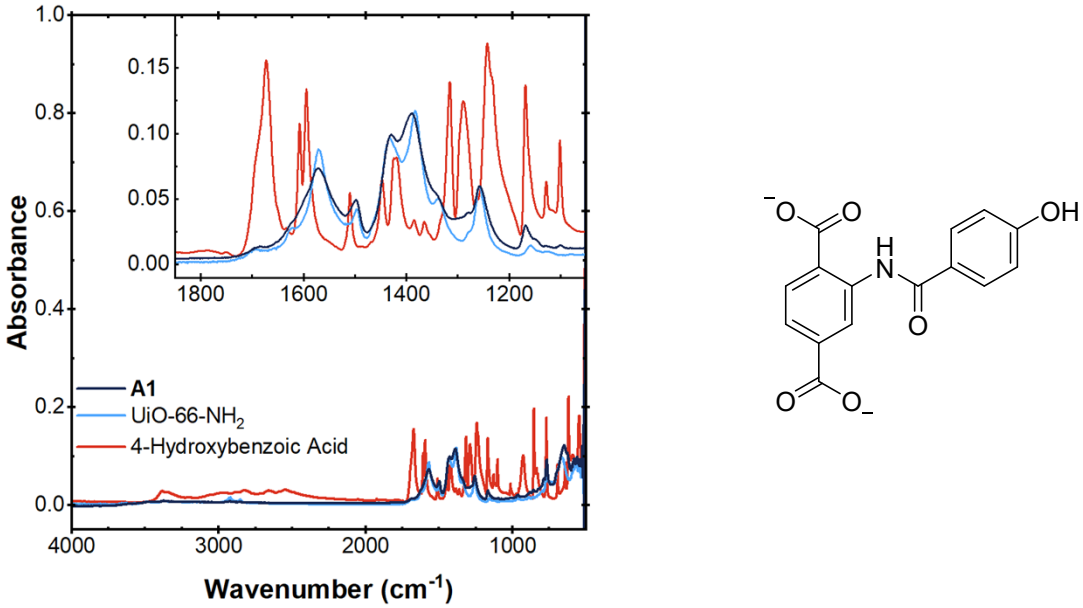

Figure S11. IR spectrum of **A1** (dark purple), UiO-66-NH_2 (light purple), and 4-hydroxybenzoic acid (light pink).

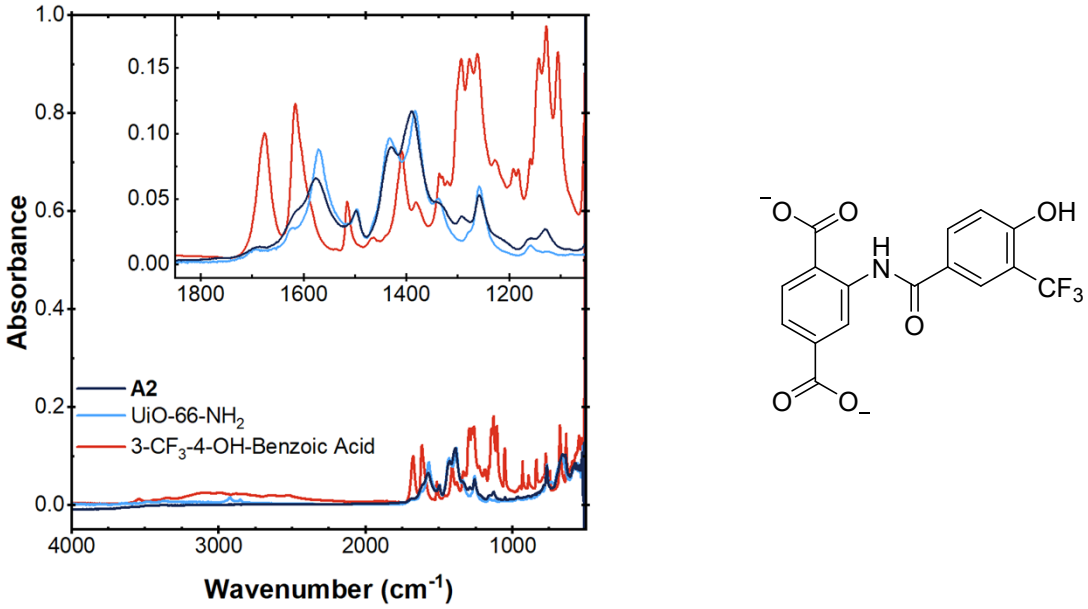

Figure S12. IR spectrum of **A2** (dark purple), UiO-66-NH_2 (light purple), and 3-trifluoromethyl-4-hydroxybenzoic acid (light pink).

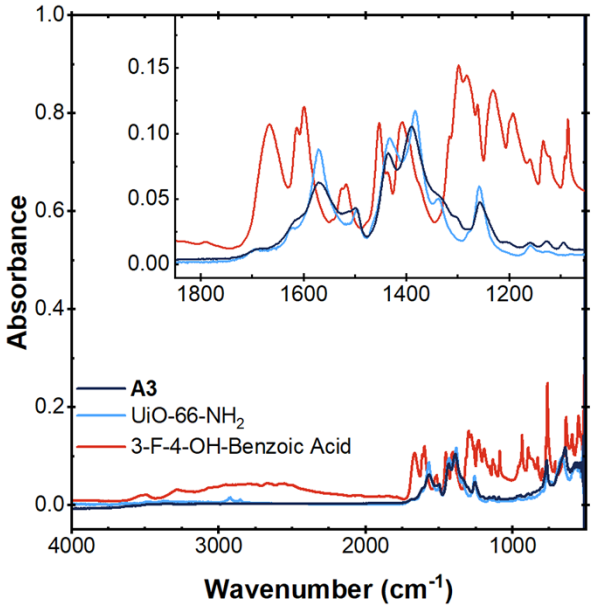

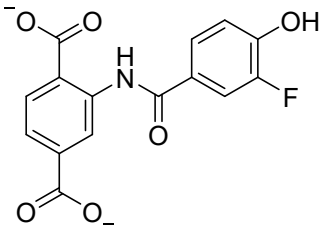

Figure S13. IR spectrum of **A3** (dark purple), UiO-66-NH_2 (light purple), and 3-fluoro-4-hydroxybenzoic acid (light pink).

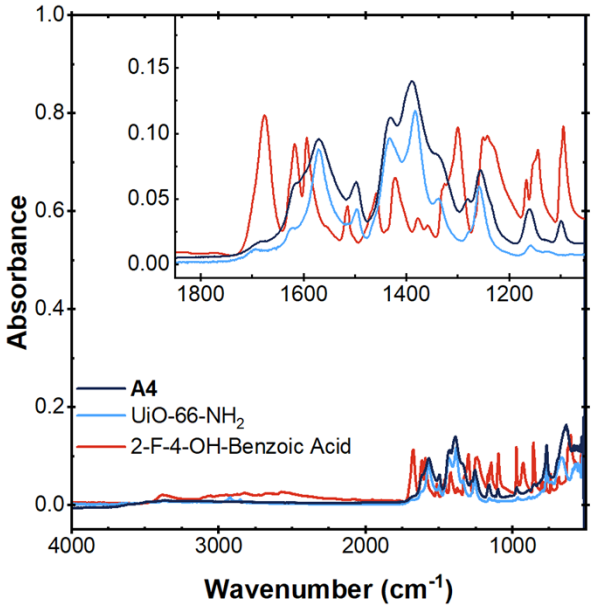

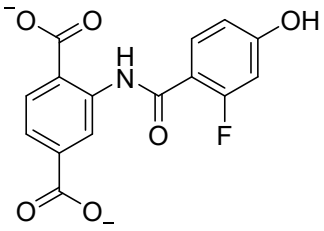

Figure S14. IR spectrum of **A4** (dark purple), UiO-66-NH_2 (light purple), and 2-fluoro-4-hydroxybenzoic acid (light pink).

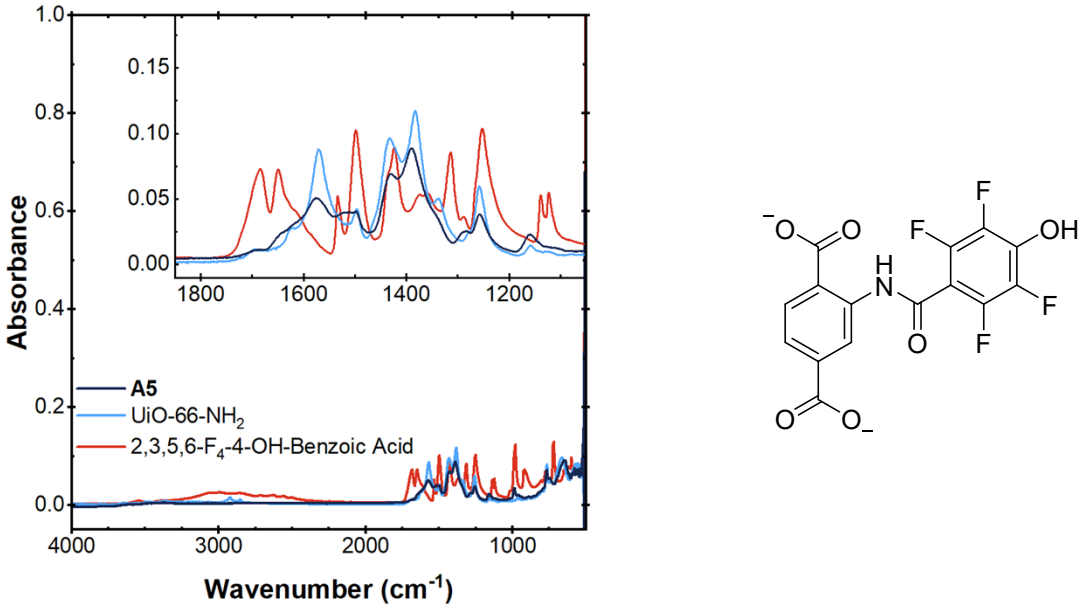

Figure S15. IR spectrum of **A5** (dark purple), UiO-66-NH_2 (light purple), and 2,3,5,6-tetrafluoro-4-hydroxybenzoic acid (light pink).

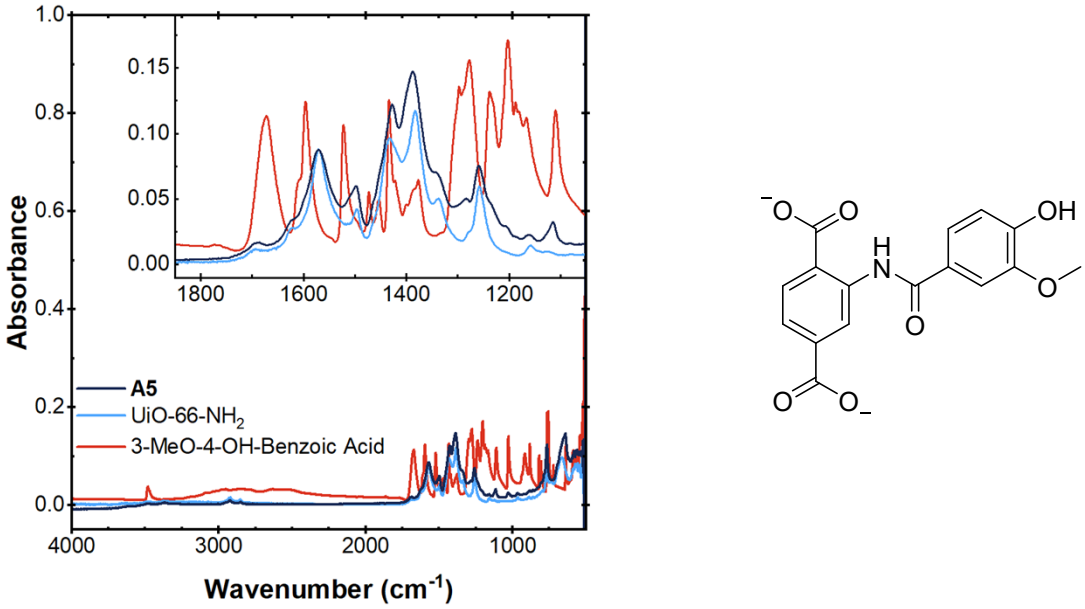

Figure S16. IR spectrum of **A6** (dark purple), UiO-66-NH_2 (light purple), and 3-methoxy-4-hydroxybenzoic acid (light pink).

NMR Spectroscopy of Digested MOF Linkers

Quantification of the degree of functionalization was performed by comparing the relative integrations of the functionalized linkers (determined based on the quantity of aldehyde or benzoic acid observed) to those of the unmodified 2-amino-1,4-benzenedicarboxylate linkers (BDC-NH_2). An example is provided for **I1** to demonstrate the method used.

Importantly, one should note that digestion of the MOF likely also hydrolyzes the functionalized linkers, leading to the formation of the aldehyde or benzoic acid starting material and additional BDC-NH_2. Since quantification relies on the relative quantities of functionalized to unfunctionalized linkers, the formation of this additional BDC-NH_2 could lead to an over-estimation of the quantity of unfunctionalized linkers and thus an under-estimation of the degree of functionalization. Since hydrolysis of the functionalized linkers should produce the aldehyde (or benzoic acid) and BDC-NH_2 in equal quantities, we have corrected for this additional BDC-NH_2 by subtracting the aldehyde (or benzoic acid) integration from the BDC-NH_2 integration prior to determining the degree of functionalization. By doing so, we are only considering the quantity of BDC-NH_2 that was not functionalized. This approach is demonstrated in the example below for **I1** and is similar to that used by Rosi and coworkers.[5]

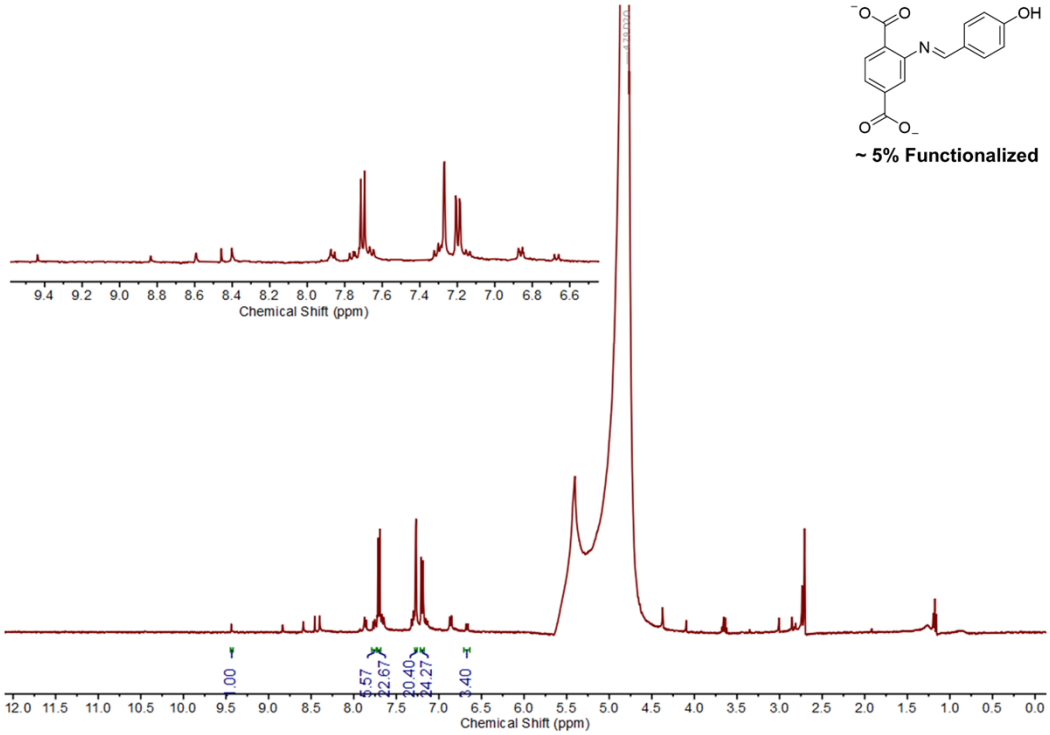

Figure S17. NMR of **I1** digested with saturated $NaHCO_3$ in D_2O showing integration values used to quantify the degree of functionalization.

Aldehyde Integration = 1.00 (9.44 ppm)
BDC-NH_2 Integration = 20.40 (7.27 ppm)

Correcting for BDC-NH_2 that was formed during digestion by hydrolysis of the functionalized linker, we get:

BDC-NH_2 Integration (Corrected) = 20.40 – 1.00 = 19.40

Now we can calculate the degree of functionalization based on the relative integrations above:
Degree of Functionalization = (Aldehyde Integration) / (Aldehyde + BDC-NH_2 Integrations)

Degree of Functionalization = 1.00 / (19.40 + 1.00) = 0.049 or 5%

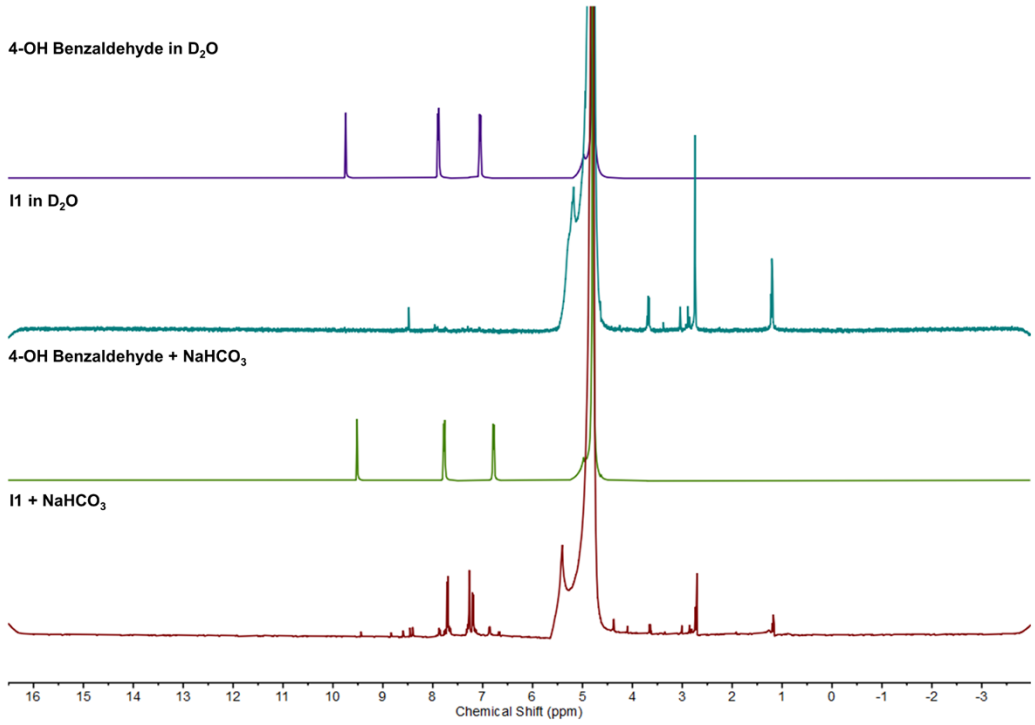

Figure S18. NMR spectra demonstrating the purity of **I1**.

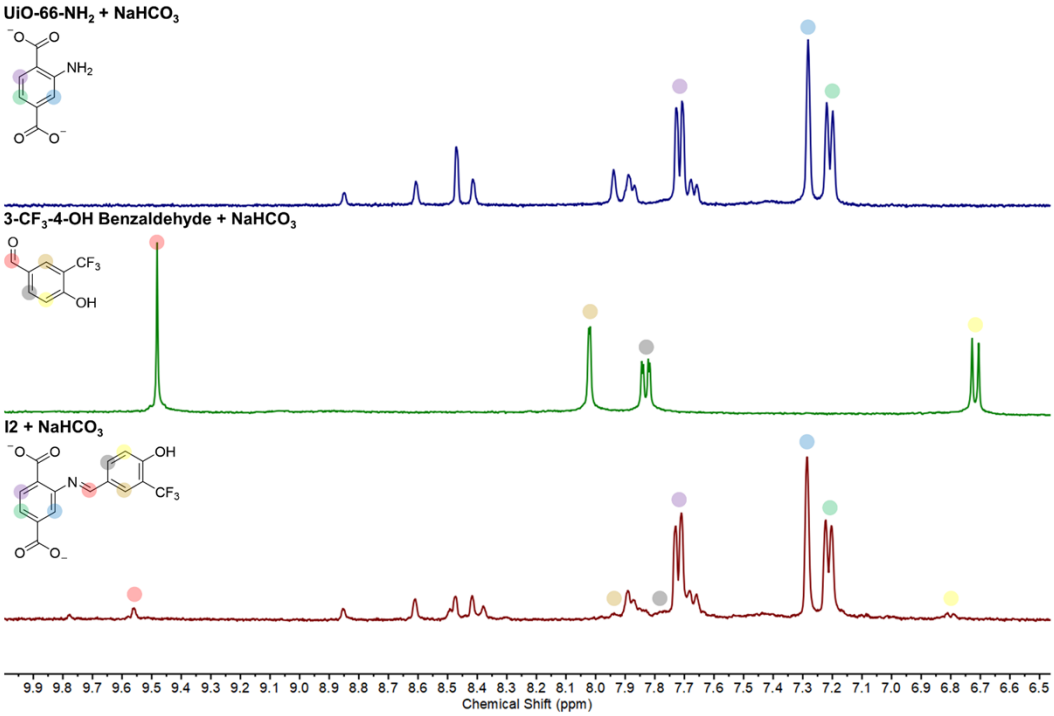

Figure S19. ^{1}H NMR of **I2** digested with saturated $NaHCO_3$ in D_2O (bottom), the corresponding coupling partner in the presence of saturated $NaHCO_3$ in D_2O (middle), and UiO-66-NH_2 digested with saturated $NaHCO_3$ in D_2O (top).

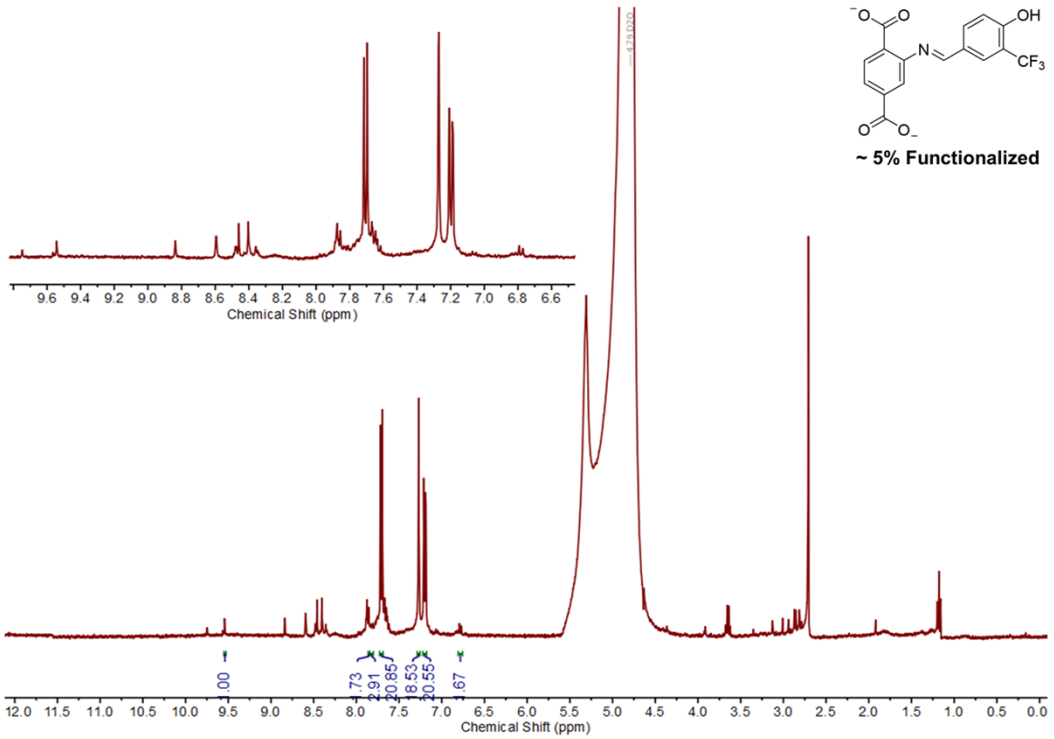

Figure S20. NMR of **I2** digested with saturated $NaHCO_3$ in D_2O showing integration values used to quantify the degree of functionalization.

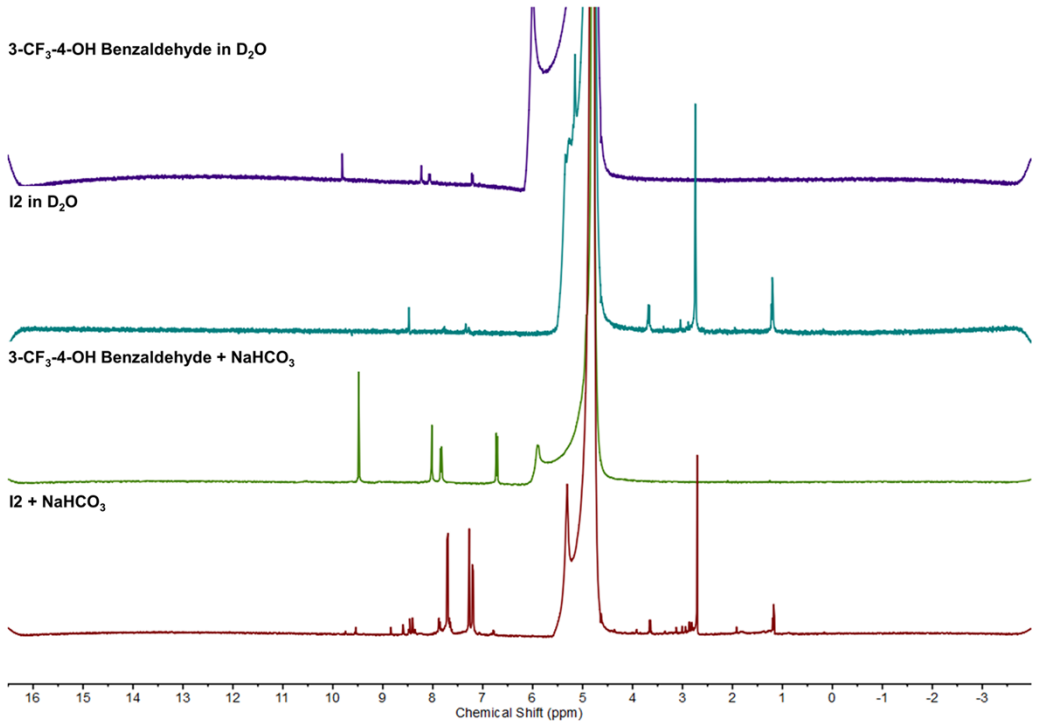

Figure S21. NMR spectra demonstrating the purity of **I2**.

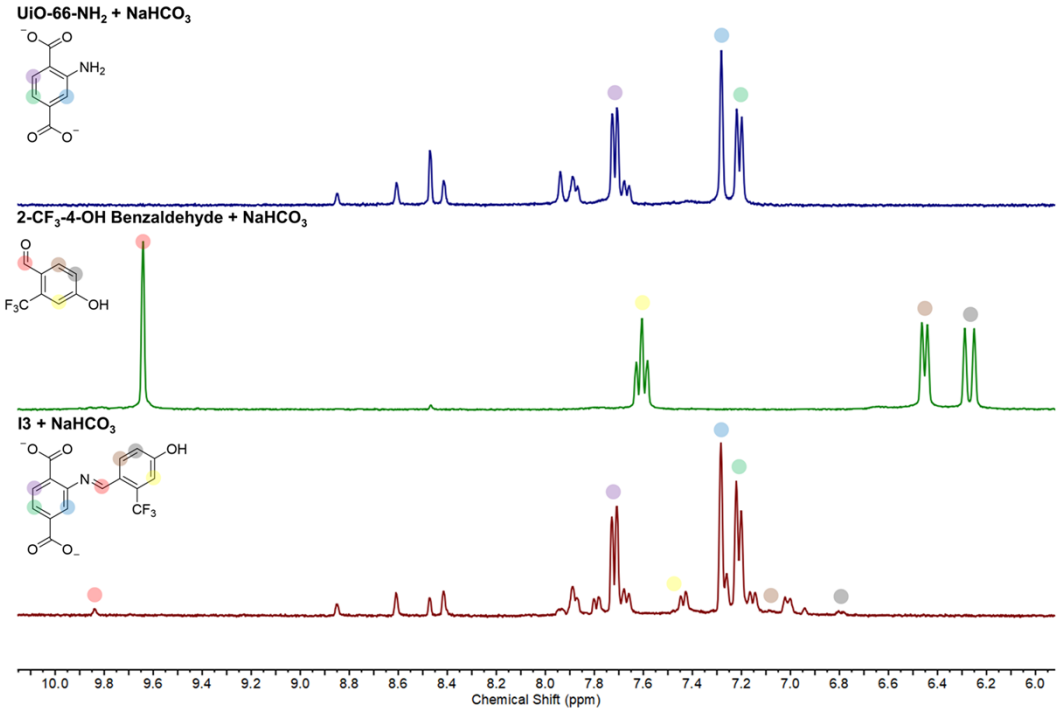

Figure S22. ^{1}H NMR of **I3** digested with saturated $NaHCO_3$ in D_2O (bottom), the corresponding coupling partner in the presence of saturated $NaHCO_3$ in D_2O (middle), and UiO-66-NH_2 digested with saturated $NaHCO_3$ in D_2O (top).

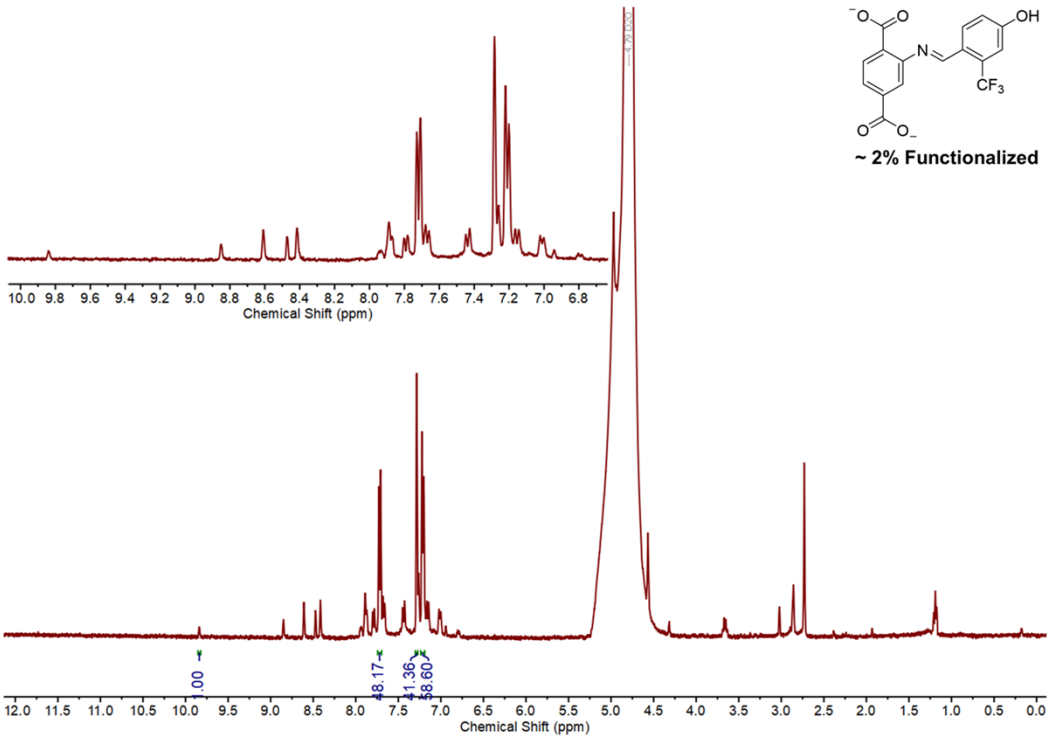

Figure S23. NMR of **I3** digested with saturated $NaHCO_3$ in D_2O showing integration values used to quantify the degree of functionalization.

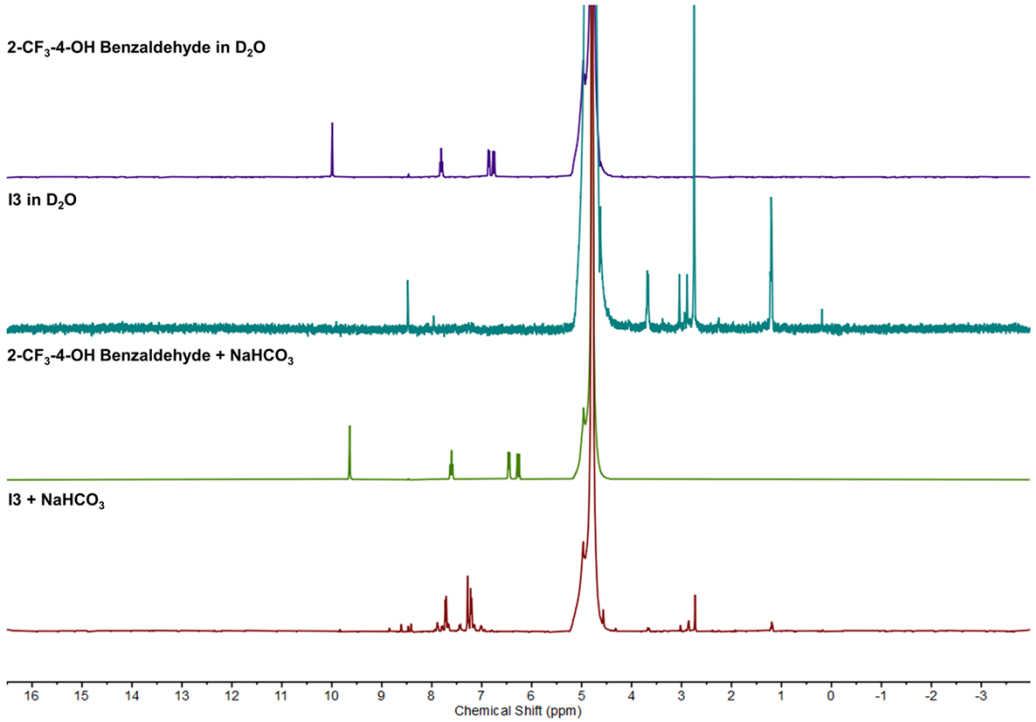

Figure S24. NMR spectra demonstrating the purity of **I3**.

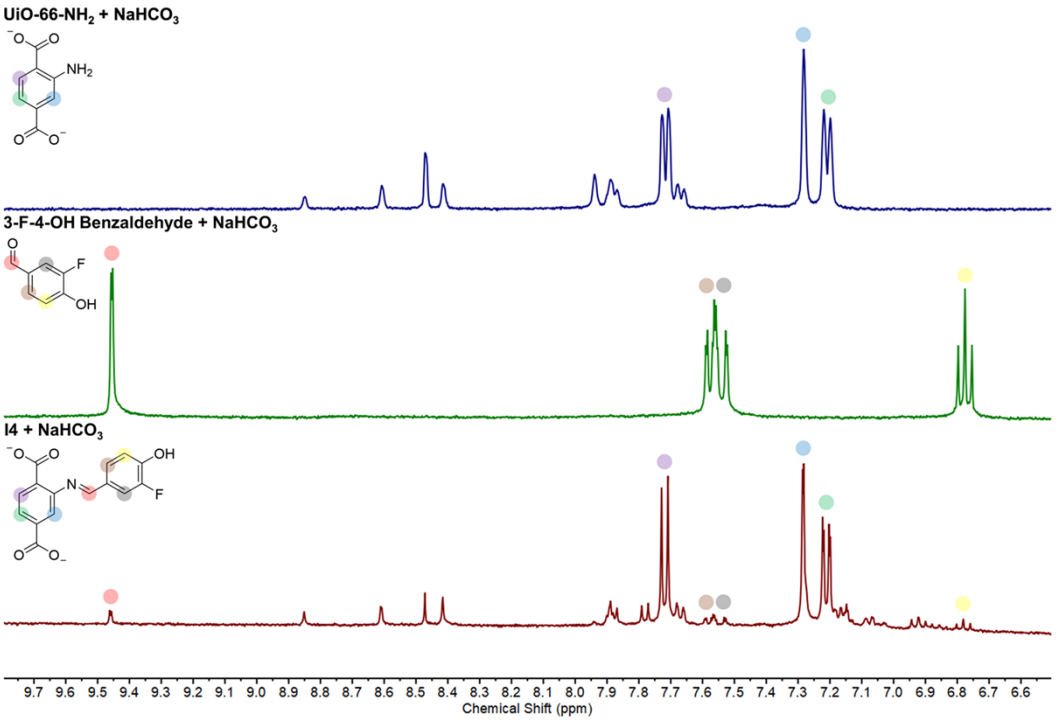

Figure S25. ^{1}H NMR of **I4** digested with saturated $NaHCO_3$ in D_2O (bottom), the corresponding coupling partner in the presence of saturated $NaHCO_3$ in D_2O (middle), and UiO-66-NH_2 digested with saturated $NaHCO_3$ in D_2O (top).

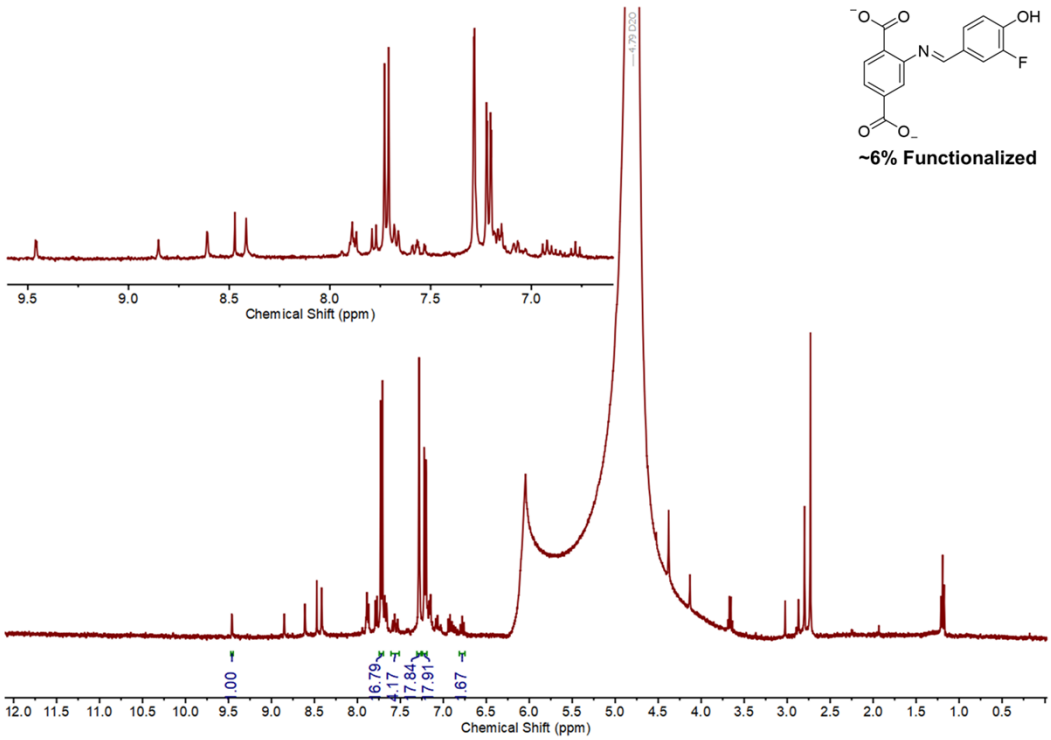

Figure S26. NMR of **I4** digested with saturated $NaHCO_3$ in D_2O showing integration values used to quantify the degree of functionalization.

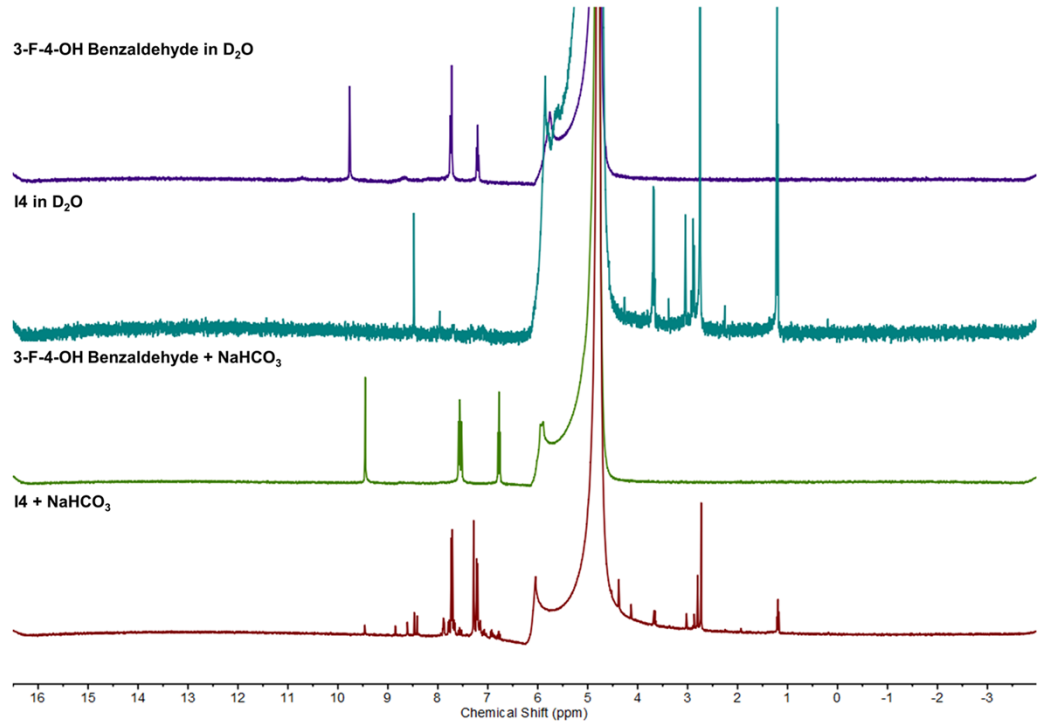

Figure S27. NMR spectra demonstrating the purity of **I4**.

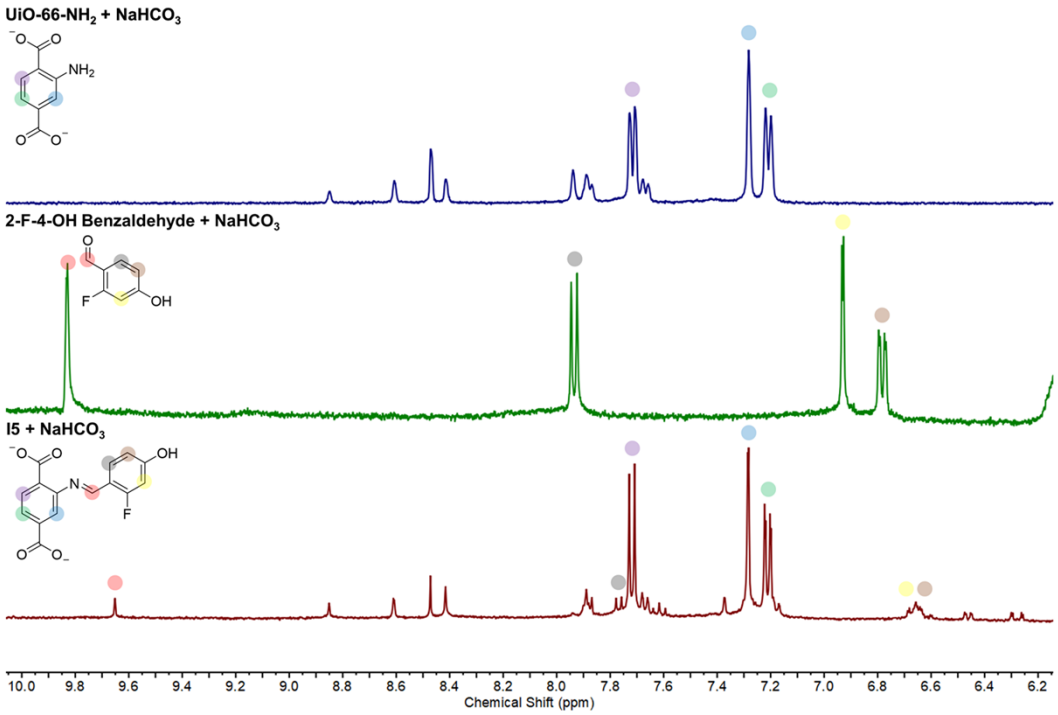

Figure S28. ^{1}H NMR of **I5** digested with saturated $NaHCO_3$ in D_2O (bottom), the corresponding coupling partner in the presence of saturated $NaHCO_3$ in D_2O (middle), and UiO-66-NH_2 digested with saturated $NaHCO_3$ in D_2O (top).

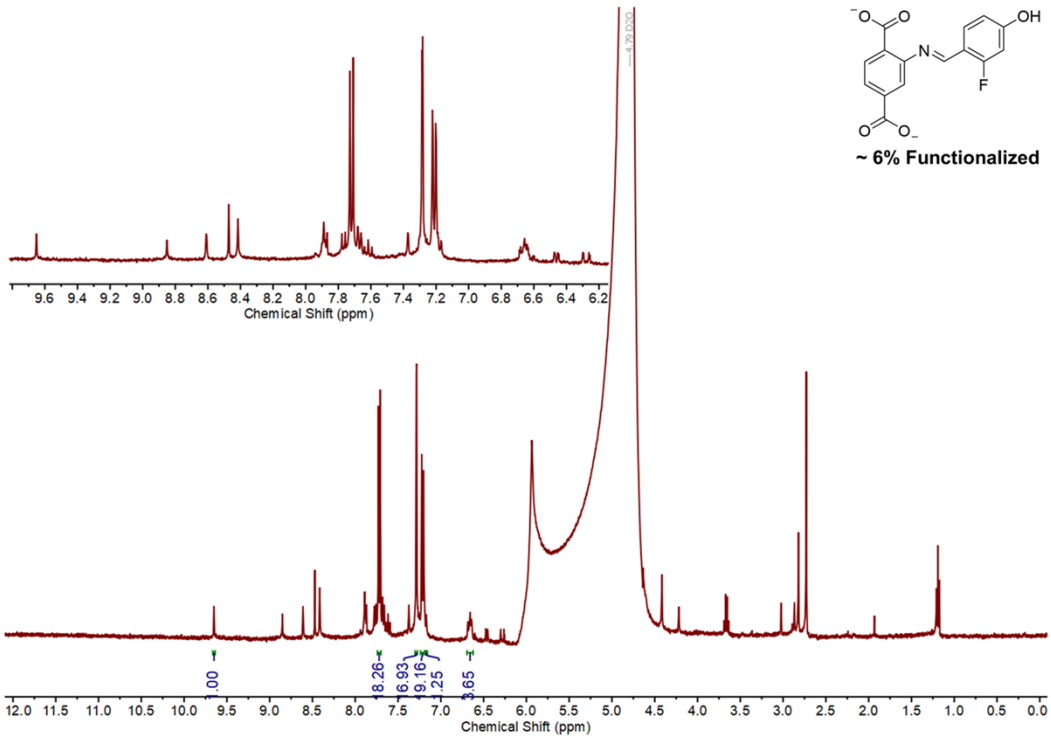

Figure S29. NMR of **I5** digested with saturated $NaHCO_3$ in D_2O showing integration values used to quantify the degree of functionalization.

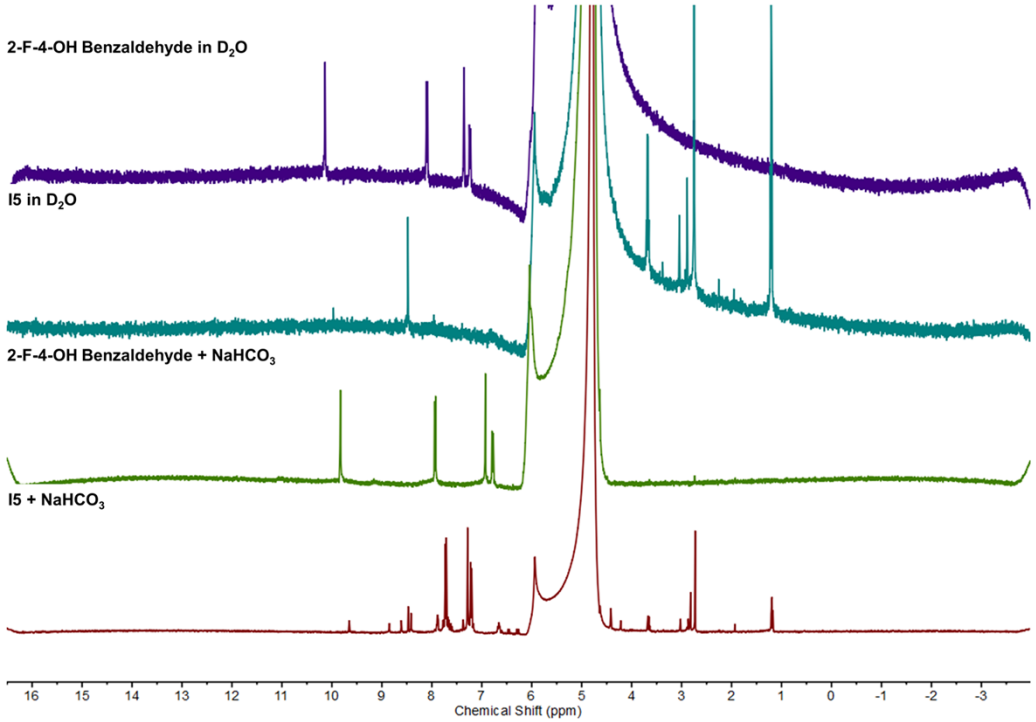

Figure S30. NMR spectra demonstrating the purity of **I5**.

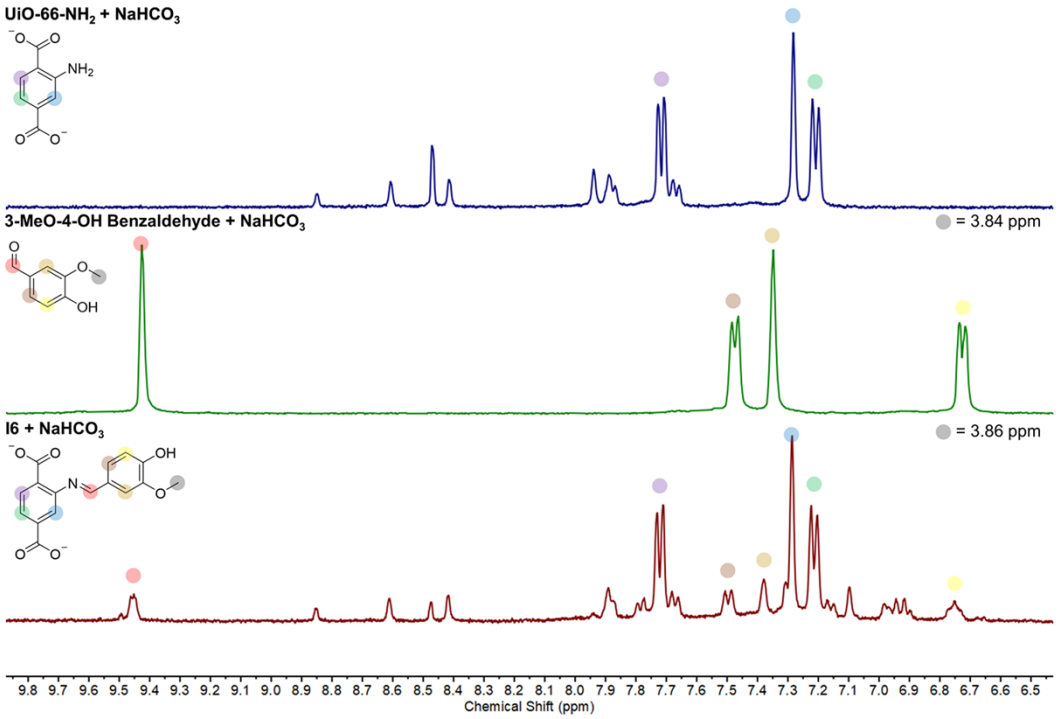

Figure S31. ^{1}H NMR of **I6** digested with saturated $NaHCO_3$ in D_2O (bottom), the corresponding coupling partner in the presence of saturated $NaHCO_3$ in D_2O (middle), and UiO-66-NH_2 digested with saturated $NaHCO_3$ in D_2O (top).

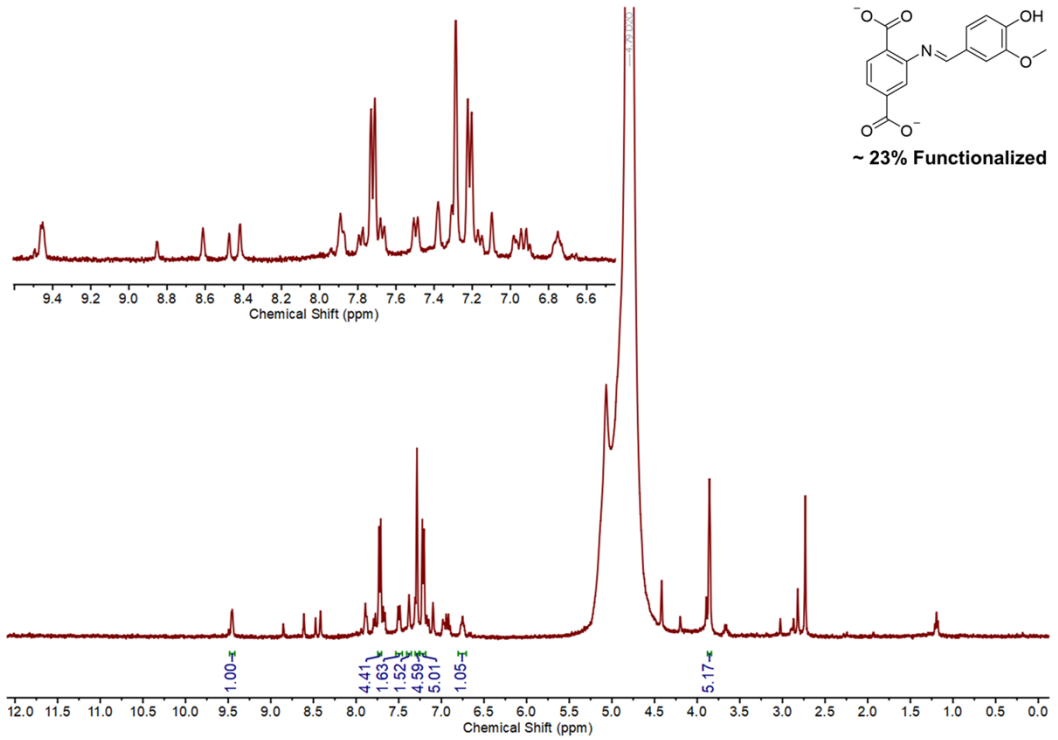

Figure S32. NMR of **I6** digested with saturated $NaHCO_3$ in D_2O showing integration values used to quantify the degree of functionalization.

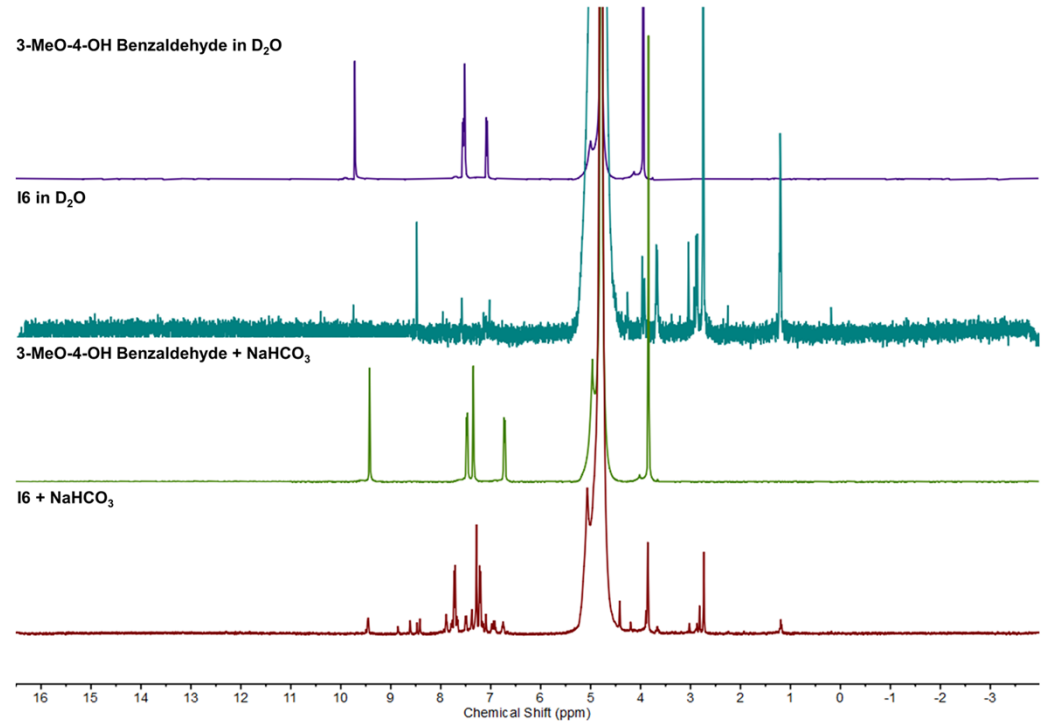

Figure S33. NMR spectra demonstrating the purity of **I6**.

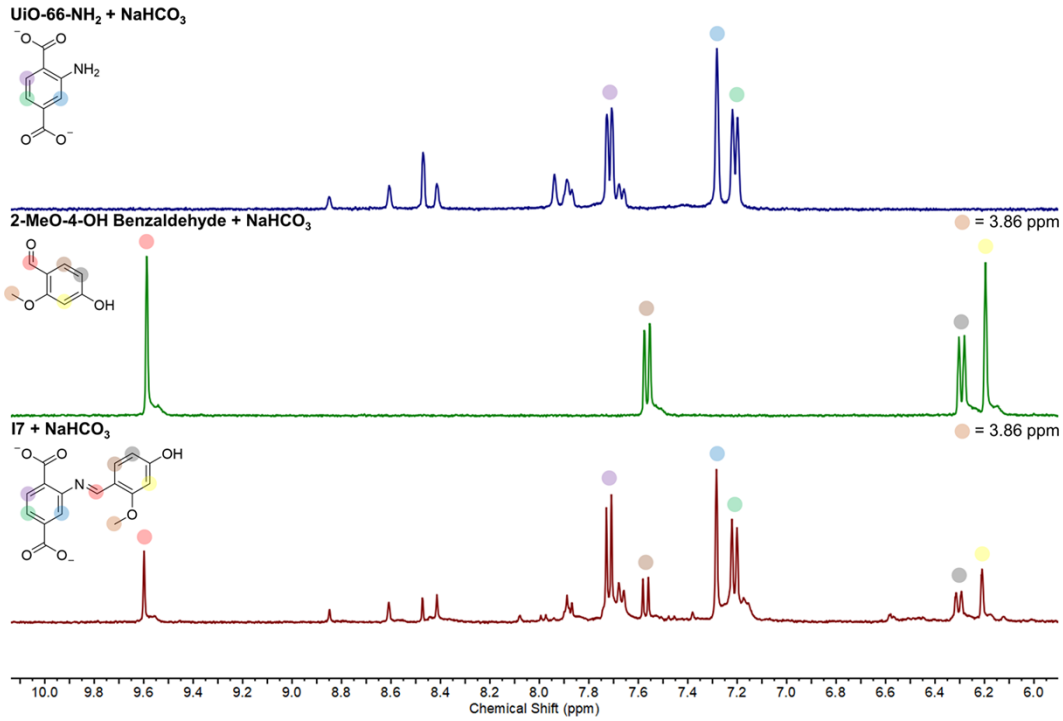

Figure S34. ^1H NMR of **I7** digested with saturated $NaHCO_3$ in D_2O (bottom), the corresponding coupling partner in the presence of saturated $NaHCO_3$ in D_2O (middle), and UiO-66-NH_2 digested with saturated $NaHCO_3$ in D_2O (top).

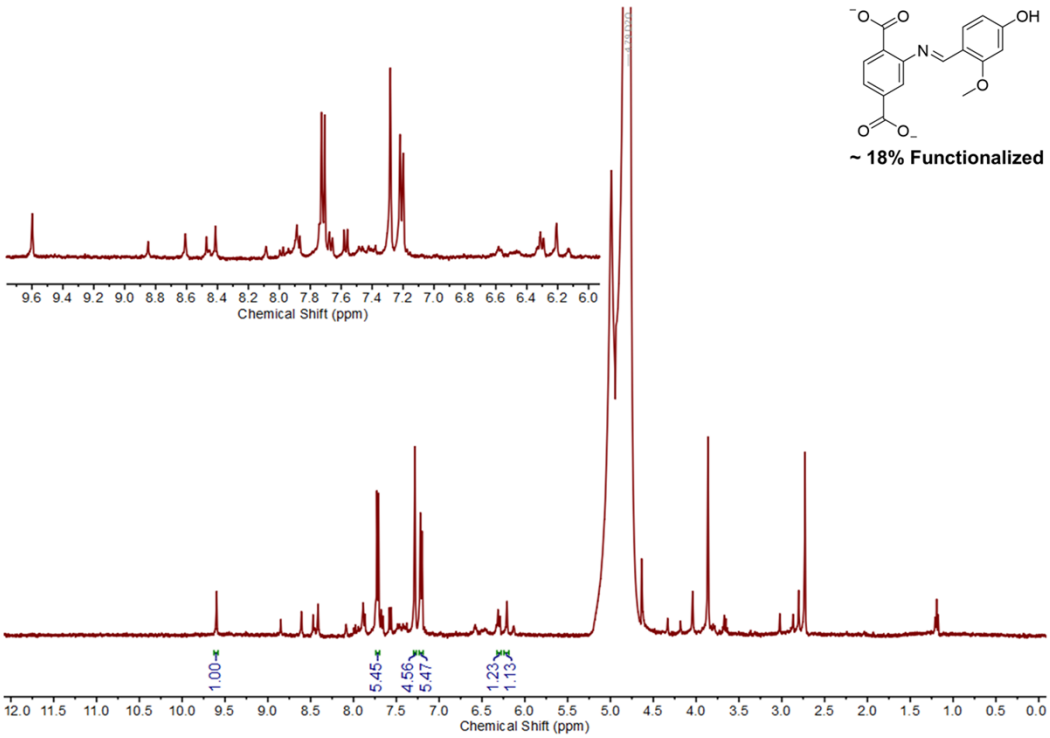

Figure S35. NMR of **I7** digested with saturated $NaHCO_3$ in D_2O showing integration values used to quantify the degree of functionalization.

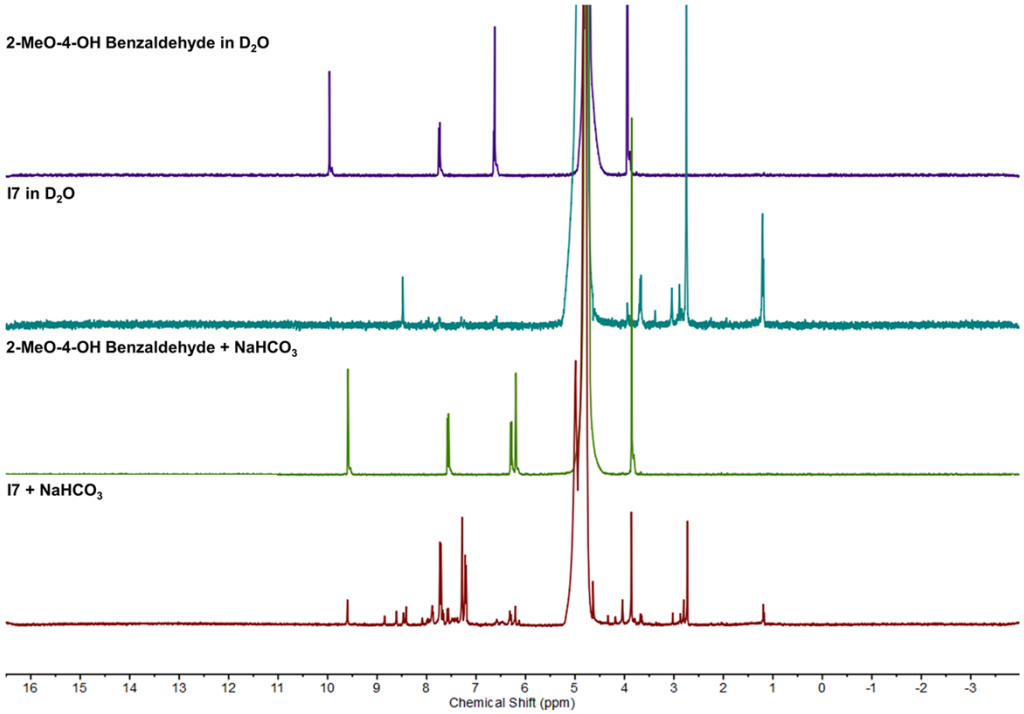

Figure S36. NMR spectra demonstrating the purity of **I7**.

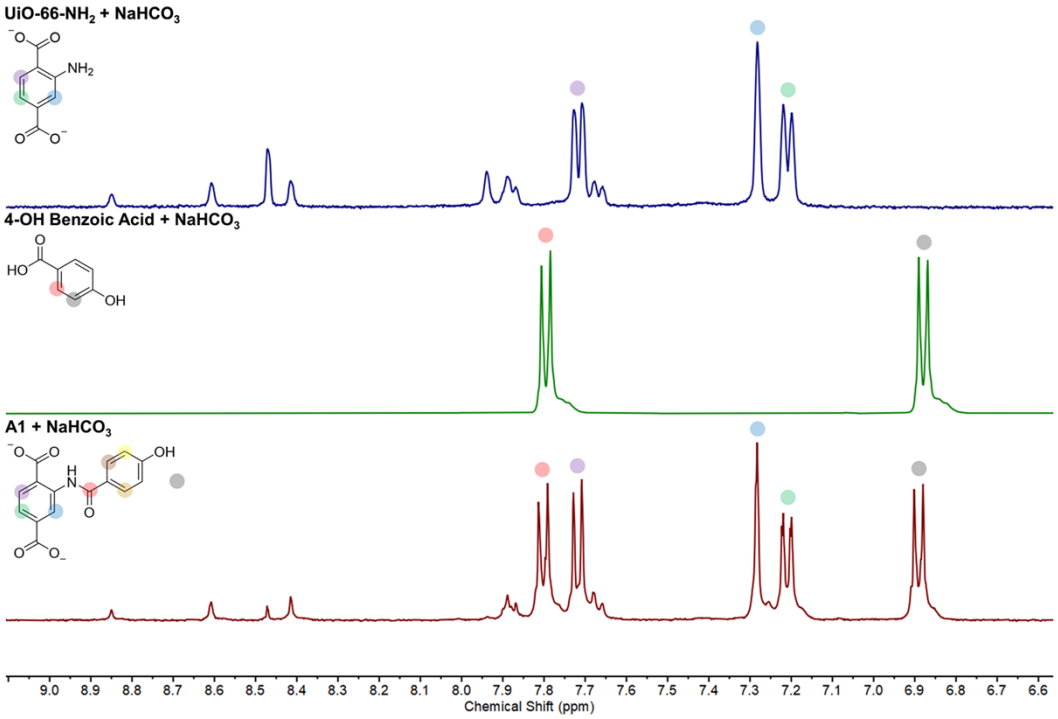

Figure S37. ^{1}H NMR of **A1** digested with saturated $NaHCO_3$ in D_2O (bottom), the corresponding coupling partner in the presence of saturated $NaHCO_3$ in D_2O (middle), and UiO-66-NH_2 digested with saturated $NaHCO_3$ in D_2O (top).

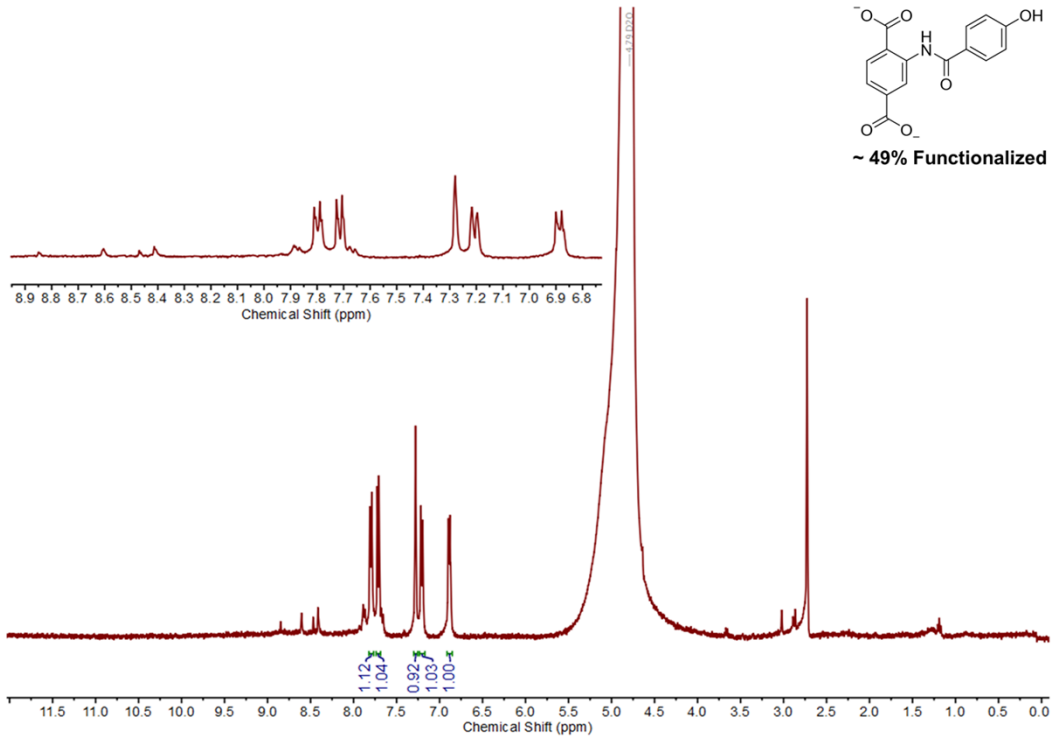

Figure S38. NMR of **A1** digested with saturated $NaHCO_3$ in D_2O showing integration values used to quantify the degree of functionalization.

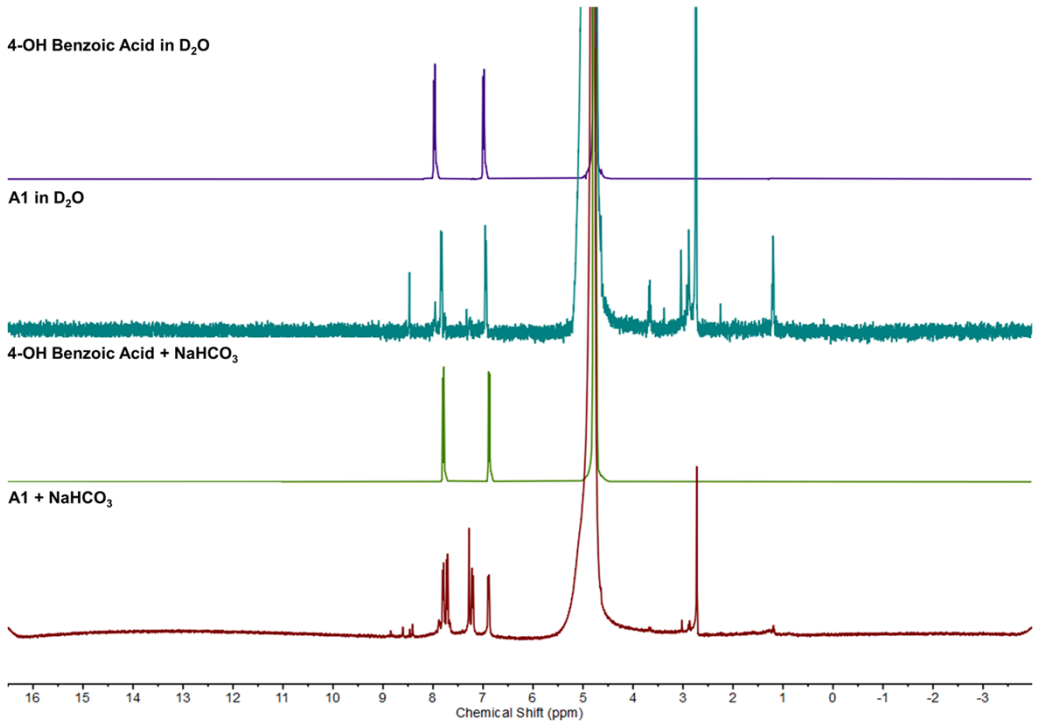

Figure S39. NMR spectra demonstrating the purity of **A1**.

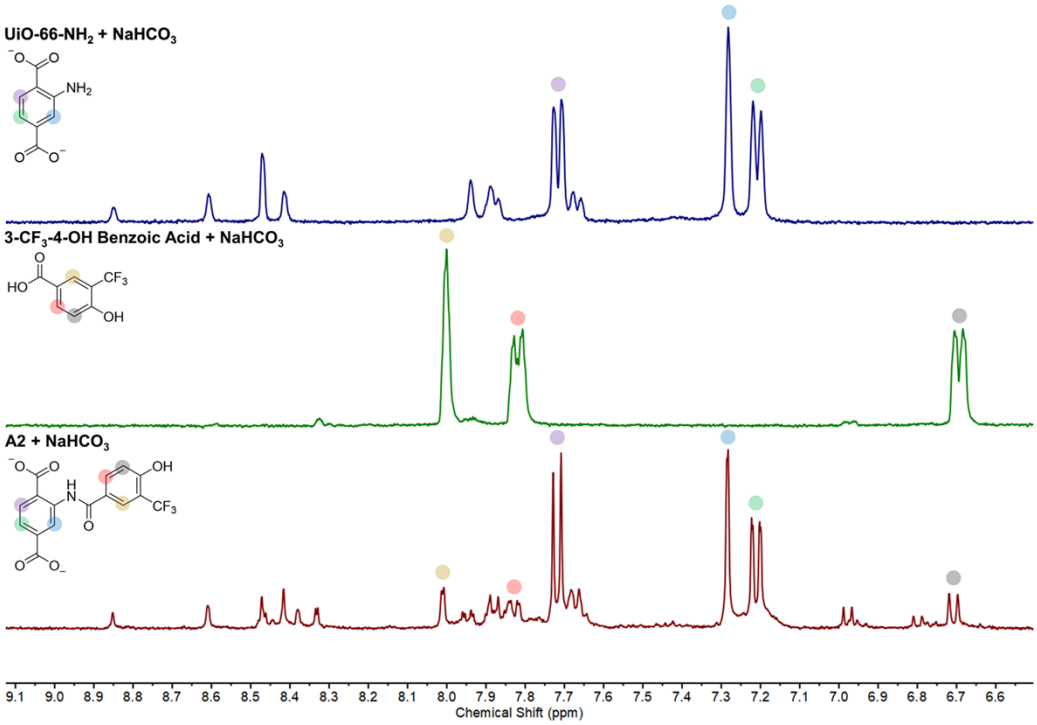

Figure S40. ^{1}H NMR of **A2** digested with saturated $NaHCO_3$ in D_2O (bottom), the corresponding coupling partner in the presence of saturated $NaHCO_3$ in D_2O (middle), and UiO-66-NH_2 digested with saturated $NaHCO_3$ in D_2O (top).

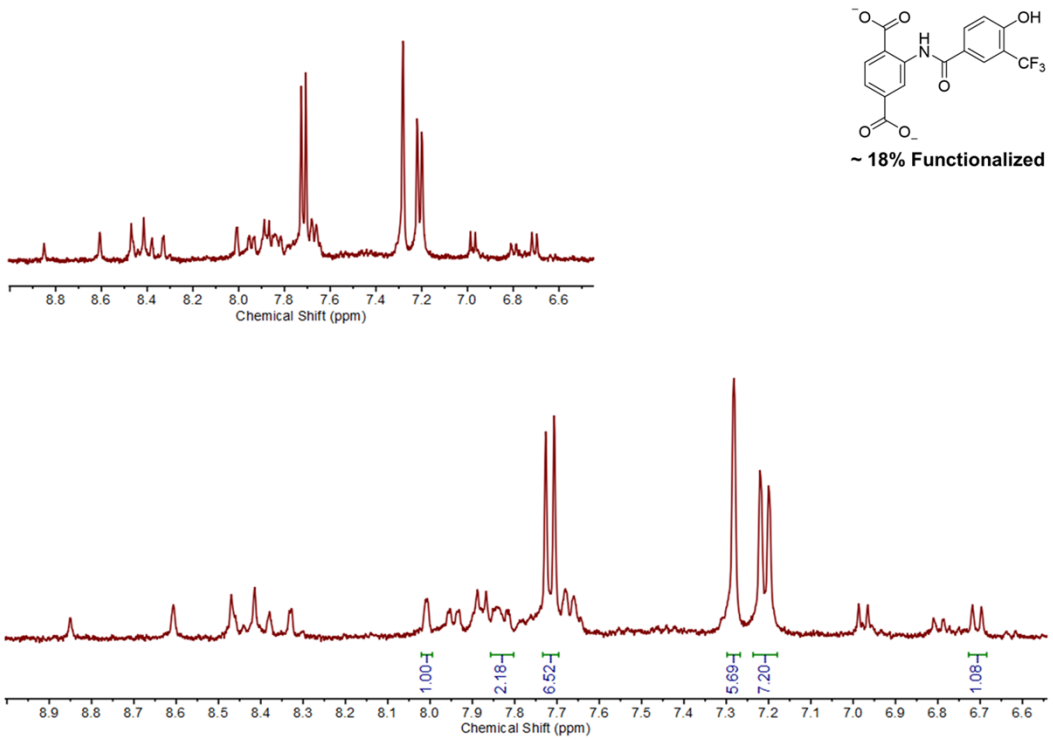

Figure S41. NMR of **A2** digested with saturated $NaHCO_3$ in D_2O showing integration values used to quantify the degree of functionalization.

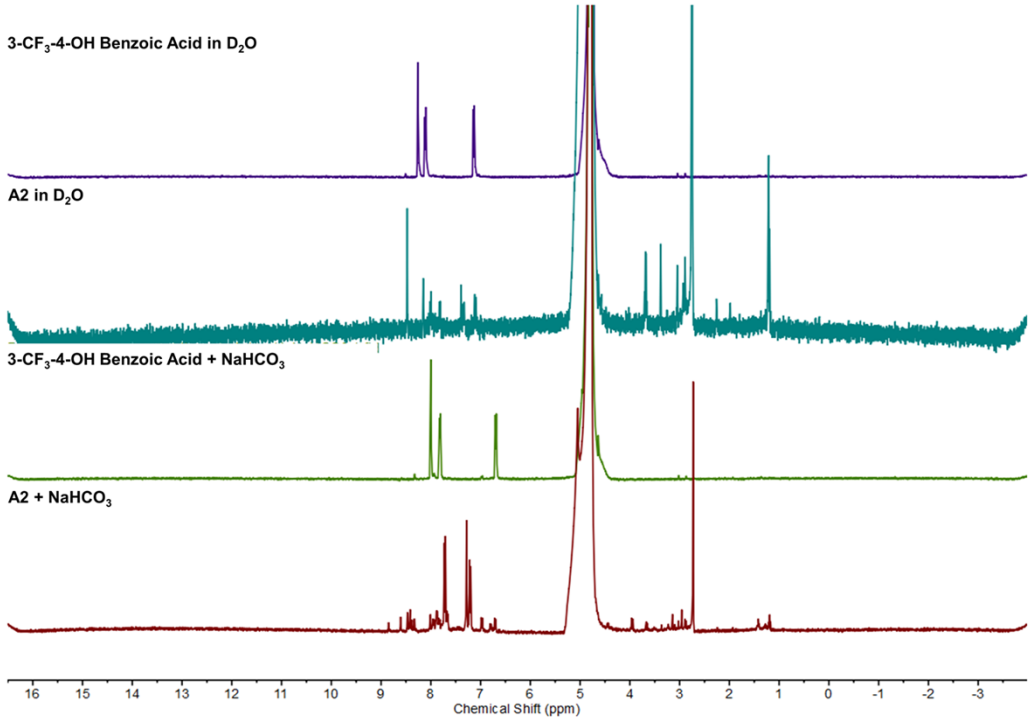

Figure S42. NMR spectra demonstrating the purity of **A2**.

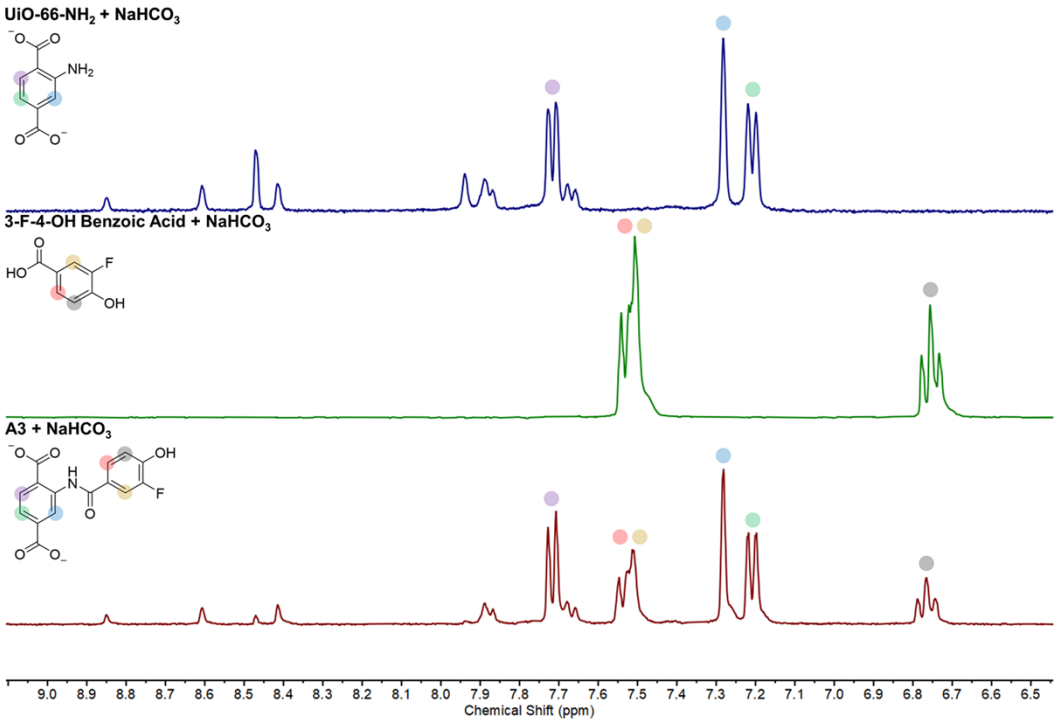

Figure S43. ^{1}H NMR of **A3** digested with saturated $NaHCO_3$ in D_2O (bottom), the corresponding coupling partner in the presence of saturated $NaHCO_3$ in D_2O (middle), and UiO-66-NH_2 digested with saturated $NaHCO_3$ in D_2O (top).

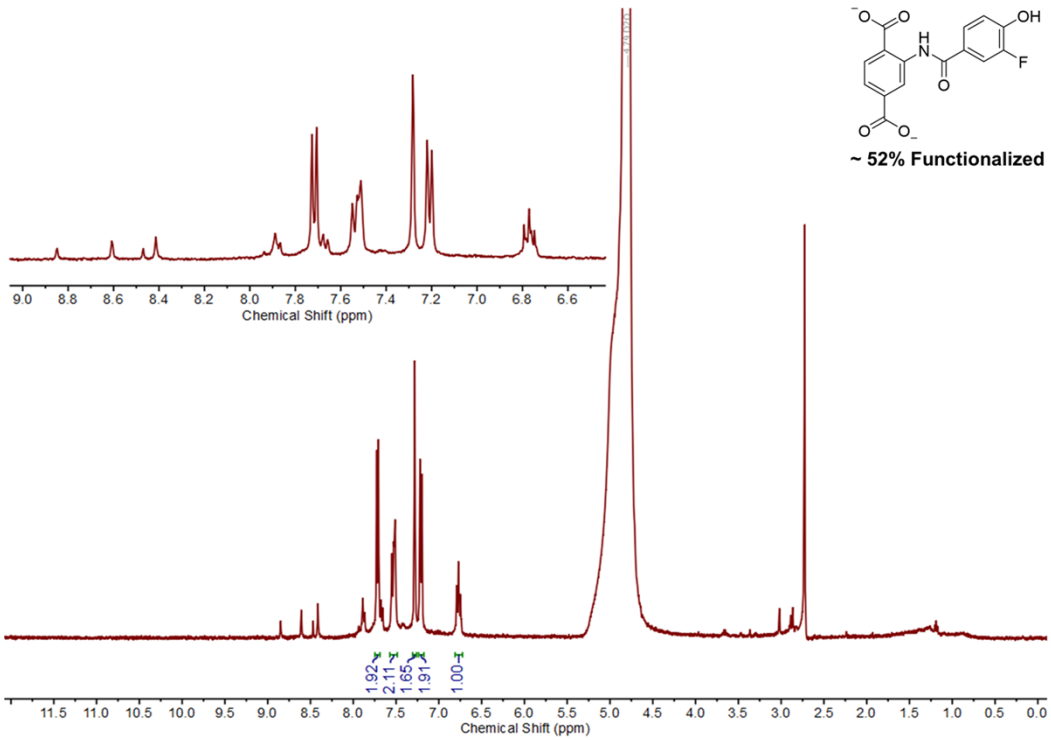

Figure S44. NMR of **A3** digested with saturated $NaHCO_3$ in D_2O showing integration values used to quantify the degree of functionalization.

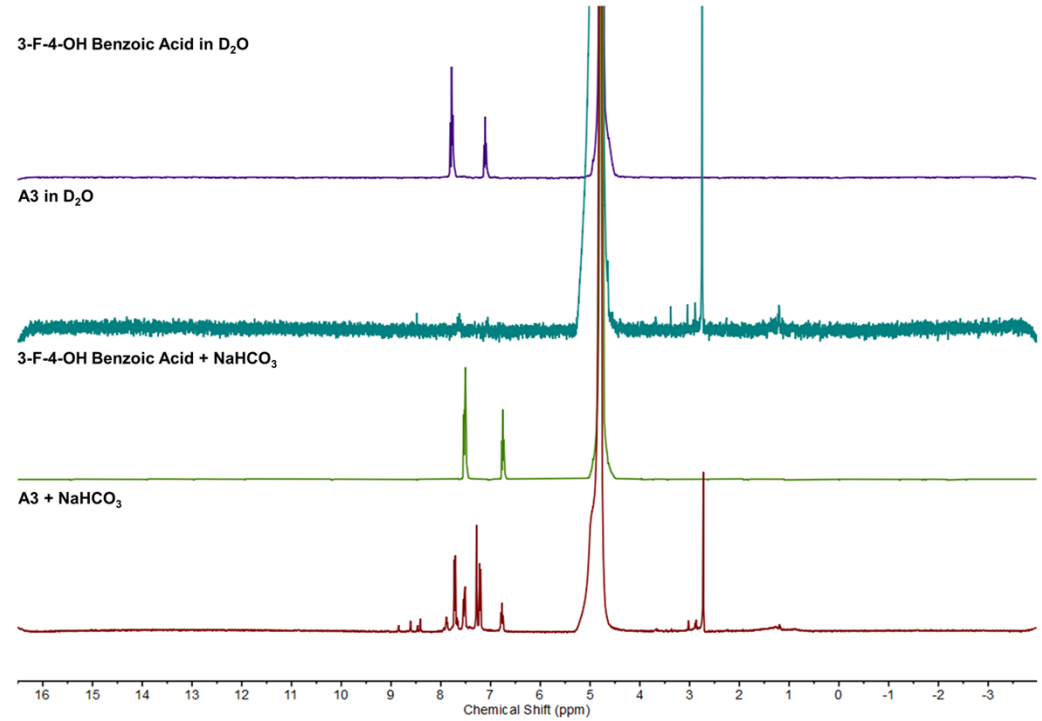

Figure S45. NMR spectra demonstrating the purity of **A3**.

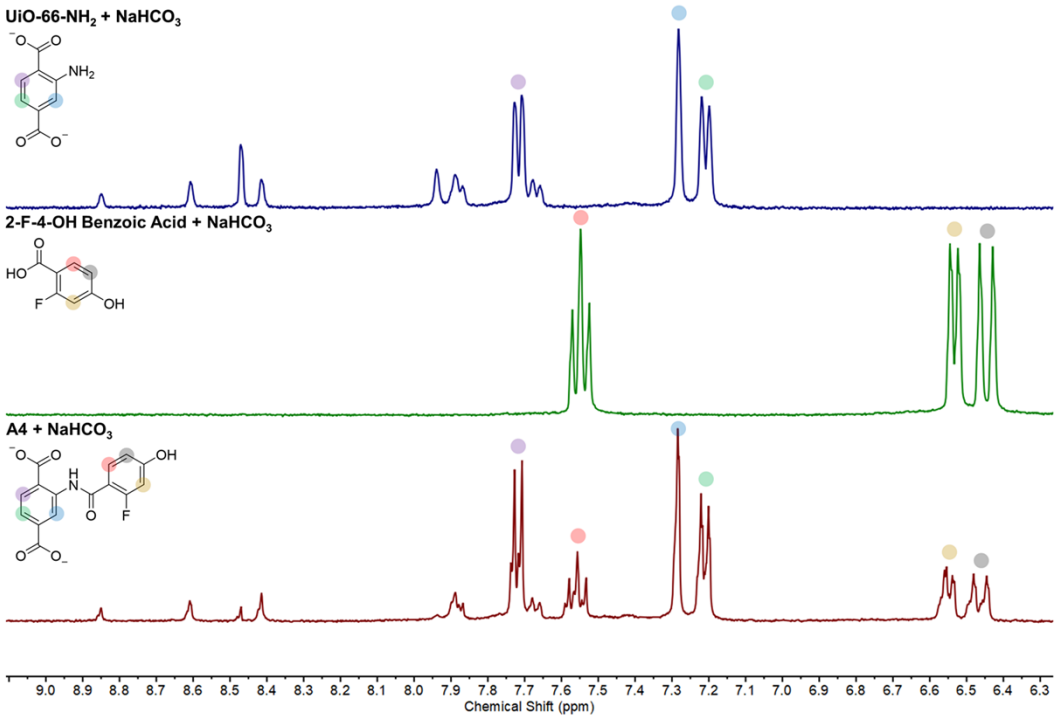

Figure S46. ^{1}H NMR of **A4** digested with saturated $NaHCO_3$ in D_2O (bottom), the corresponding coupling partner in the presence of saturated $NaHCO_3$ in D_2O (middle), and UiO-66-NH_2 digested with saturated $NaHCO_3$ in D_2O (top).

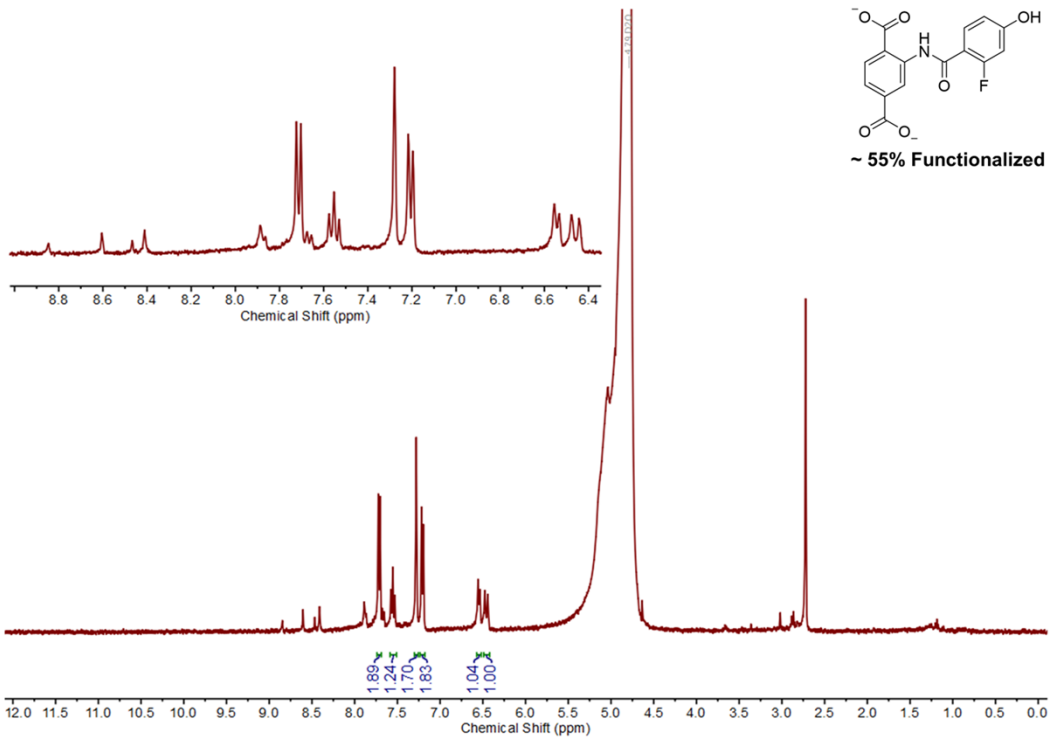

Figure S47. NMR of **A4** digested with saturated $NaHCO_3$ in D_2O showing integration values used to quantify the degree of functionalization.

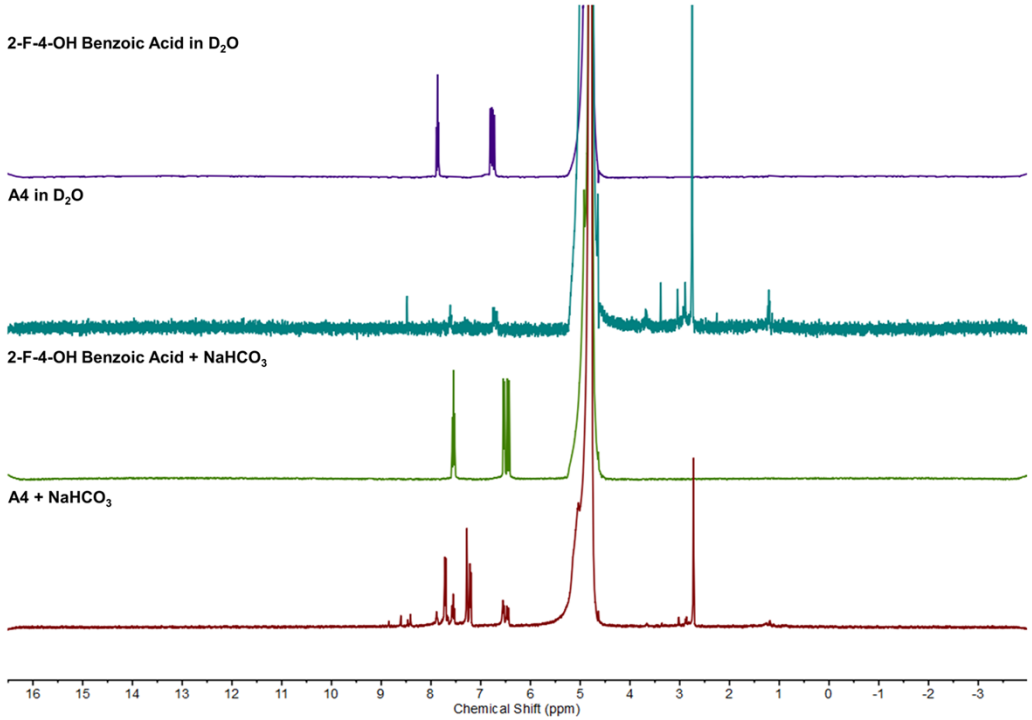

Figure S48. NMR spectra demonstrating the purity of **A4**.

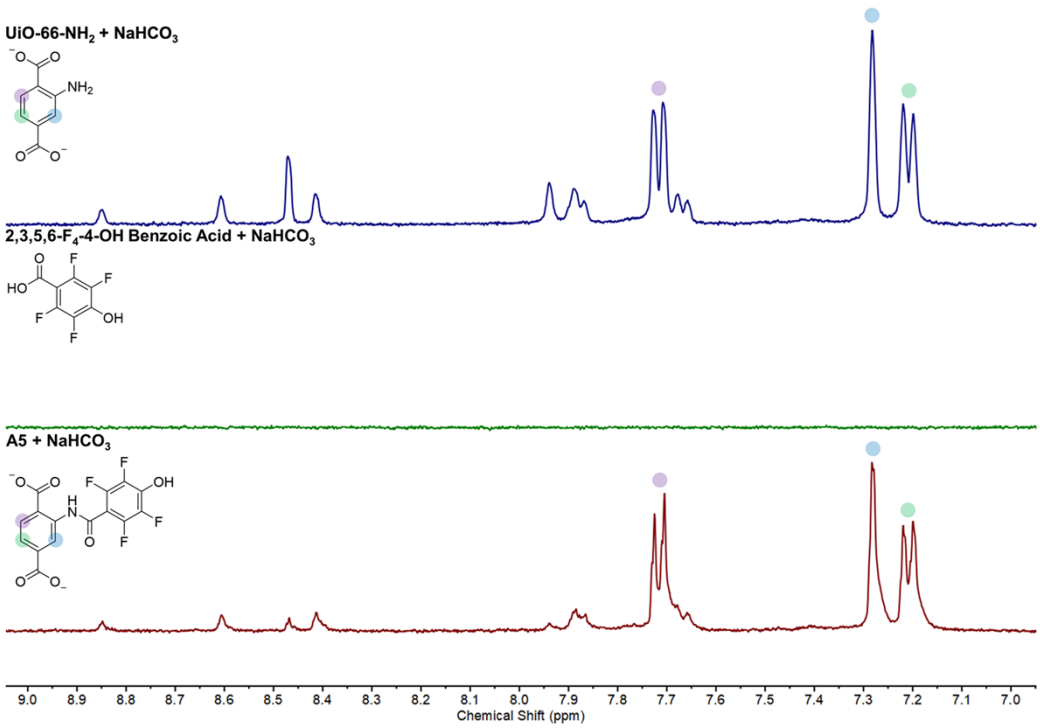

Figure S49. ^{1}H NMR of **A5** digested with saturated $NaHCO_3$ in D_2O (bottom), the corresponding coupling partner in the presence of saturated $NaHCO_3$ in D_2O (middle), and UiO-66-NH_2 digested with saturated $NaHCO_3$ in D_2O (top).

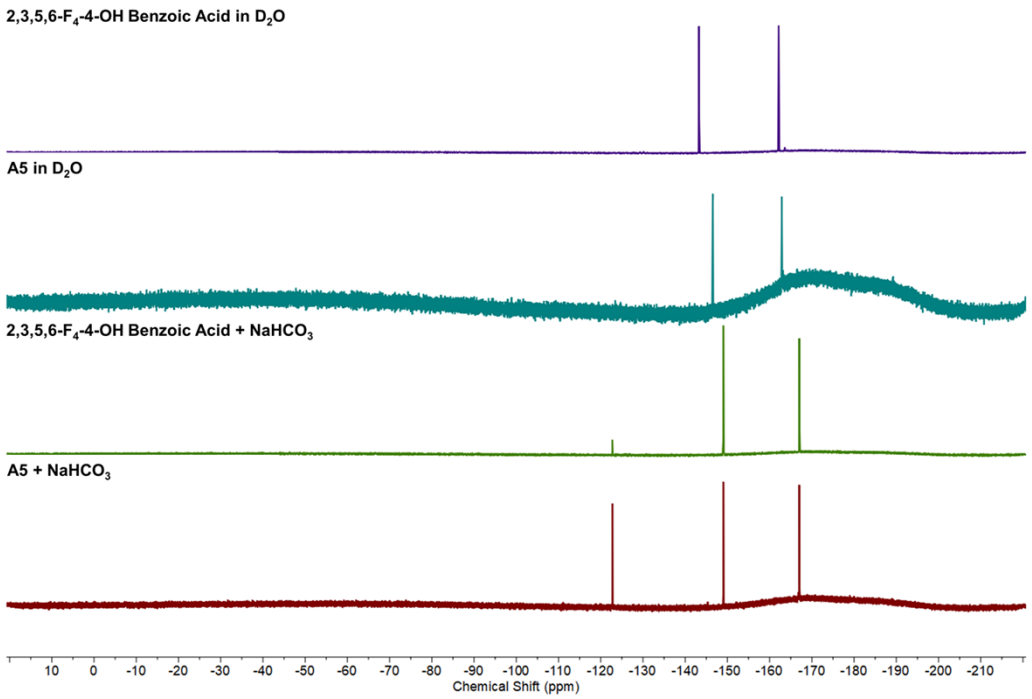

Figure S50. NMR spectra demonstrating the purity of **A5**.

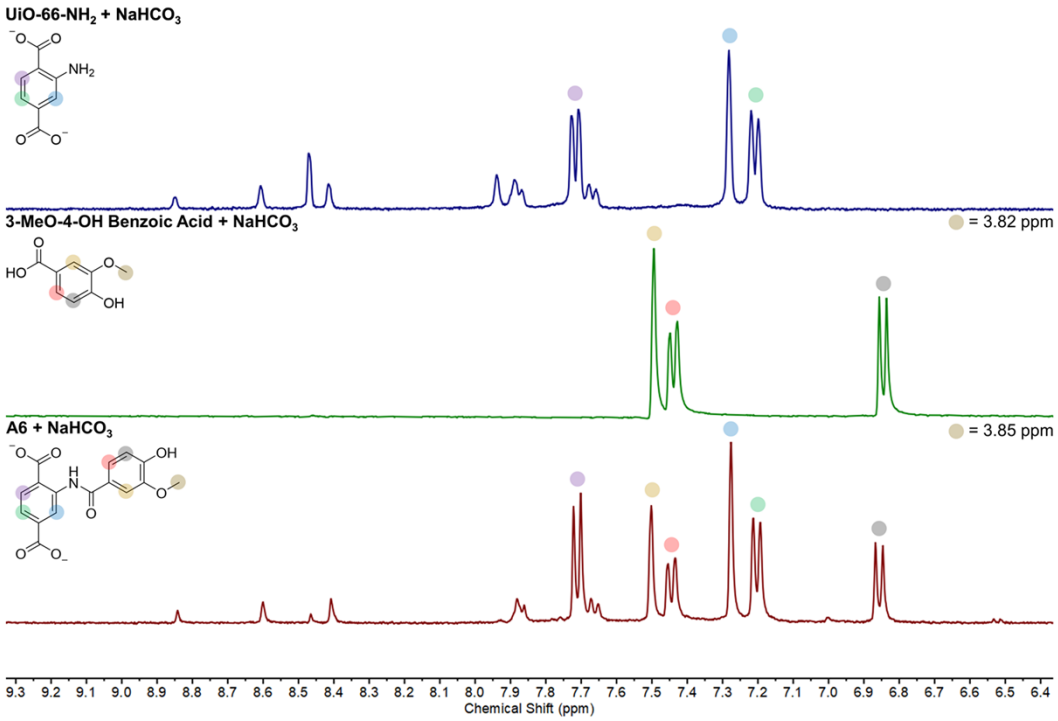

Figure S51. ^{1}H NMR of **A6** digested with saturated $NaHCO_3$ in D_2O (bottom), the corresponding coupling partner in the presence of saturated $NaHCO_3$ in D_2O (middle), and UiO-66-NH_2 digested with saturated $NaHCO_3$ in D_2O (top).

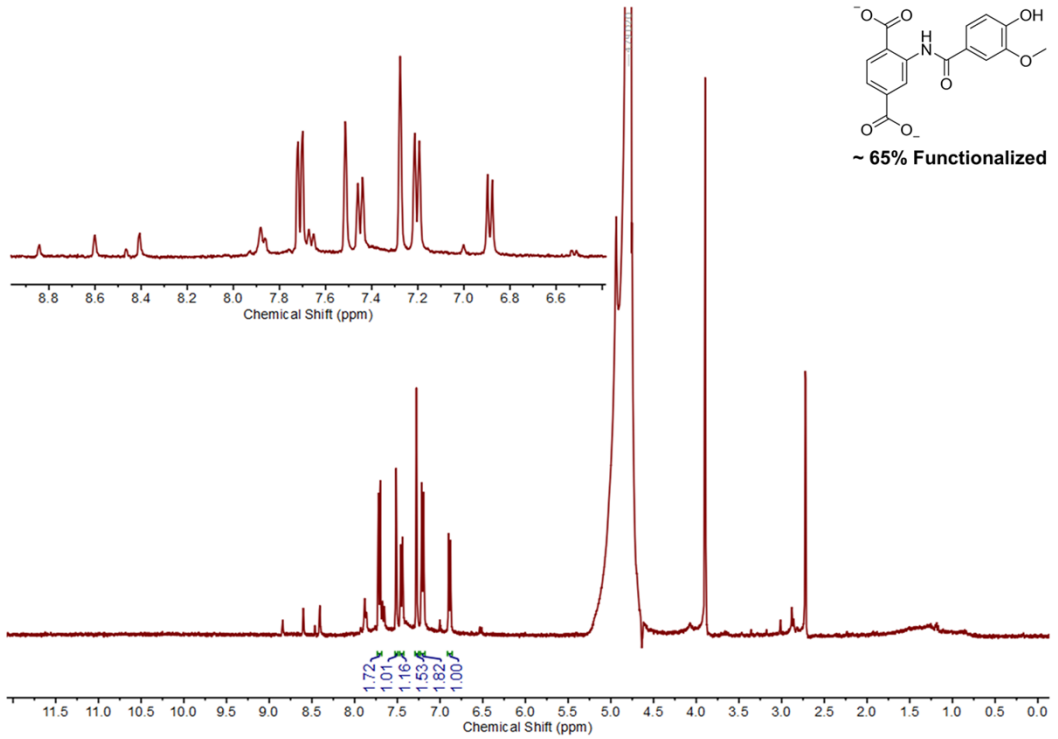

Figure S52. NMR of **A6** digested with saturated $NaHCO_3$ in D_2O showing integration values used to quantify the degree of functionalization.

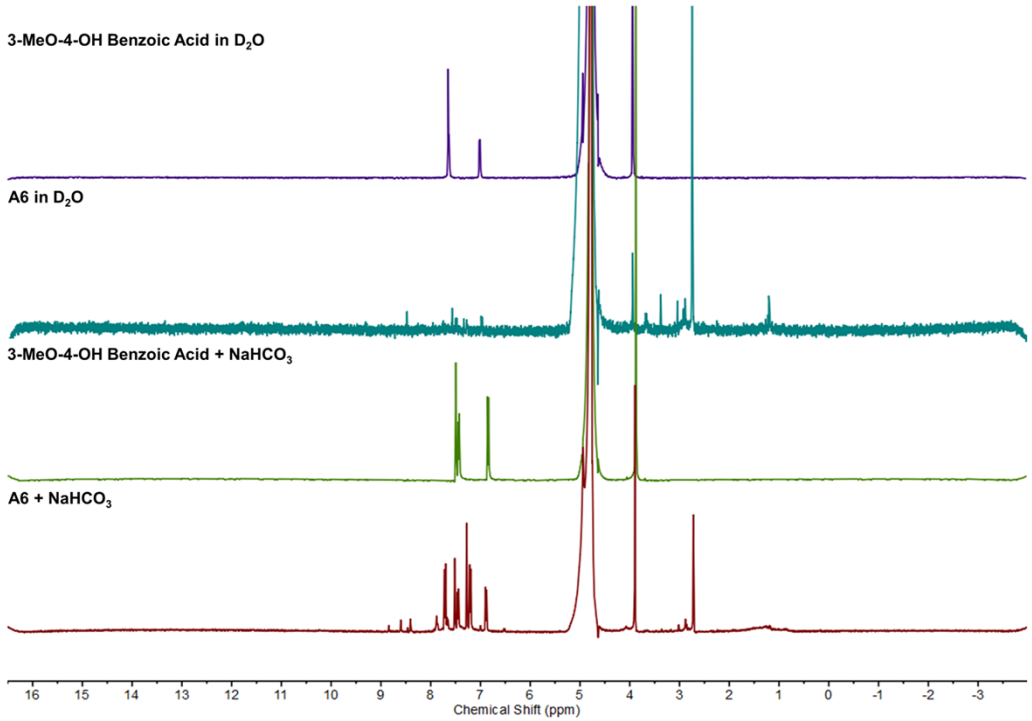

Figure S53. NMR spectra demonstrating the purity of **A6**.

*UV-Vis of **A1** – **A6** Suspensions*

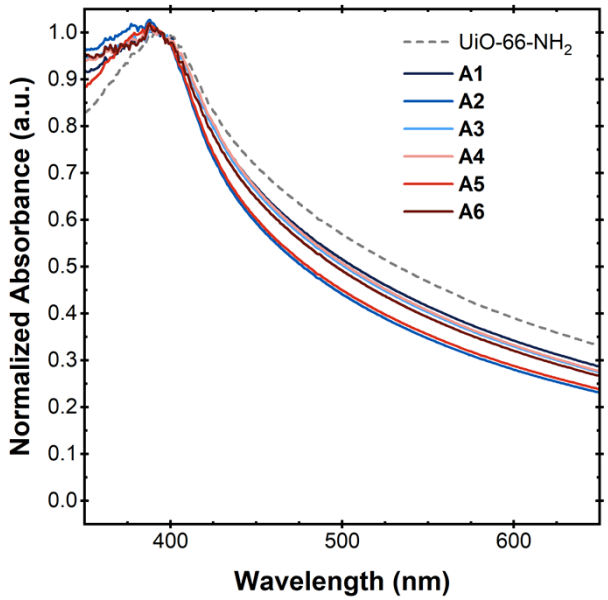

Figure S54. Normalized UV-visible absorption spectra of UiO-66-NH_2 (for reference) and **A1** – **A6** suspended in DMF at an approximate concentration of 0.15 mg mL^{-1}. Since the amide bridging group does not increase the conjugation of the system, no significant differences relative to UiO-66-NH_2 are expected.

Synthesis and Characterization of an Imine Small Molecule Analogue

Dimethyl aminoterephthalate (0.1032 g, 0.4933 mmol, 1 eq) and 4-hydroxy-3-methoxybenzaldehyde (vanillin, 0.1492 g, 0.9806 mmol, 2 eq) were weighed into a 20 mL glass scintillation vial with a magnetic stir bar. Methanol (5 mL) was added to the vial, and the reaction was allowed to stir at room temperature for 1 week. During that time, the solution changed from colorless to yellow-orange in color. After 1 week, the reaction was centrifuged and decanted to separate the orange solution from undissolved starting materials, and the solvent was evaporated to give a yellow-orange solid. The product was characterized by ^1H NMR spectroscopy in $CDCl_3$ and D_2O, as well as UV-visible spectroscopy in methanol.

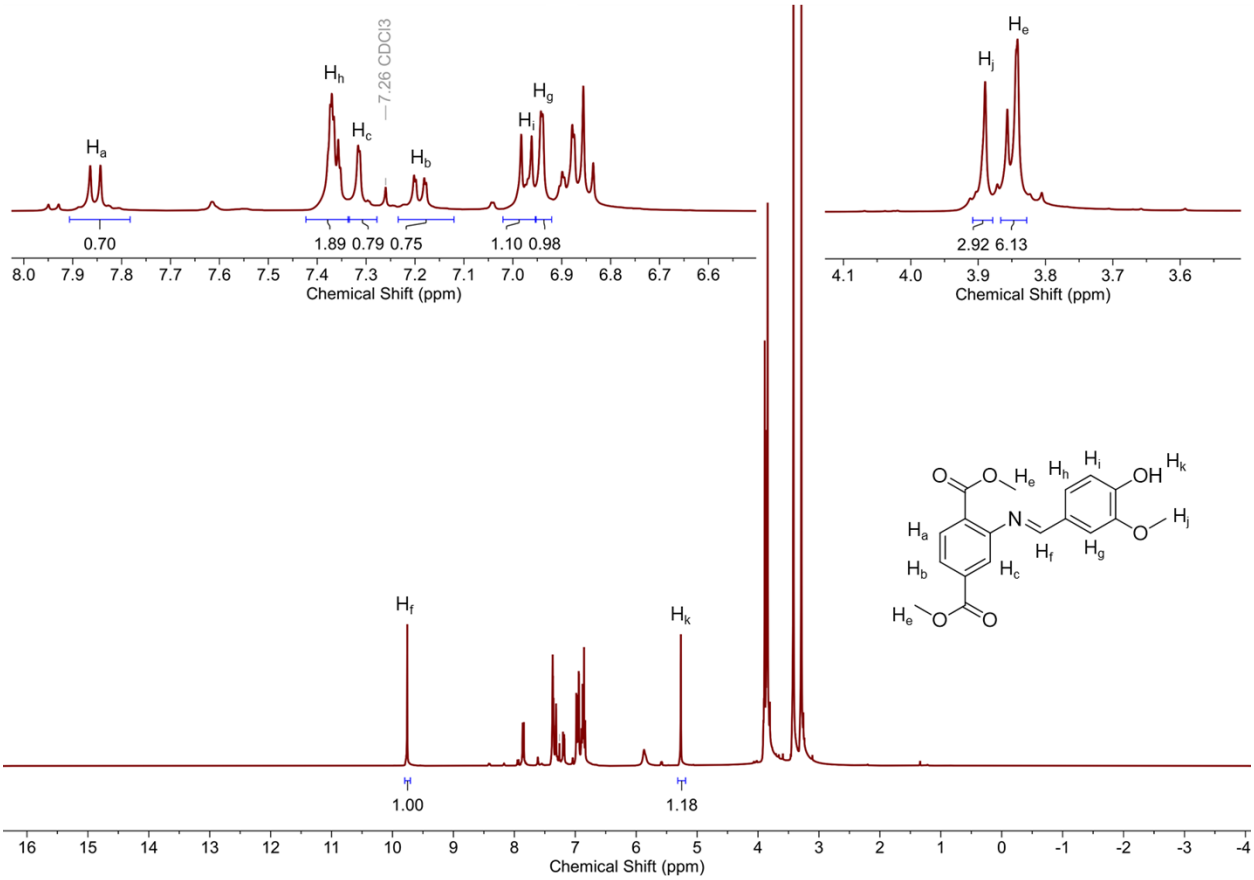

Figure S55. ^1H NMR of the crude small molecule analogue product in $CDCl_3$.

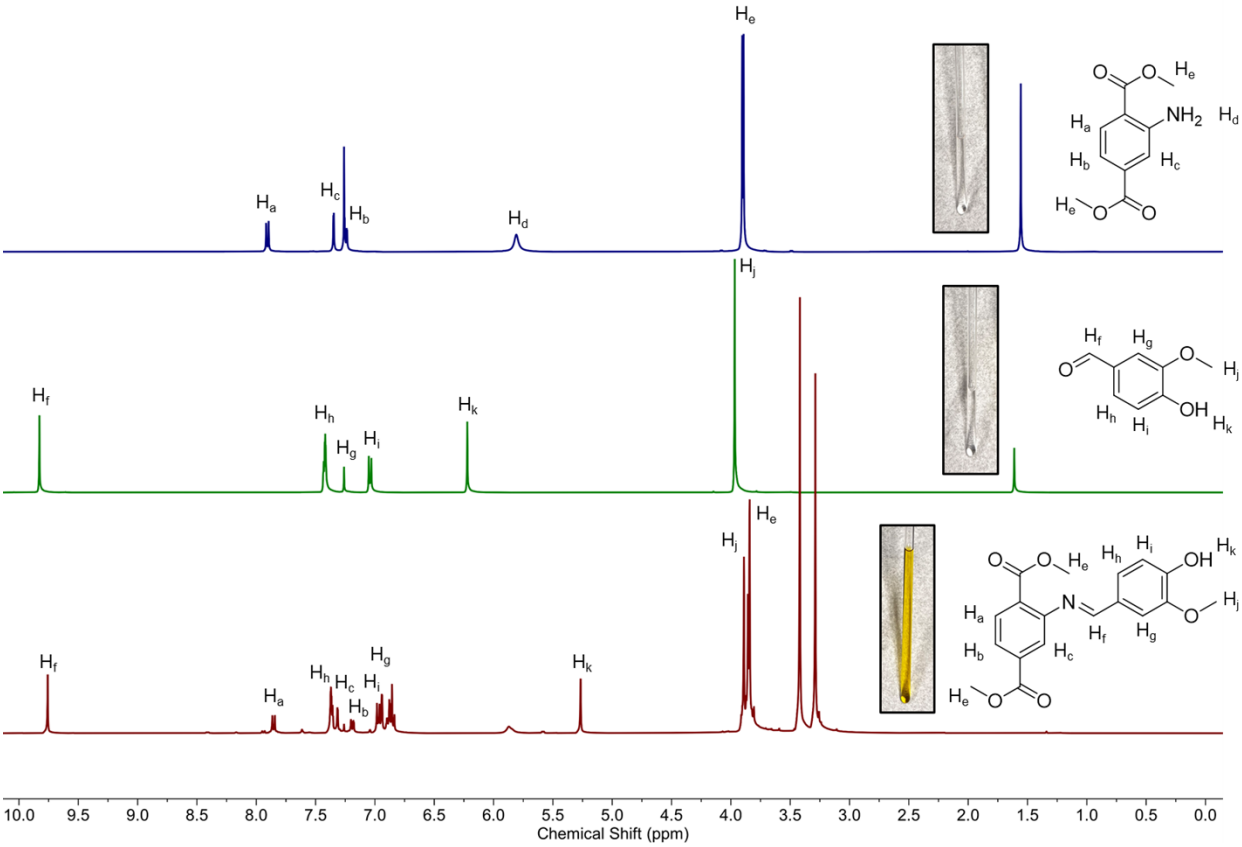

Figure S56. Overlayed ^{1}H NMR of the crude small molecule analogue product (bottom), along with pristine vanillin (middle) and dimethyl aminoterephthalate (top) in $CDCl_3$. Figure insets show photographs of the NMR solutions, highlighting the distinct color change observed during the reaction.

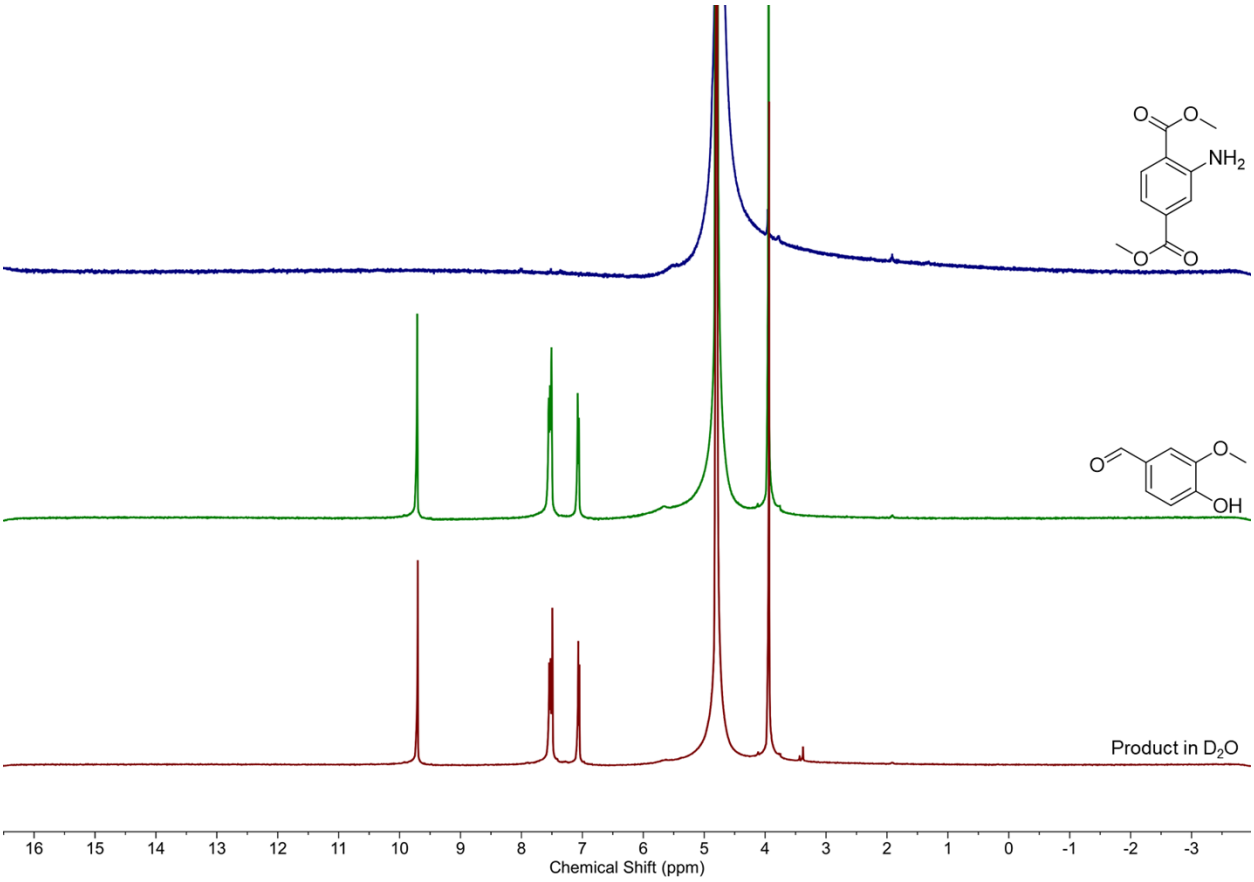

Figure S57. ^{1}H NMR of the crude small molecule analogue product (bottom), vanillin (middle), and dimethyl aminoterephthalate (top) in D_2O.

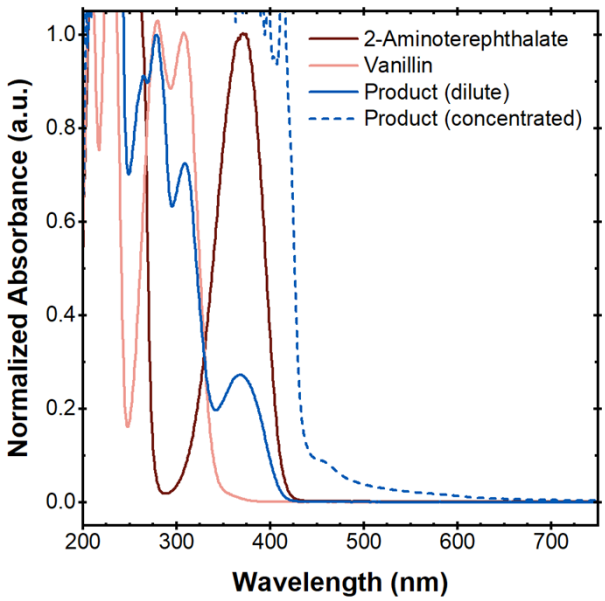

Figure S58. UV-visible absorption spectra of the crude small molecule analogue product, vanillin, and dimethyl aminoterephthalate in methanol. A second spectrum of the crude product is provided at higher concentration showing the appearance of a shoulder around 450 nm, which supports the formation of an imine-product and likely gives the product its orange color.

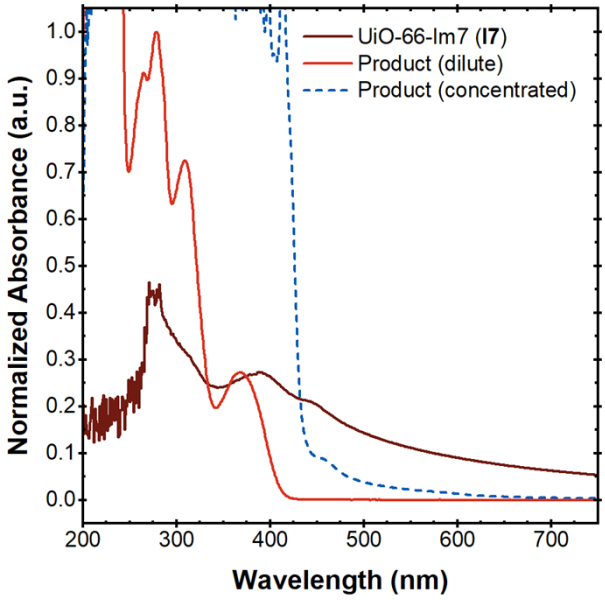

Figure S59. UV-visible absorption spectrum of the crude small molecule analogue product compared to one of the imine-functionalized MOFs (**I7**). Similar absorption features are observed between the two, including a weak signal around 450 nm that is assigned to the imine in both cases.

*Reduction of Imine **I6** with Sodium Borohydride*

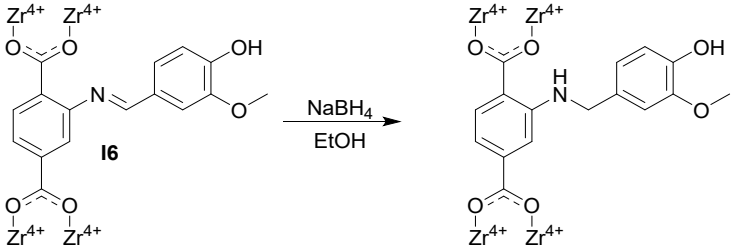

Figure S60. Scheme for the reduction of **I6** using sodium borohydride.

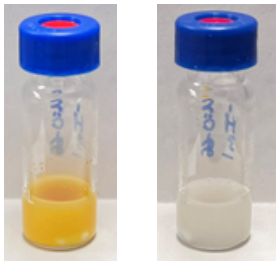

Figure S61. Photographs of **I6** before (left) and after (right) reduction with sodium borohydride.

To investigate this reaction in greater detail, a second sample of **I6** was reduced and digested for NMR analysis using the following procedure:

***I6** (0.0480 g, 0.1642 mmol NH_2 estimated, 1 eq) and sodium borohydride (0.0243 g, 0.6423 mmol, 3 eq) were weighed into a 20 mL glass scintillation vial with a magnetic stir bar. Ethanol (5 mL) was added, and the reaction was stirred at room temperature overnight. During this time, the color of the solid MOF material changed from yellow-orange to colorless. The reaction was then centrifuged, and the supernatant was decanted and replaced with fresh ethanol. This process was repeated to wash the solid twice, after which it was dried briefly on a rotary evaporator and analyzed by NMR spectroscopy.*

The ^{1}H NMR spectrum of the reduced and digested product could not be analyzed and integrated to determine the degree to which the **I6** starting material had been functionalized. However, the disappearance of the imine signal at 9.37 ppm (N-C**H**) and the appearance of a new signal at 3.80 ppm (N-C**H**$_2$) was observed, which could correspond to conversion of the imine to an amine.

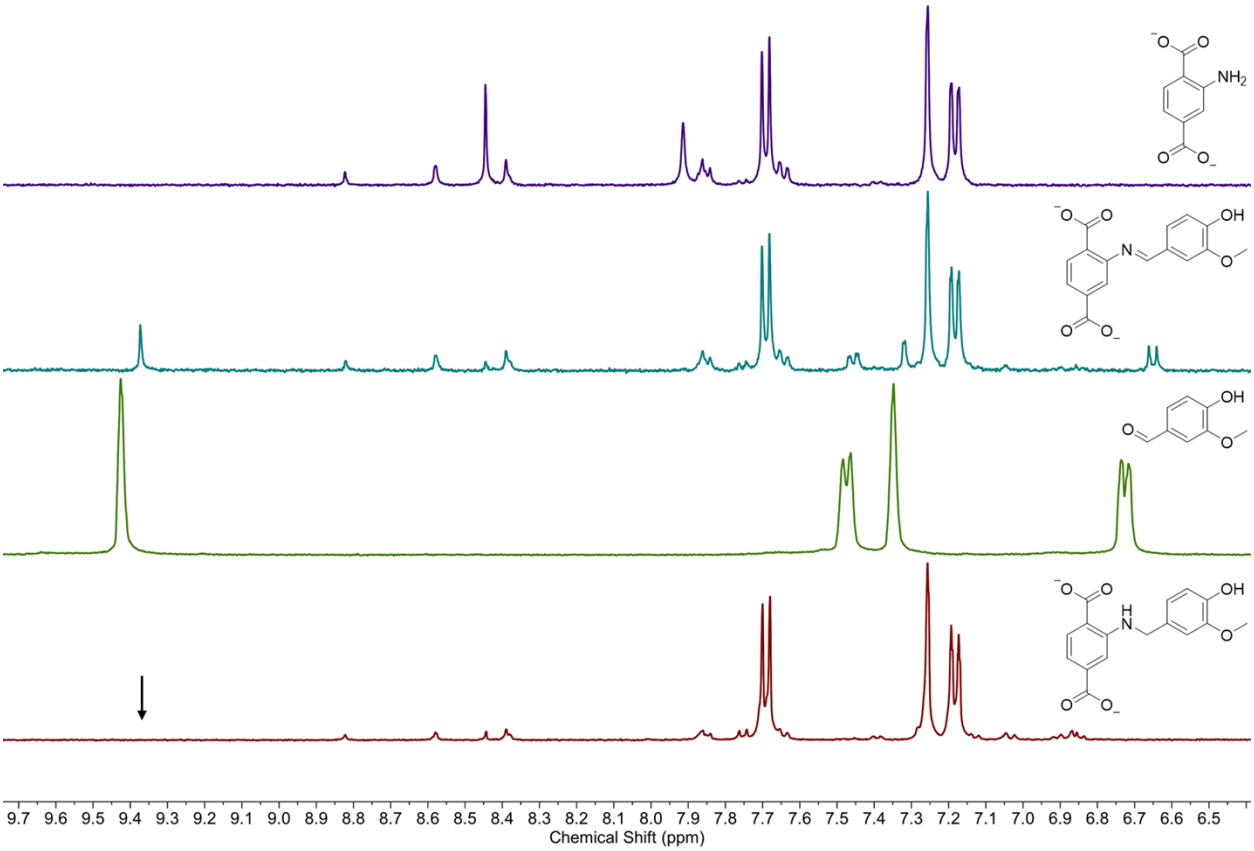

Figure S62. ^{1}H NMR of **I6** after reduction with sodium borohydride and digestion in saturated $NaHCO_3$ in D_2O (bottom), compared to the NMR spectra of digested UiO-66-NH_2, **I6**, and vanillin (top to bottom, respectively). The aromatic region shown here shows the disappearance of the peak assigned to the imine proton in **I6** upon reduction with sodium borohydride (highlighted with a black arrow).

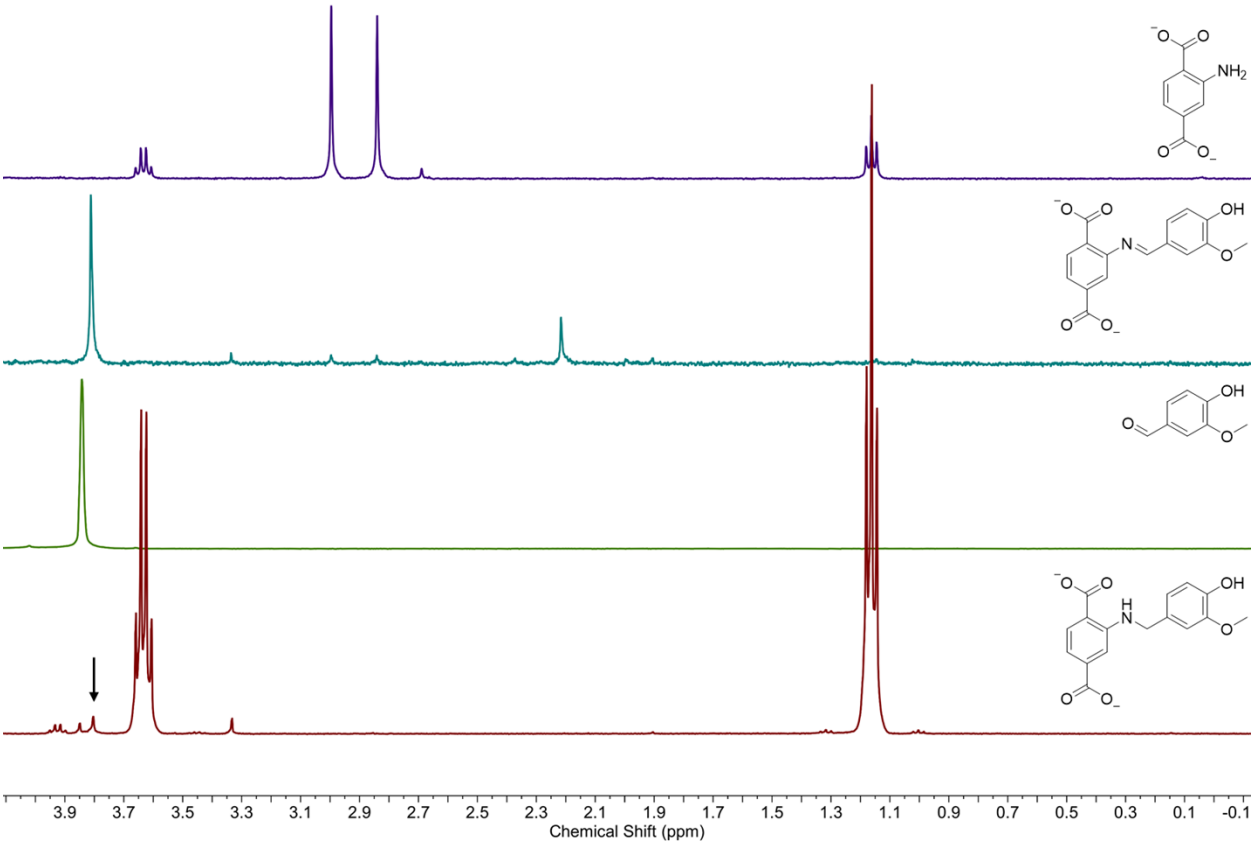

Figure S63. ^{1}H NMR of **I6** after reduction with sodium borohydride and digestion in saturated $NaHCO_3$ in D_2O (bottom), compared to the NMR spectra of digested UiO-66-NH_2, **I6**, and vanillin (top to bottom, respectively). The aliphatic region shown here shows the appearance of a new peak (highlighted with a black arrow) that could correspond to the CH_2 adjacent to the amine formed after reduction of **I6** using sodium borohydride.

Powder X-Ray Diffraction

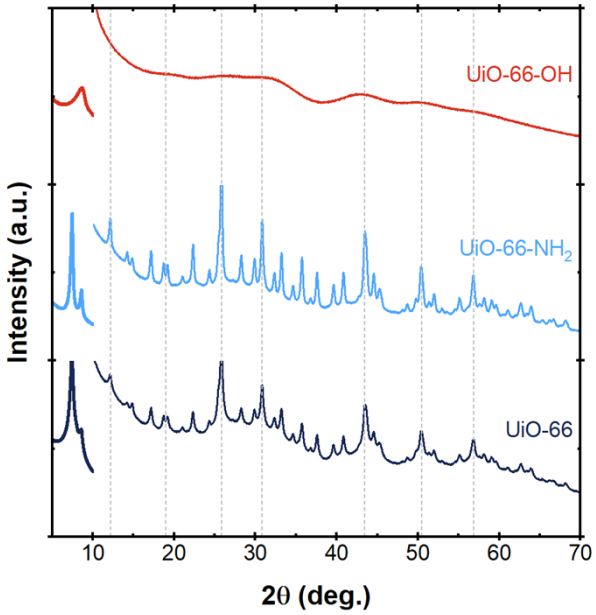

Figure S64. Powder patterns of UiO-66, UiO-66-NH_2, and UiO-66-OH.

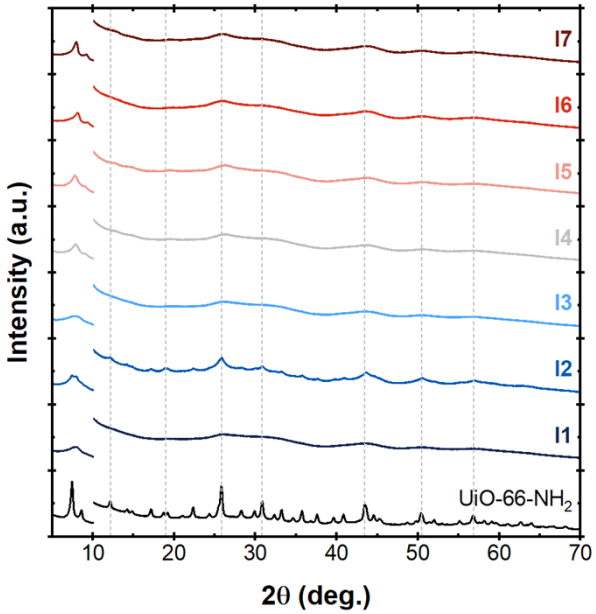

Figure S65. Powder patters of imine-functionalized MOFs **I1** – **I7** compared to the powder pattern of UiO-66-NH_2 (bottom).

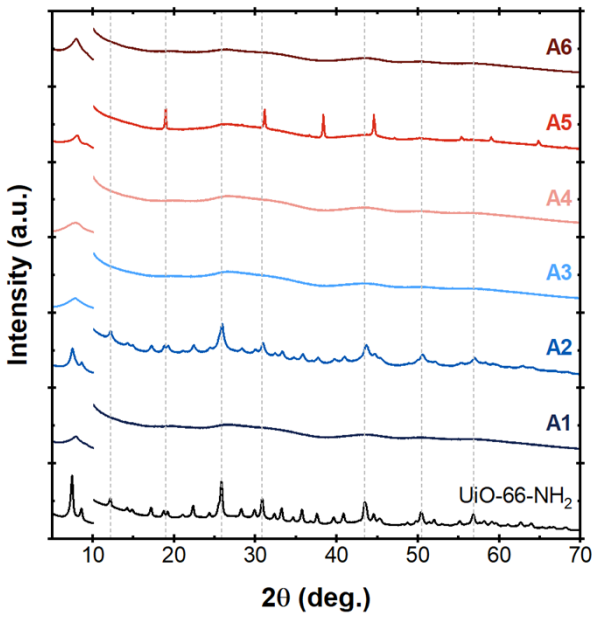

Figure S66. Powder patters of amide-functionalized MOFs **A1** – **A6** compared to the powder pattern of UiO-66-NH_2 (bottom).

Thermogravimetric Analysis

Thermogravimetric analysis was performed on all f-MOF samples prior to N_2 gas adsorption experiments to determine suitable heating conditions for MOF activation. The following data shows all f-MOFs are stable up to at least 200 °C, so this temperature was chosen for MOF activation prior to gas adsorption measurements.

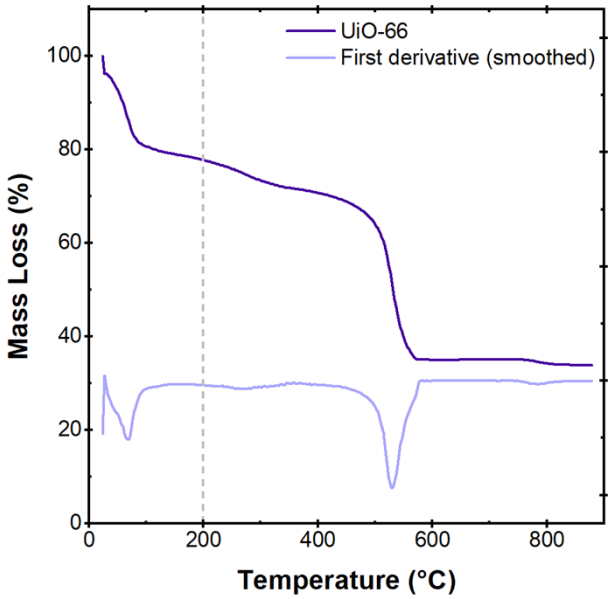

Figure S67. Thermogravimetric analysis of UiO-66 with the chosen activation temperature marked (200 °C).

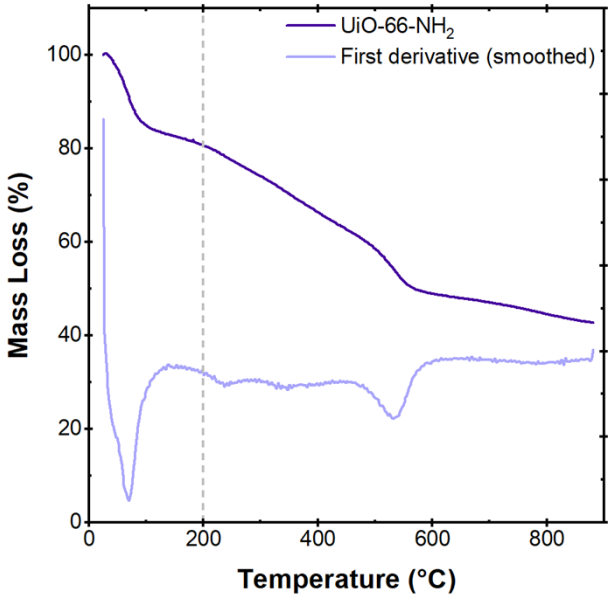

Figure S68. Thermogravimetric analysis of UiO-66-NH_2 with the chosen activation temperature marked (200 °C).

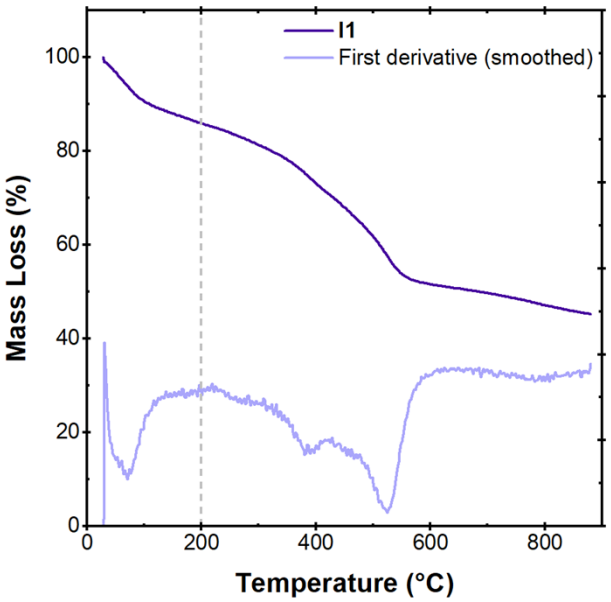

Figure S69. Thermogravimetric analysis of **I1** with the chosen activation temperature marked (200 °C).

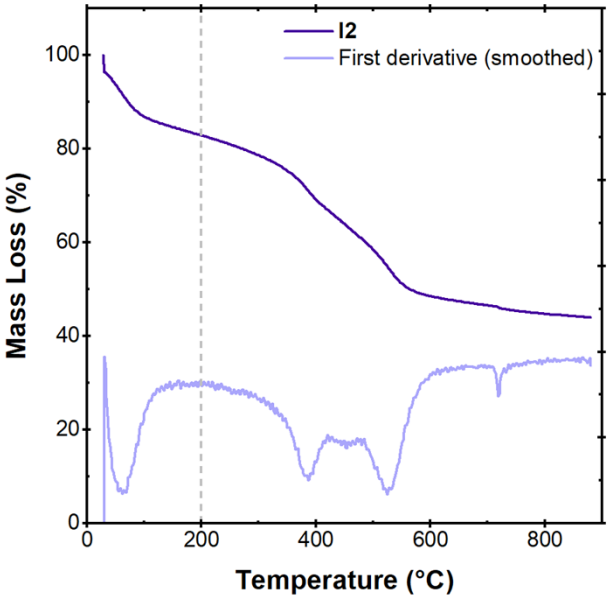

Figure S70. Thermogravimetric analysis of **I2** with the chosen activation temperature marked (200 °C).

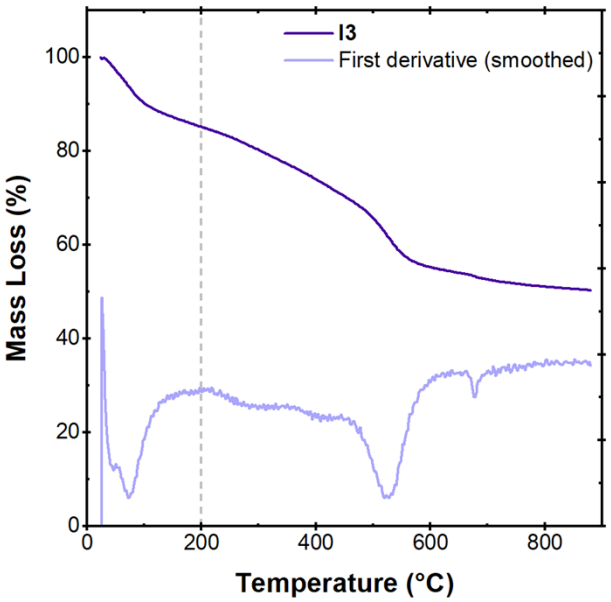

Figure S71. Thermogravimetric analysis of **I3** with the chosen activation temperature marked (200 °C).

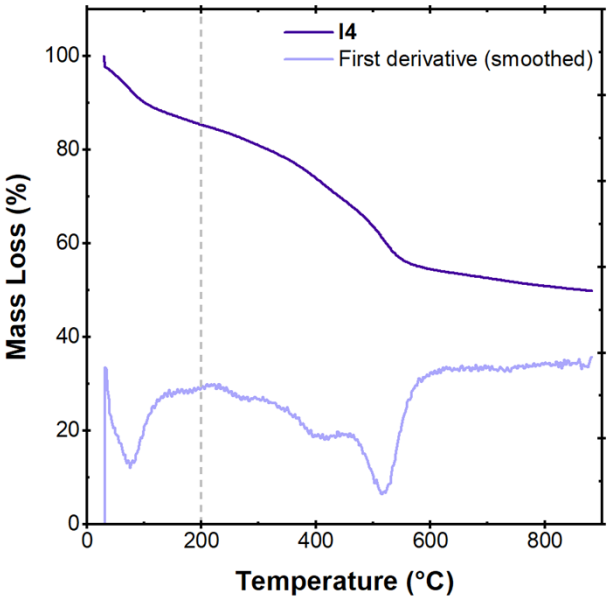

Figure S72. Thermogravimetric analysis of **I4** with the chosen activation temperature marked (200 °C).

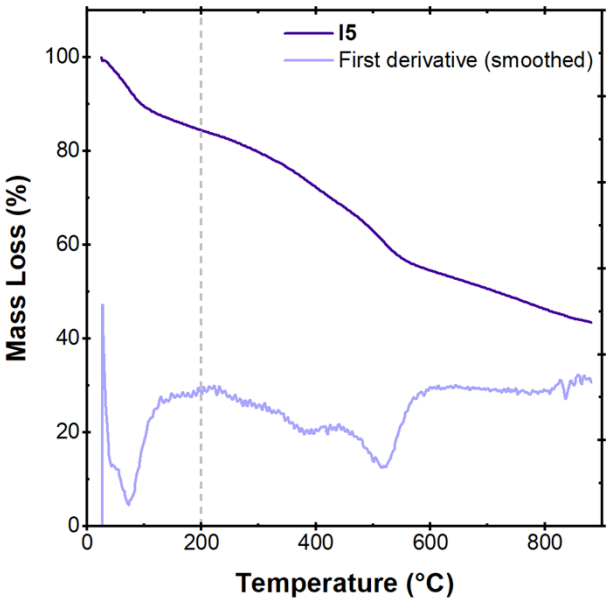

Figure S73. Thermogravimetric analysis of **I5** with the chosen activation temperature marked (200 °C).

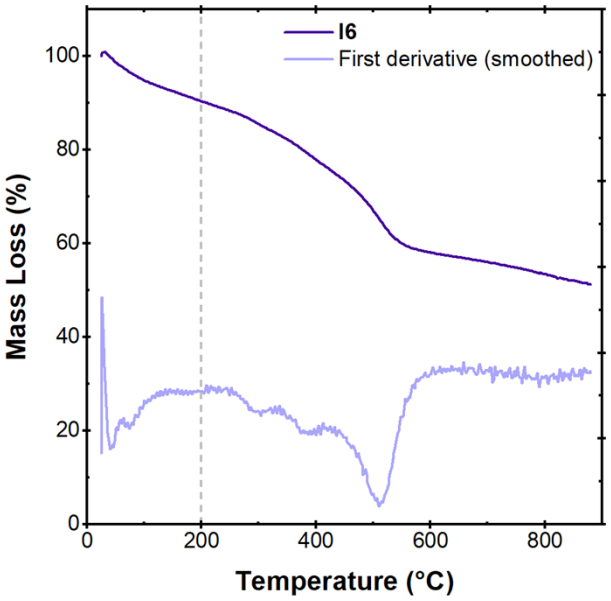

Figure S74. Thermogravimetric analysis of **I6** with the chosen activation temperature marked (200 °C).

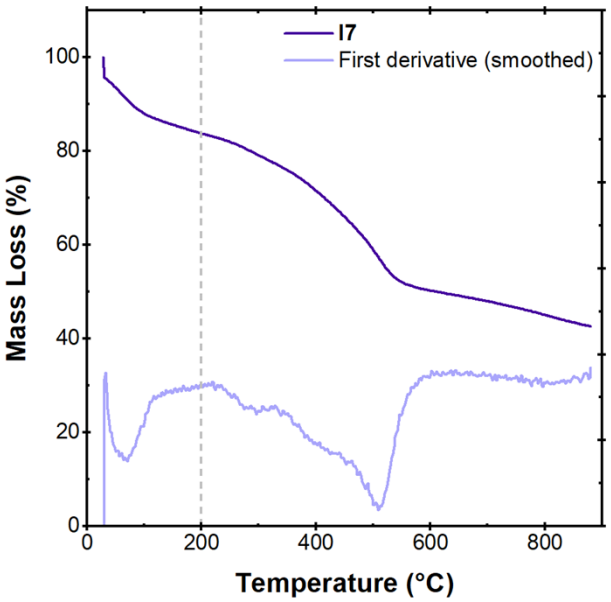

Figure S75. Thermogravimetric analysis of **I7** with the chosen activation temperature marked (200 °C).

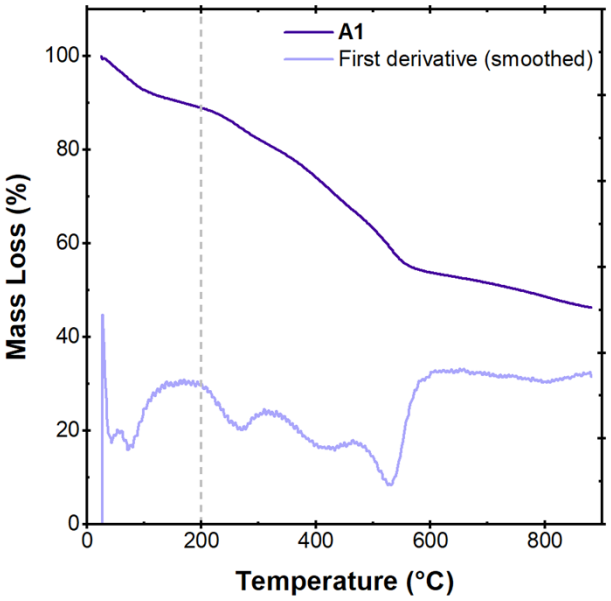

Figure S76. Thermogravimetric analysis of **A1** with the chosen activation temperature marked (200 °C).

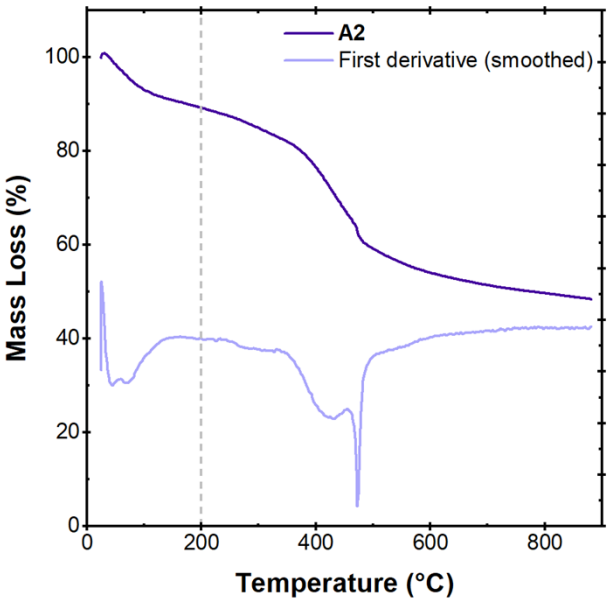

Figure S77. Thermogravimetric analysis of **A2** with the chosen activation temperature marked (200 °C).

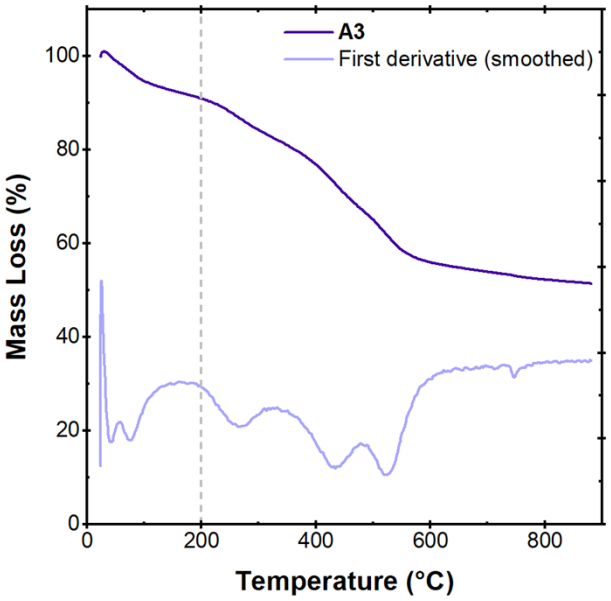

Figure S78. Thermogravimetric analysis of **A3** with the chosen activation temperature marked (200 °C).

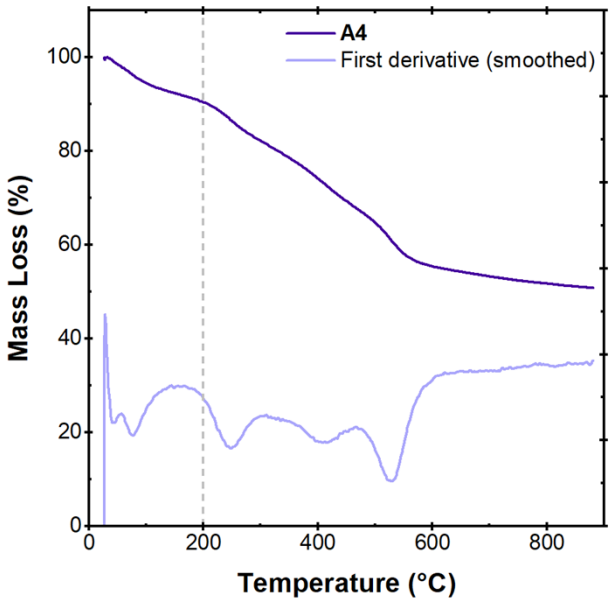

Figure S79. Thermogravimetric analysis of **A4** with the chosen activation temperature marked (200 °C).

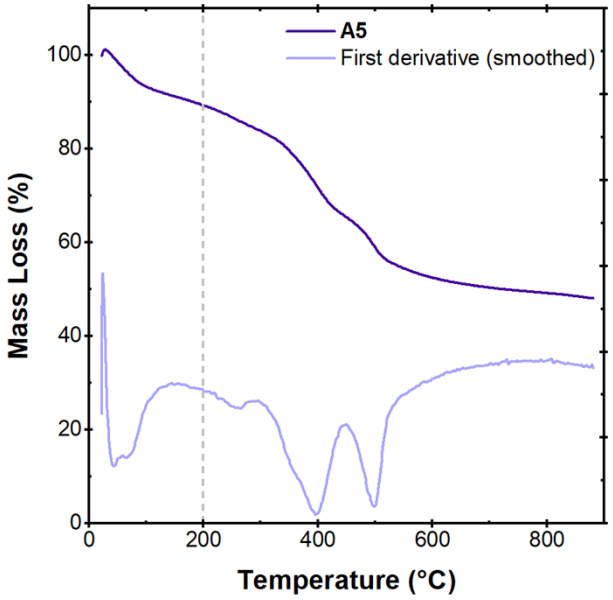

Figure S80. Thermogravimetric analysis of **A5** with the chosen activation temperature marked (200 °C).

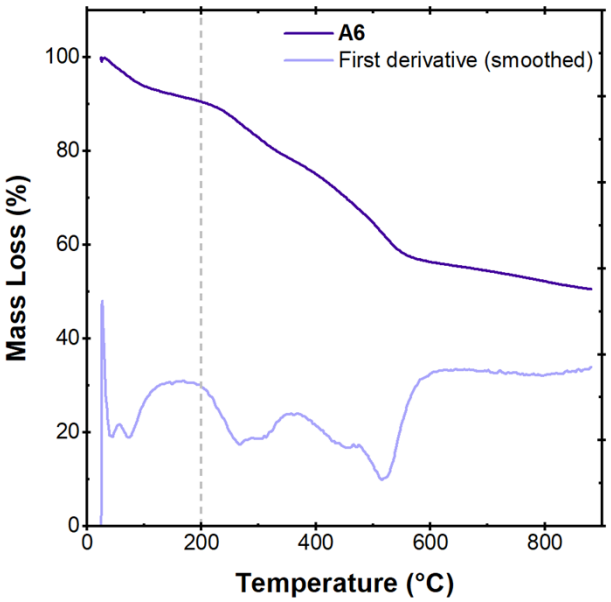

Figure S81. Thermogravimetric analysis of **A6** with the chosen activation temperature marked (200 °C).

Surface Area Measurement Nitrogen Gas Adsorption

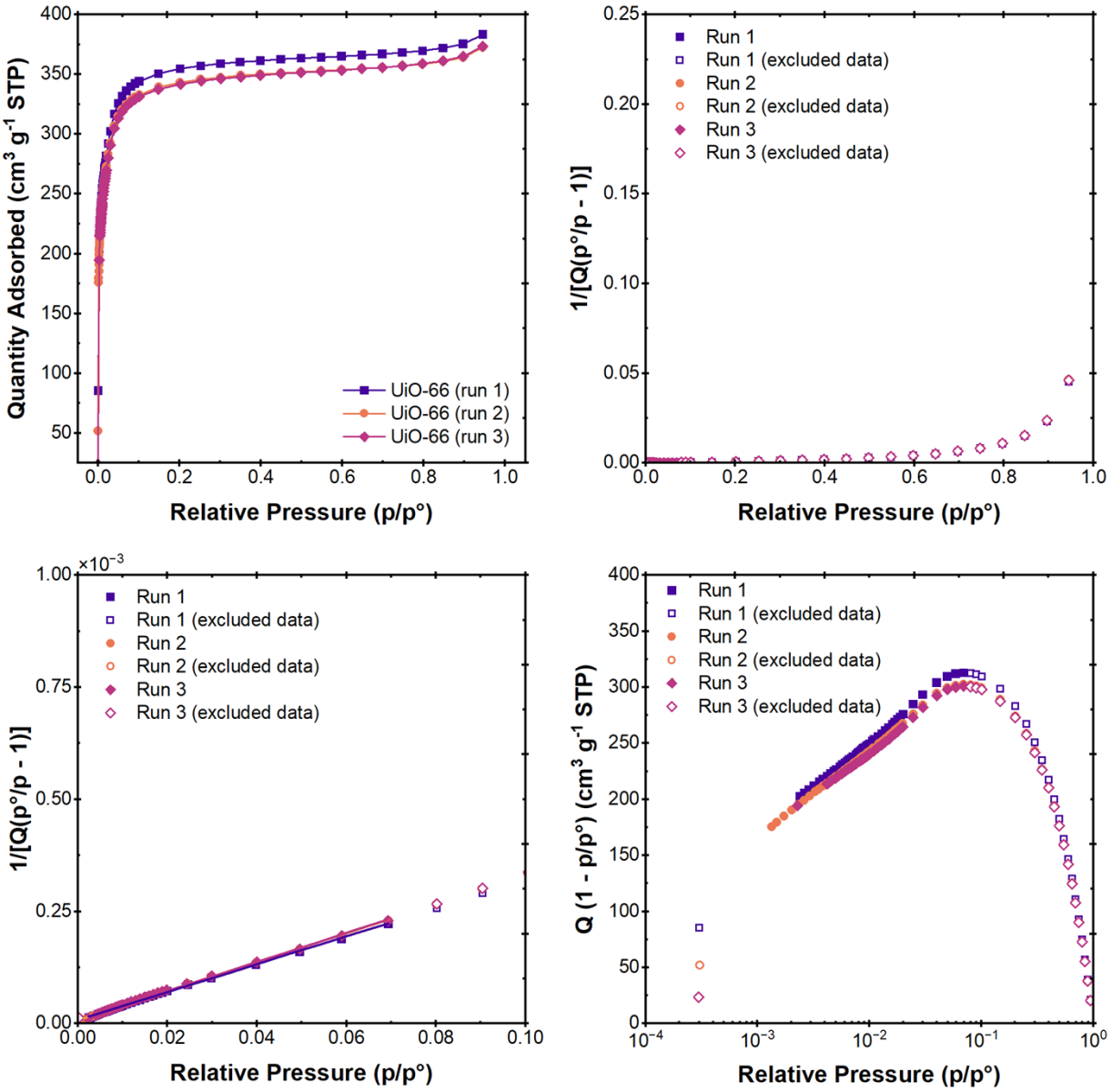

Figure S82. Nitrogen gas adsorption data for UiO-66 performed in triplicate. Adsorption isotherms (top left), BET surface area plots (full view, top right), BET surface area plots (zoomed-in on fitted data, bottom left), and Rouquerol BET plots (bottom right).

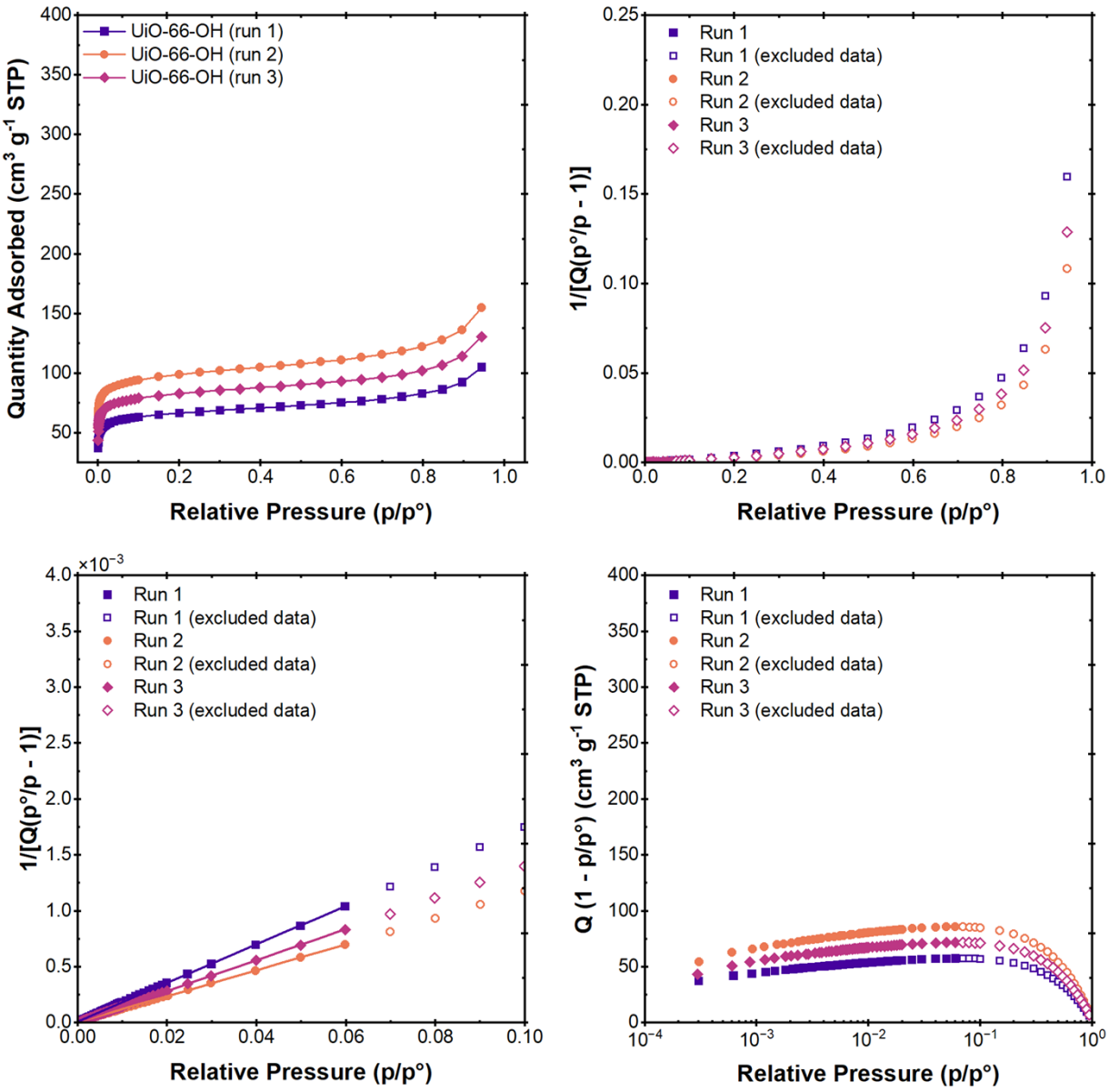

Figure S83. Nitrogen gas adsorption data for UiO-66-OH performed in triplicate. Adsorption isotherms (top left), BET surface area plots (full view, top right), BET surface area plots (zoomed-in on fitted data, bottom left), and Rouquerol BET plots (bottom right).

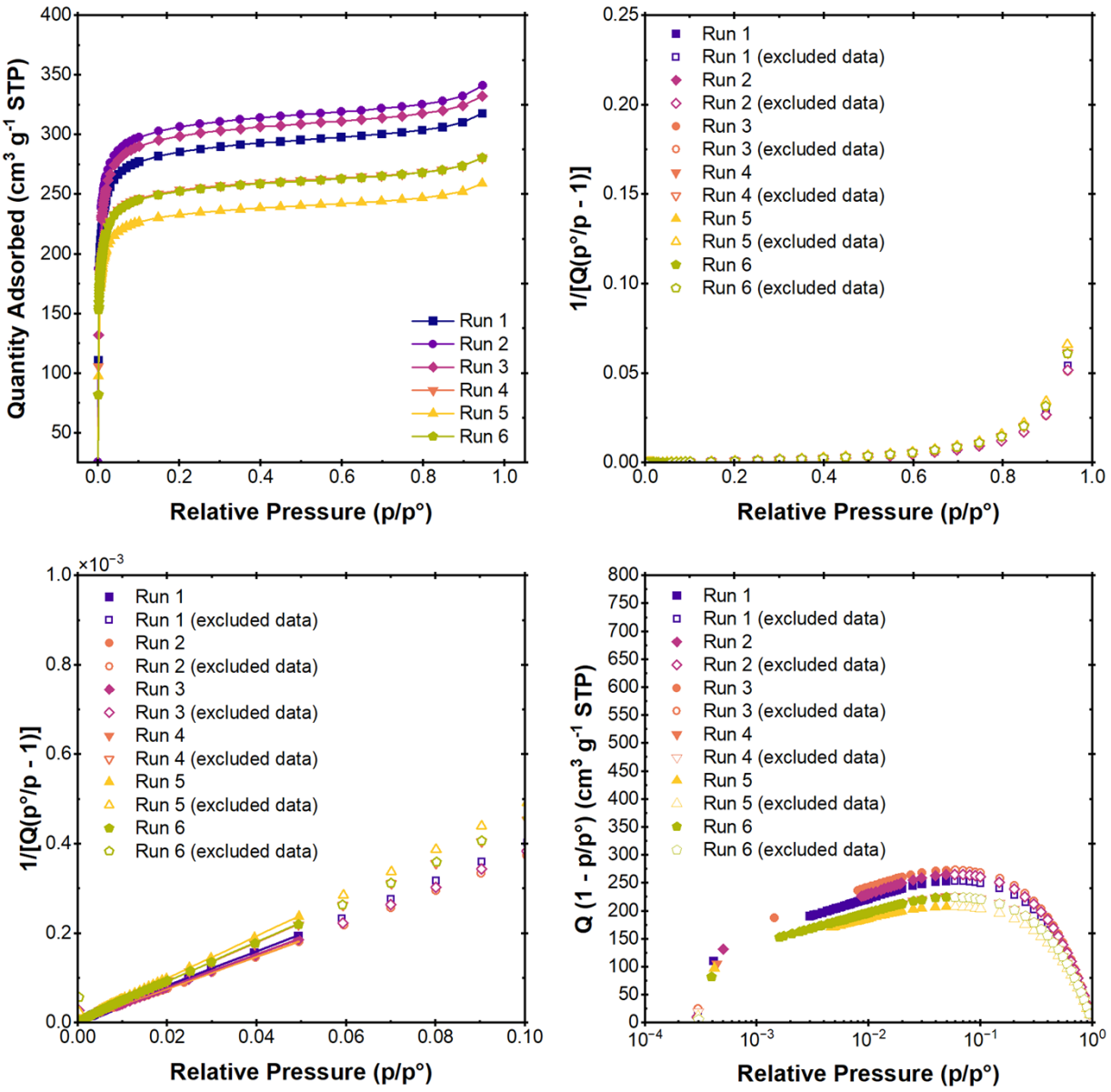

Figure S84. Nitrogen gas adsorption data for UiO-66-NH_2 performed for six replicates. Adsorption isotherms (top left), BET surface area plots (full view, top right), BET surface area plots (zoomed-in on fitted data, bottom left), and Rouquerol BET plots (bottom right).

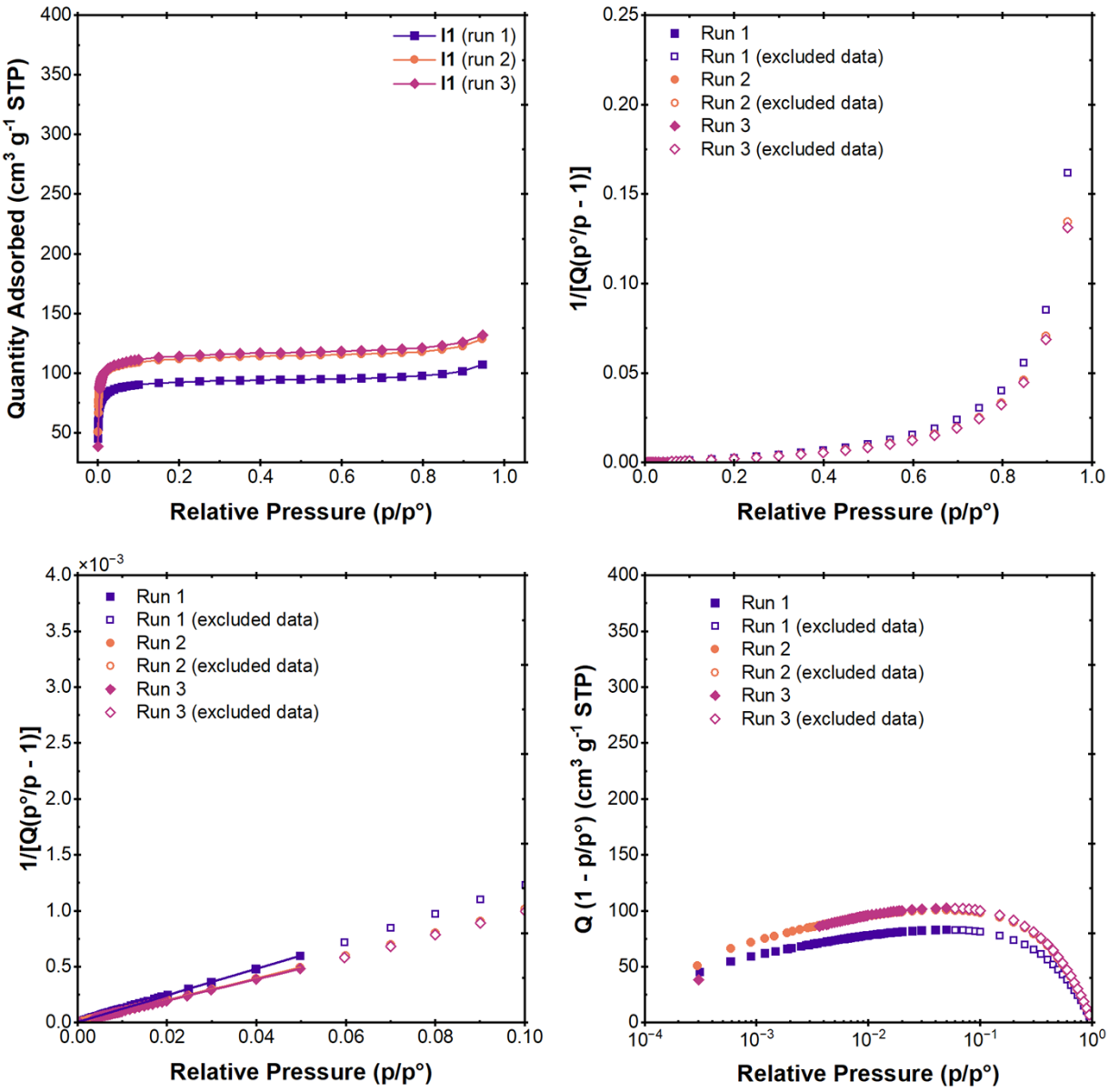

Figure S85. Nitrogen gas adsorption data for **I1** performed in triplicate. Adsorption isotherms (top left), BET surface area plots (full view, top right), BET surface area plots (zoomed-in on fitted data, bottom left), and Rouquerol BET plots (bottom right).

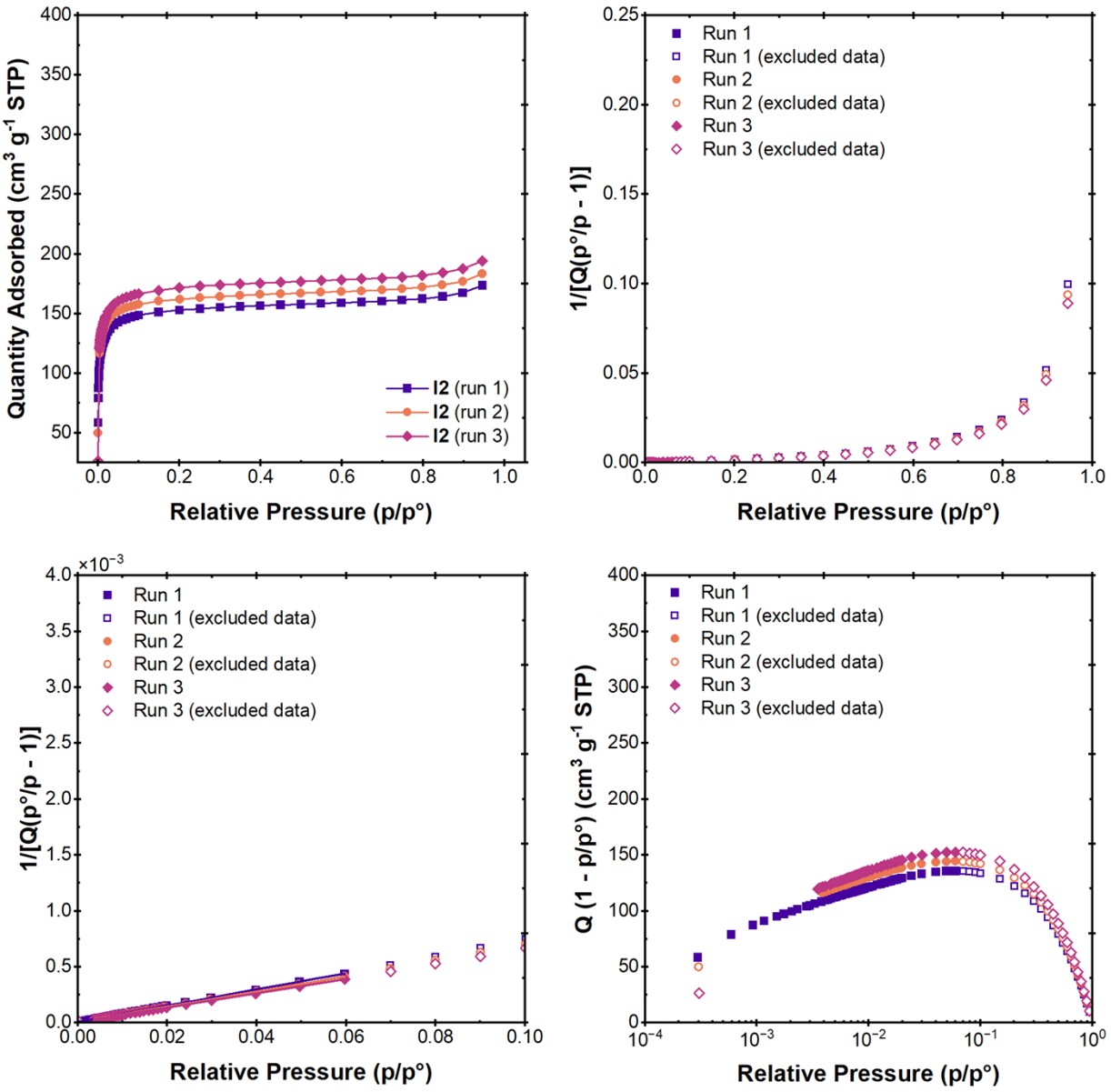

Figure S86. Nitrogen gas adsorption data for **I2** performed in triplicate. Adsorption isotherms (top left), BET surface area plots (full view, top right), BET surface area plots (zoomed-in on fitted data, bottom left), and Rouquerol BET plots (bottom right).

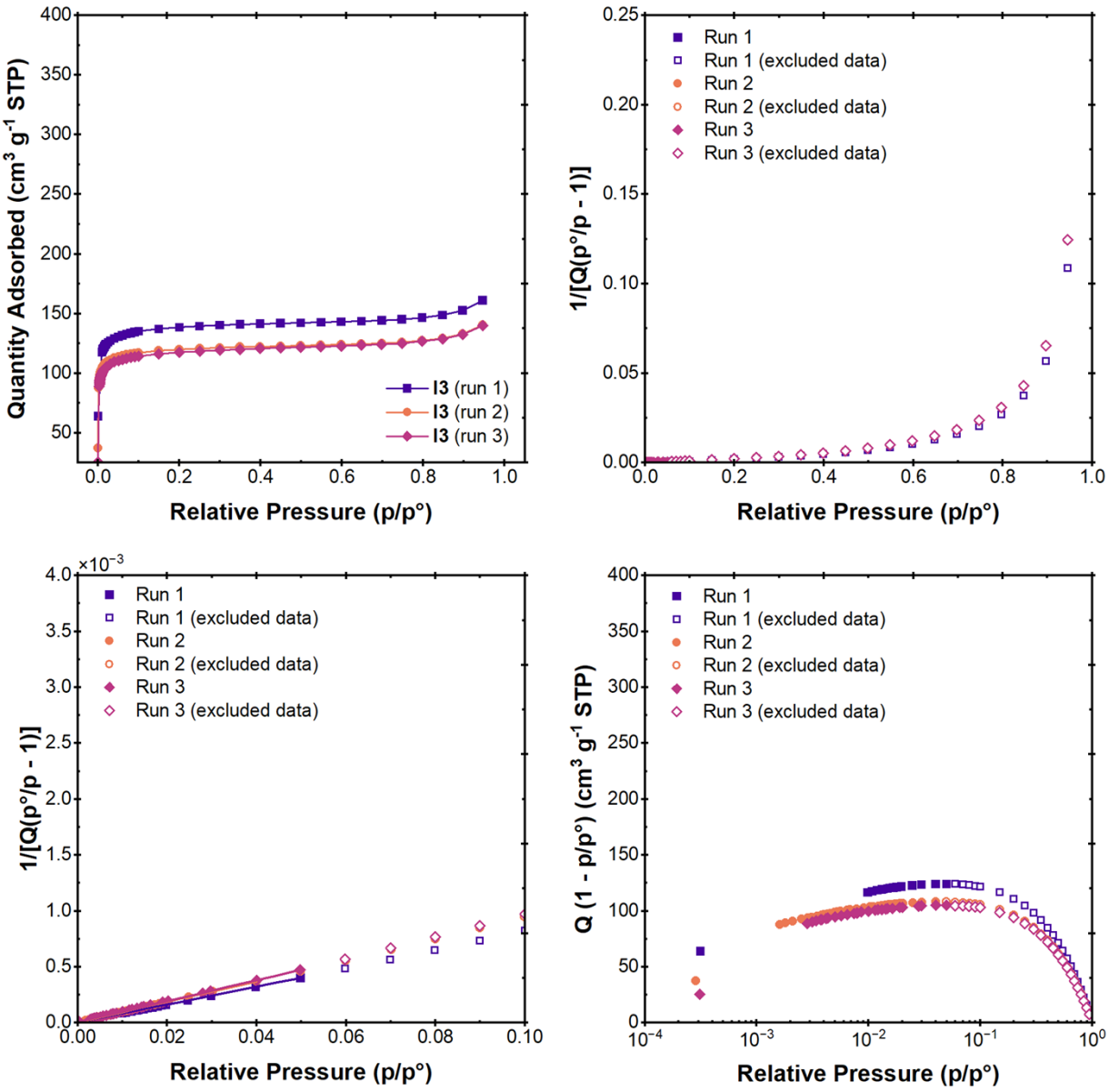

Figure S87. Nitrogen gas adsorption data for **I3** performed in triplicate. Adsorption isotherms (top left), BET surface area plots (full view, top right), BET surface area plots (zoomed-in on fitted data, bottom left), and Rouquerol BET plots (bottom right).

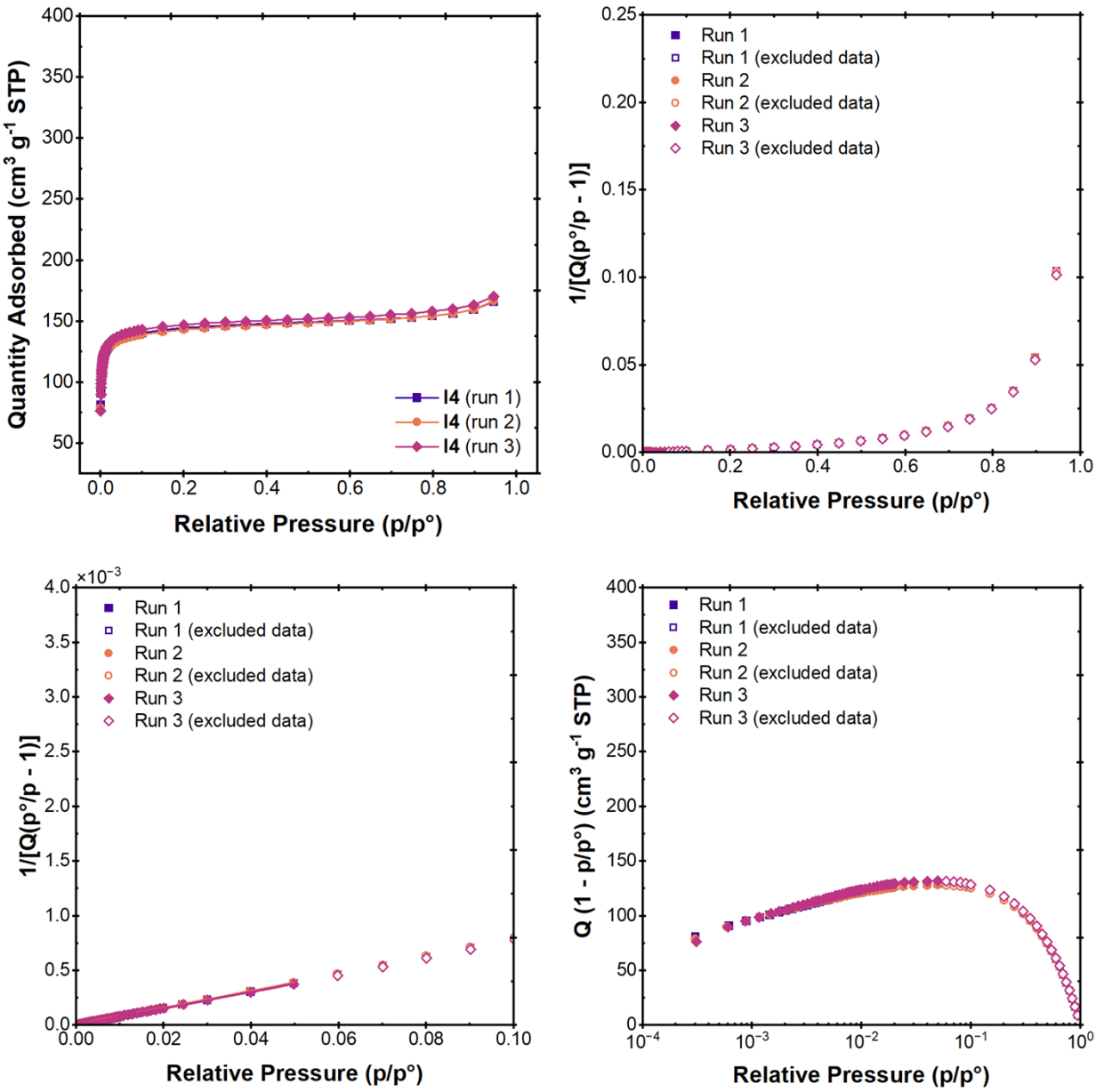

Figure S88. Nitrogen gas adsorption data for **I4** performed in triplicate. Adsorption isotherms (top left), BET surface area plots (full view, top right), BET surface area plots (zoomed-in on fitted data, bottom left), and Rouquerol BET plots (bottom right).

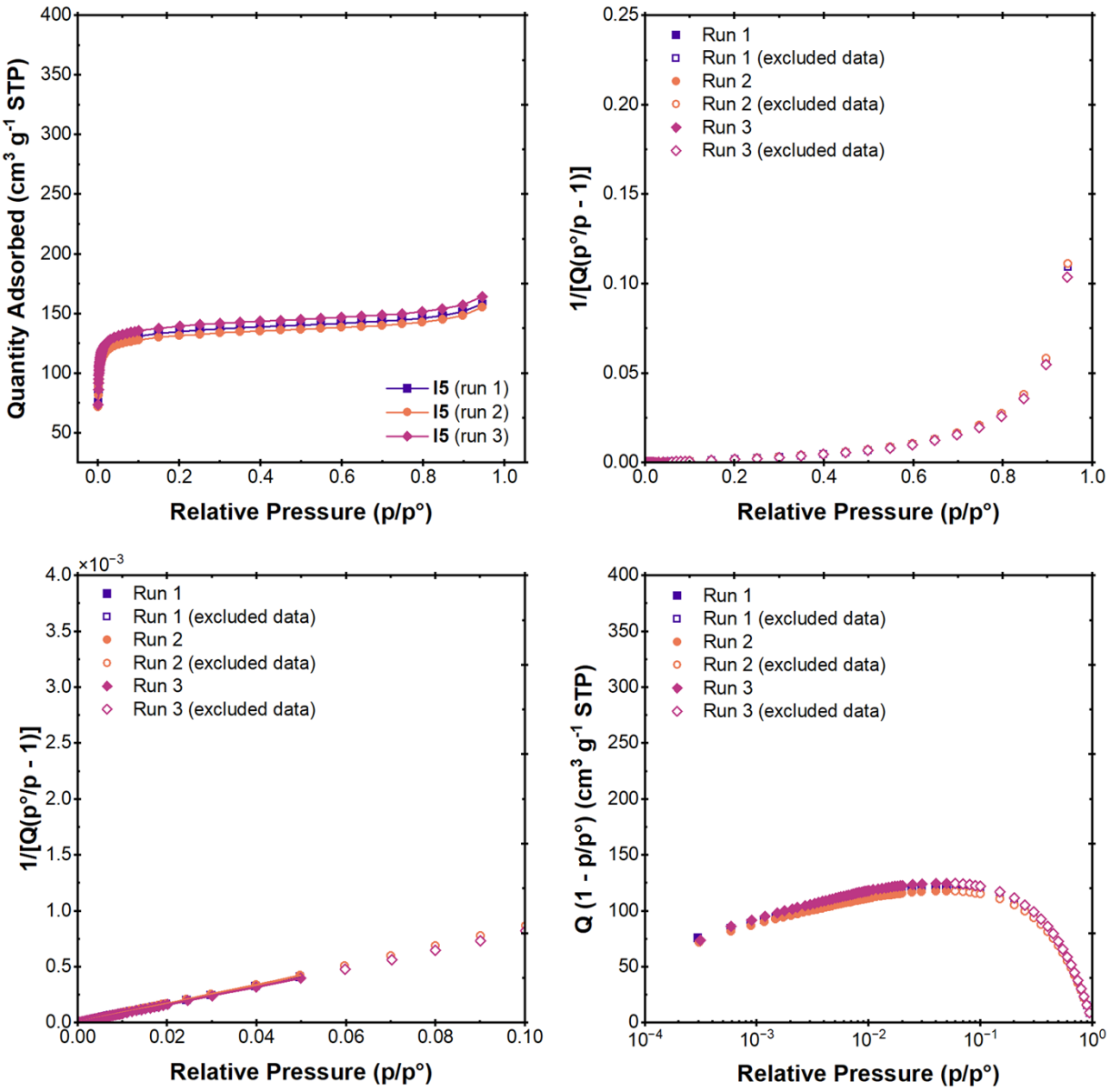

Figure S89. Nitrogen gas adsorption data for **I5** performed in triplicate. Adsorption isotherms (top left), BET surface area plots (full view, top right), BET surface area plots (zoomed-in on fitted data, bottom left), and Rouquerol BET plots (bottom right).

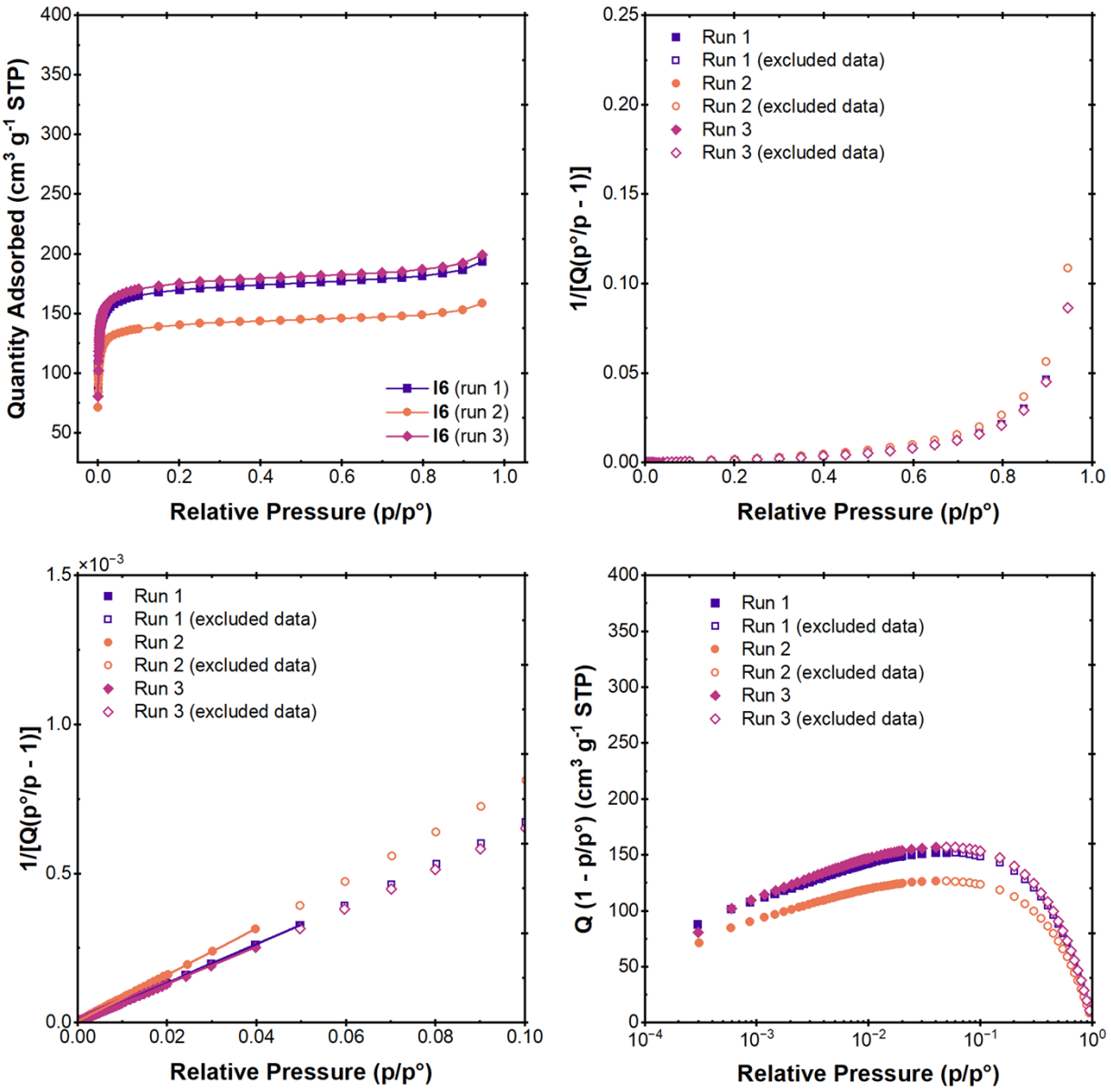

Figure S90. Nitrogen gas adsorption data for **I6** performed in triplicate. Adsorption isotherms (top left), BET surface area plots (full view, top right), BET surface area plots (zoomed-in on fitted data, bottom left), and Rouquerol BET plots (bottom right).

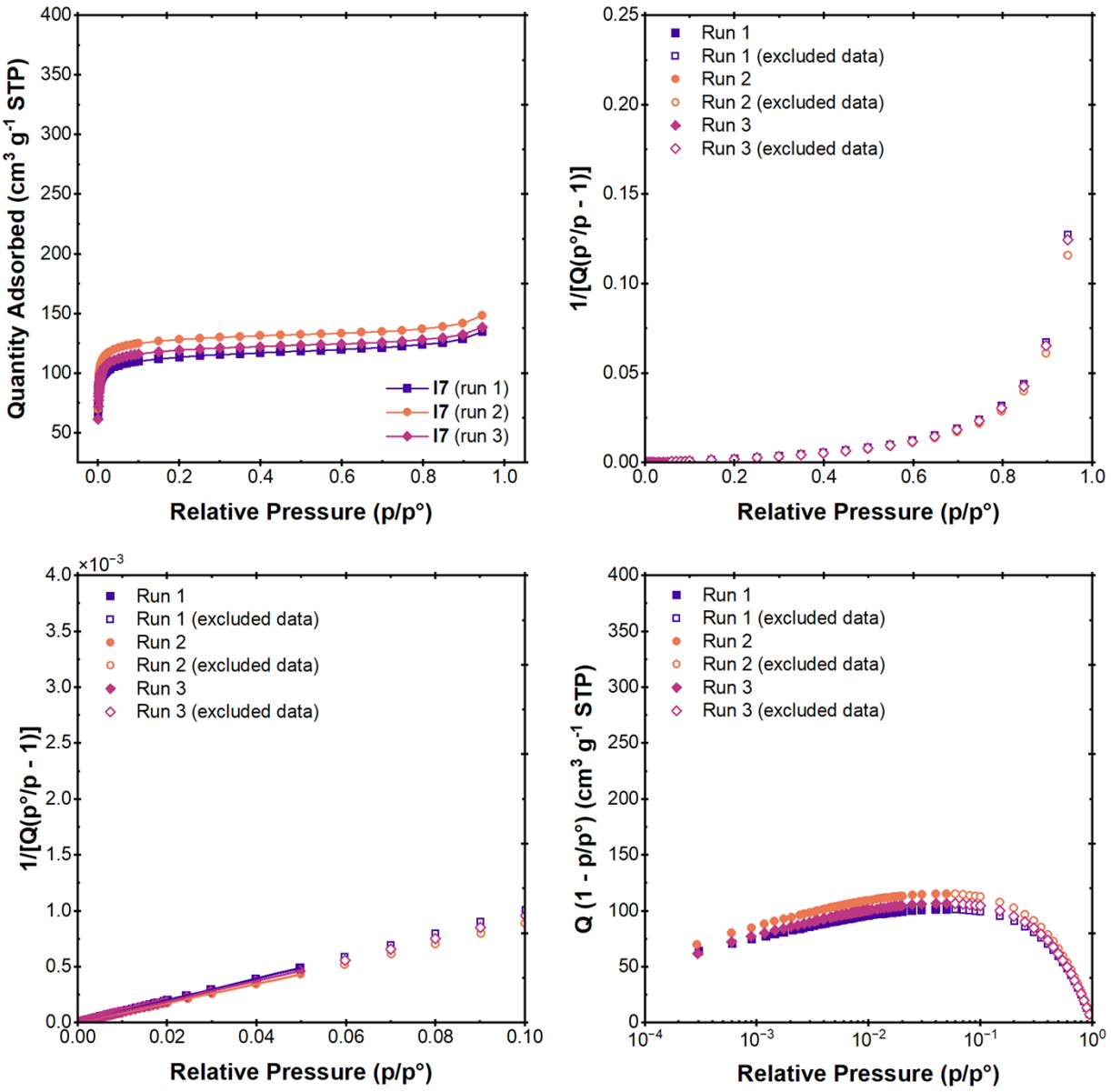

Figure S91. Nitrogen gas adsorption data for **I7** performed in triplicate. Adsorption isotherms (top left), BET surface area plots (full view, top right), BET surface area plots (zoomed-in on fitted data, bottom left), and Rouquerol BET plots (bottom right).

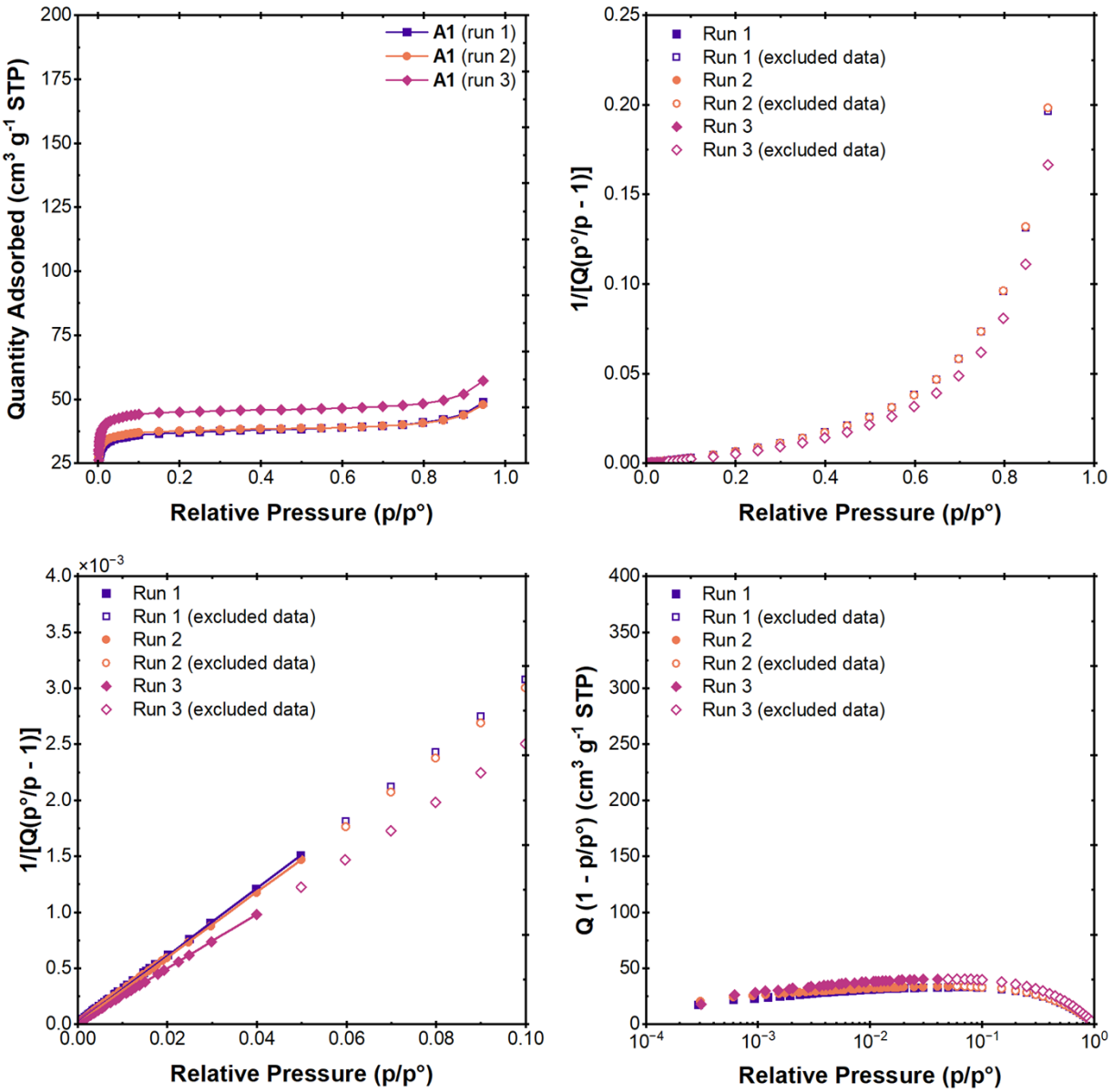

Figure S92. Nitrogen gas adsorption data for **A1** performed in triplicate. Adsorption isotherms (top left), BET surface area plots (full view, top right), BET surface area plots (zoomed-in on fitted data, bottom left), and Rouquerol BET plots (bottom right).

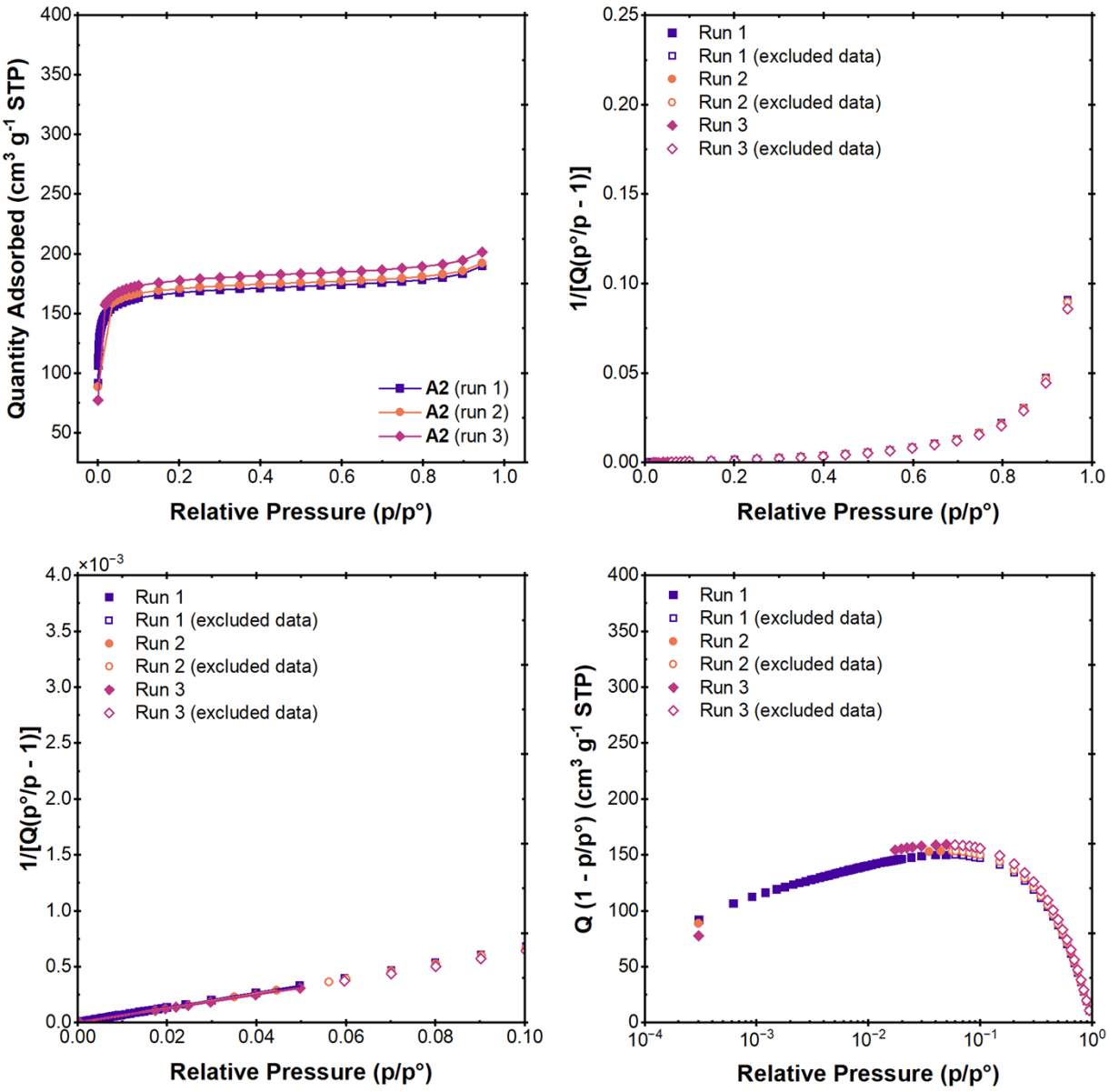

Figure S93. Nitrogen gas adsorption data for **A2** performed in triplicate. Adsorption isotherms (top left), BET surface area plots (full view, top right), BET surface area plots (zoomed-in on fitted data, bottom left), and Rouquerol BET plots (bottom right).

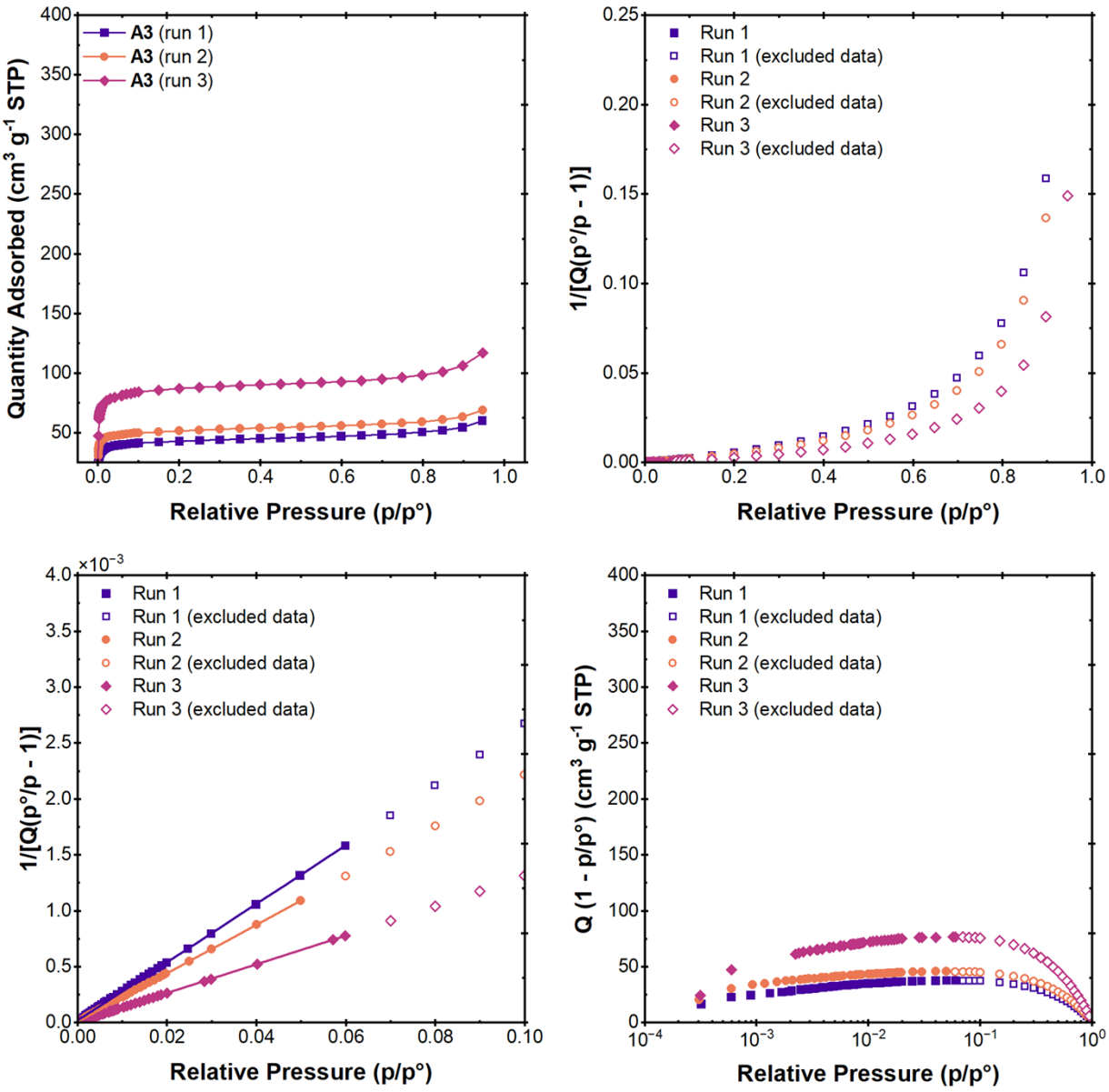

Figure S94. Nitrogen gas adsorption data for **A3** performed in triplicate. Adsorption isotherms (top left), BET surface area plots (full view, top right), BET surface area plots (zoomed-in on fitted data, bottom left), and Rouquerol BET plots (bottom right).

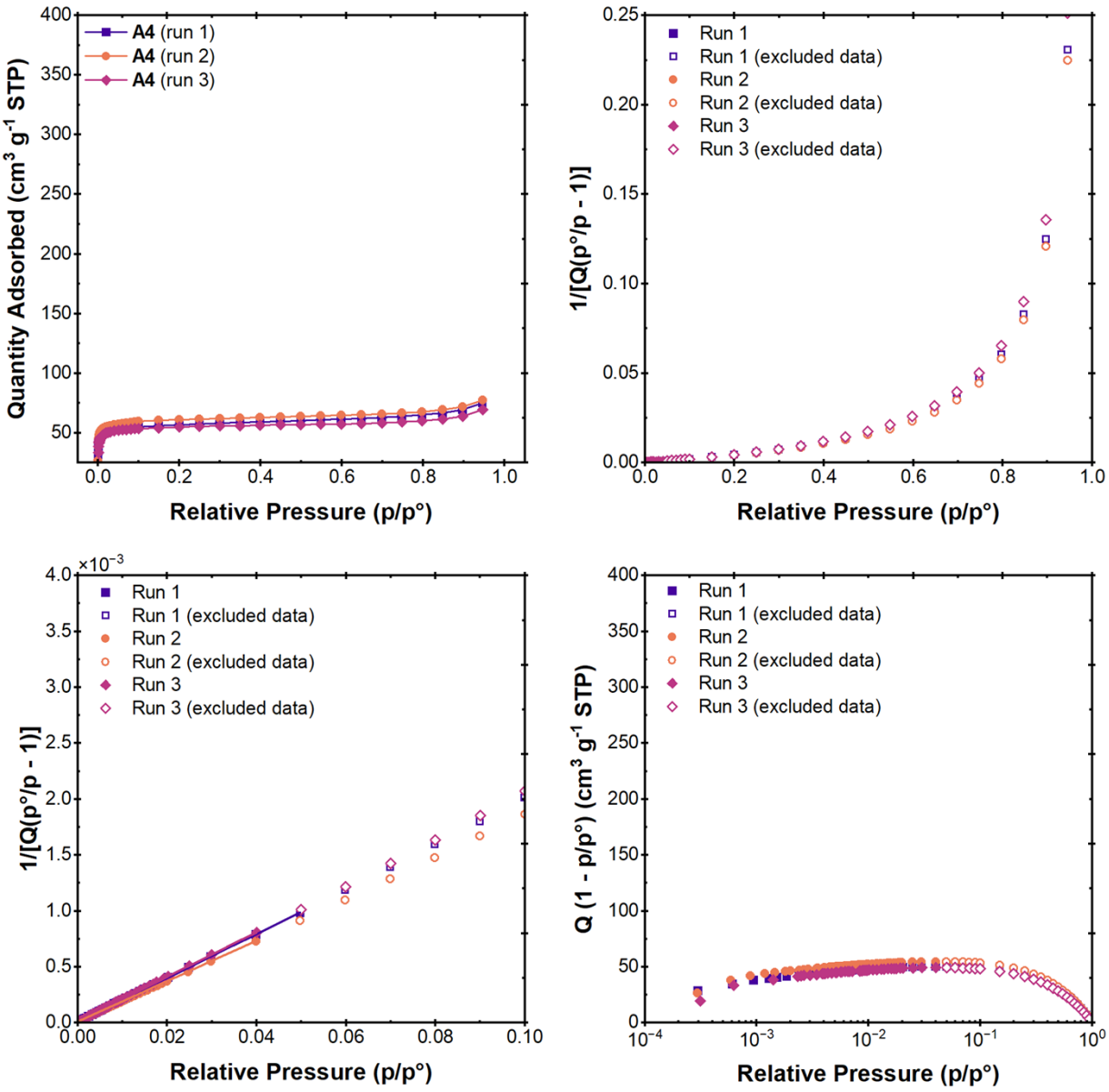

Figure S95. Nitrogen gas adsorption data for **A4** performed in triplicate. Adsorption isotherms (top left), BET surface area plots (full view, top right), BET surface area plots (zoomed-in on fitted data, bottom left), and Rouquerol BET plots (bottom right).

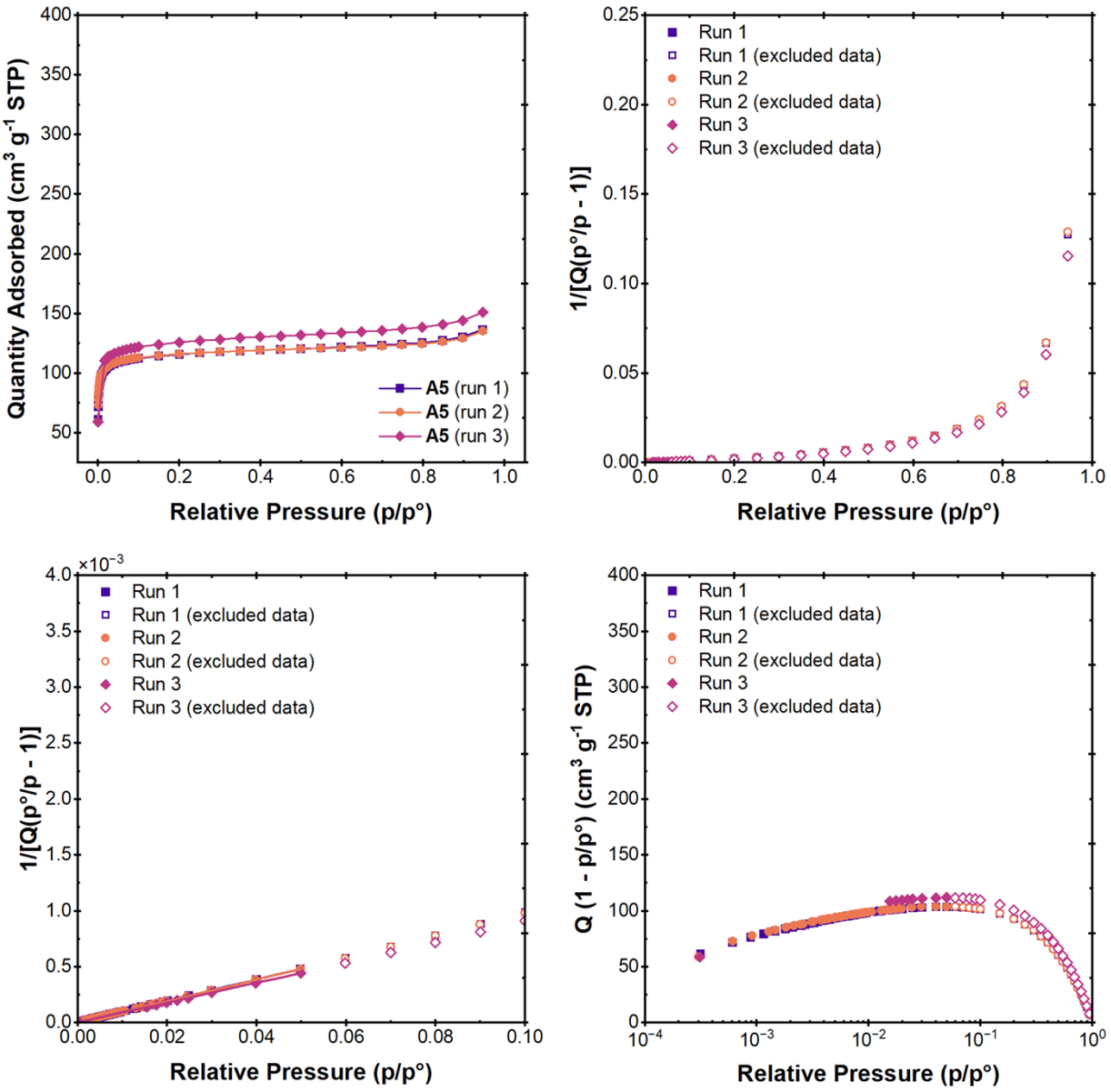

Figure S96. Nitrogen gas adsorption data for **A5** performed in triplicate. Adsorption isotherms (top left), BET surface area plots (full view, top right), BET surface area plots (zoomed-in on fitted data, bottom left), and Rouquerol BET plots (bottom right).

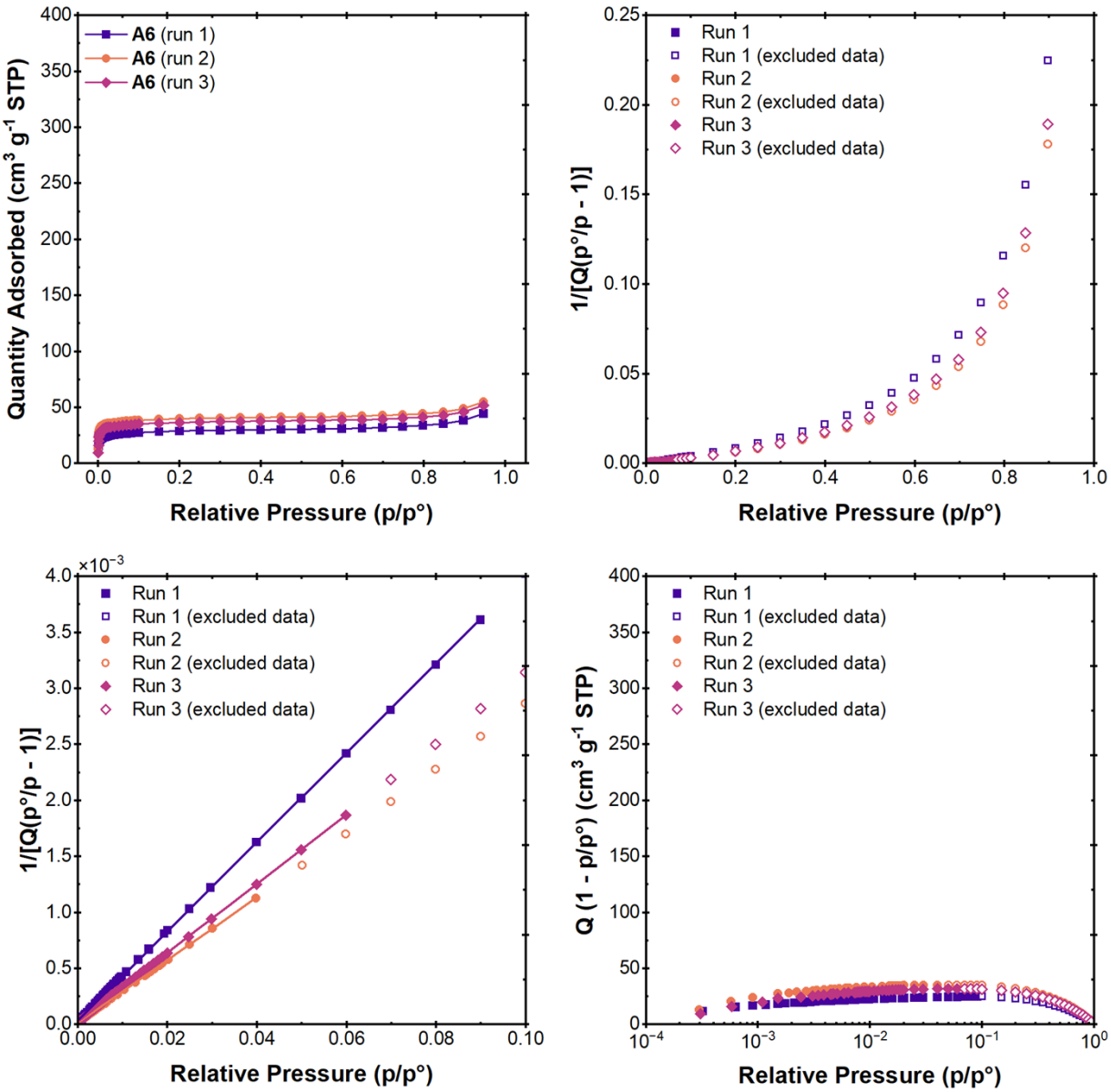

Figure S97. Nitrogen gas adsorption data for **A6** performed in triplicate. Adsorption isotherms (top left), BET surface area plots (full view, top right), BET surface area plots (zoomed-in on fitted data, bottom left), and Rouquerol BET plots (bottom right).

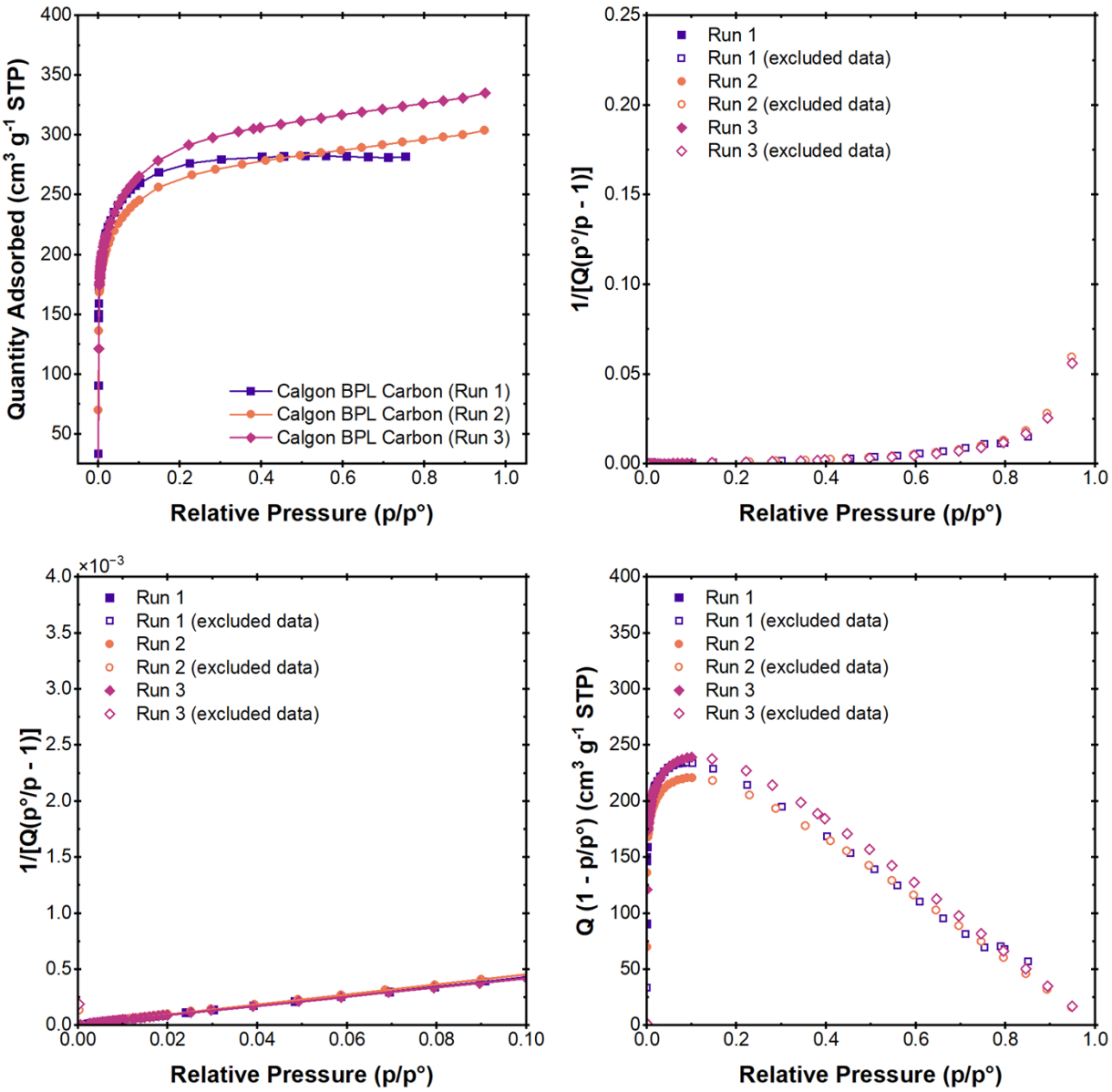

Figure S98. Nitrogen gas adsorption data for Calgon BPL Carbon performed in triplicate. Adsorption isotherms (top left), BET surface area plots (full view, top right), BET surface area plots (zoomed-in on fitted data, bottom left), and Rouquerol BET plots (bottom right).

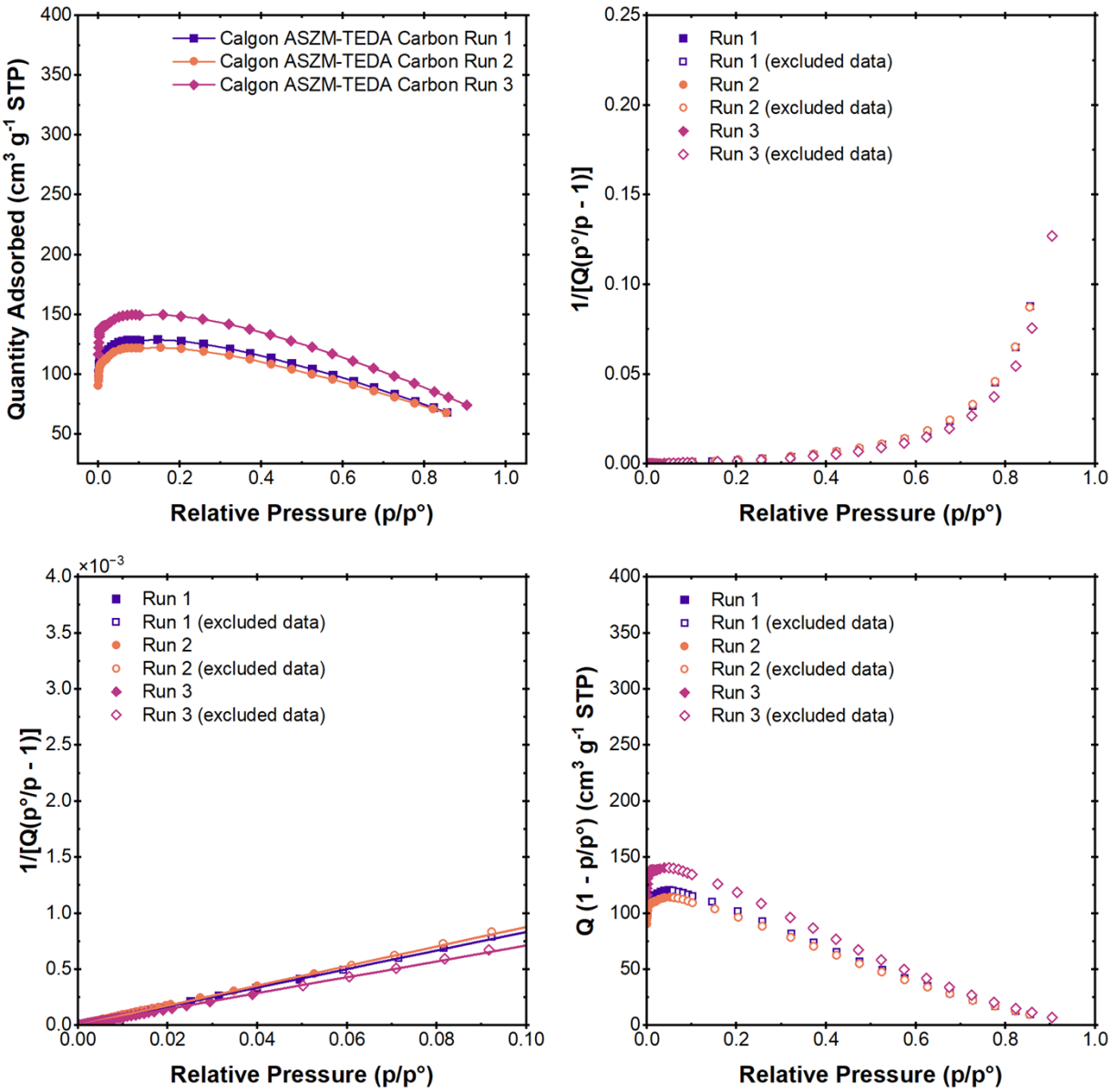

Figure S99. Nitrogen gas adsorption data for Calgon ASZM-TEDA Carbon performed in triplicate. Adsorption isotherms (top left), BET surface area plots (full view, top right), BET surface area plots (zoomed-in on fitted data, bottom left), and Rouquerol BET plots (bottom right).

Measurement of DMMP Uptake Capacity

QCM sensors (10 MHz) were cleaned by first treating them in an oxygen plasma chamber on a high setting for 10 minutes. The sensors were then placed in a solution of 5:1:1 DI water, 25% aqueous NH_4OH, and 30% H_2O_2. The solution was heated to 75 °C and the sensors allowed to soak for 5 min. The sensors were washed immediately washed with DI water and dried under compressed air. A final treatment in an oxygen plasma chamber was performed on a high setting for 10 minutes, and the sensors were stored in sealed containers until further use.

Prior to coating the sensors, their oscillation frequencies were measured under dry air flow. Coating of the sensors with each MOF was then performed according a published literature procedure.[6] Suspensions of each MOF were prepared by sonicating 5 mg mL^{-1} in ethanol for 5h. A small amount (10 μL) was drop-cast onto each sensor and the solvent allowed to evaporate. The coated sensors were dried in a vacuum oven overnight at 120 °C and their oscillation frequencies remeasured to determine the quantity of each MOF deposited. Sensors were then stored in a vacuum oven at 120 °C prior to DMMP exposure experiments.

The data from these experiments is provided in Table SA and in the subsequent figures. The raw data (change in oscillation frequency, Δf) was converted to mass change (Δm) by use of the modified Saurbrey equation (Eq. 1).[7] A value of 4.4 ng cm^{-2} was used for the mass sensitivity constant (C) of the 10 MHz QCM sensors, and the first harmonic (n=1) was used.

$$\Delta m = \frac{-C * \Delta f}{n} \qquad \text{Eq. 1}$$

Vapor delivery was achieved by first generating a saturated DMMP vapor steam by flowing dry air at a rate of 4 mL min^{-1} through the headspace of a container filled with DMMP liquid. The temperature of the liquid was maintained at 25 °C using a thermostatted oil bath. The saturated vapor was exhausted to a fume hood while the signal from the QCM sensor was stabilized at 1 mL min^{-1}. Once a stable baseline was achieved, the gas stream was switched to the saturated DMMP vapor, which was split among 4 parallel sensor compartments maintained at 25 °C for simultaneous measurement of 4 separate samples. The flow rate for each sensor was 1 mL min^{-1}, equivalent to the dry air gas stream used for stabilization prior to the experiment. The sensors were exposed to DMMP vapor for 30 min, followed by dry air for 1 h prior to repetition of the experiment.

Table S1. Frequency changes and calculated data obtained from QCM experiments probing DMMP adsorption in MOF sorbents.

Sample	Run	f_{clean} (Hz)	f_{MOF} (Hz)	f_{DMMP} (Hz)	m_{MOF} (ng)	m_{DMMP} (ng)	Capacity (mg_{DMMP} / $g_{Sorbent}$)	Normalized Capacity (μmol_{DMMP} m^{-2})
UiO-66	1	10009024	9998910	9998737	44502	761	0.138	0.101
	2	10009024	9998859	9998712	44726	647	0.117	0.086
	3	10009024	9998846	9998703	44783	629	0.113	0.083
UiO-66-NH_2	1	10014729	10009472	10009380	23131	405	0.141	0.455
	2	10014729	10009441	10009361	23267	352	0.122	0.393
	3	10014729	10009430	10009358	23316	317	0.110	0.353
UiO-66-OH	1	10004836	9989233	9988827	68653	1786	0.210	0.194
	2	10004836	9988978	9988735	69775	1069	0.123	0.114
	3	10004836	9988909	9988758	70079	664	0.076	0.071
I1	1	10008384	10004769	10004730	15906	172	0.087	0.207
	2	10008384	10004754	10004717	15972	163	0.082	0.196
	3	10008384	10004745	10004708	16012	163	0.082	0.195
I2	1	10007229	10000931	10000852	27711	348	0.101	0.158
	2	10007229	10000919	10000832	27764	383	0.111	0.174
	3	10007229	10000896	10000817	27865	348	0.101	0.157
I3	1	10010528	9999185	9998791	49909	1734	0.280	0.560
	2	10010528	9999191	9998747	49883	1954	0.316	0.631
	3	10010528	9999229	9998739	49716	2156	0.350	0.699
I4	1	10008319	9995512	9995294	56351	959	0.137	0.241
	2	10008319	9995504	9995298	56386	906	0.130	0.227
	3	10008319	9995549	9995289	56188	1144	0.164	0.288
I5	1	10011663	10005207	10005145	28406	273	0.077	0.146
	2	10011663	10005238	10005145	28270	409	0.117	0.220
	3	10011663	10005243	10005138	28248	462	0.132	0.249
I6	1	9994679	9978149	9978100	72732	216	0.024	0.037
	2	9994679	9978137	9978080	72785	251	0.028	0.043
	3	9994679	9978133	9978068	72802	286	0.032	0.049
I7	1	9994602	9983840	9983599	47353	1060	0.180	0.384
	2	9994602	9983761	9983577	47700	810	0.137	0.291
	3	9994602	9983723	9983568	47868	682	0.115	0.244
A1	1	10011346	10001990	10001943	41166	207	0.040	0.253
	2	10011346	10002005	10001937	41100	299	0.059	0.367
	3	10011346	10002000	10001925	41122	330	0.065	0.404
A2	1	9997779	9993315	9993282	19642	145	0.060	0.088
	2	9997779	9993304	9993273	19690	136	0.056	0.082
	3	9997779	9993298	9993266	19716	141	0.058	0.085
A3	1	10011110	10001039	10000963	44312	334	0.061	0.253
	2	10011110	10001052	10000953	44255	436	0.079	0.331
	3	10011110	10001051	10000945	44260	466	0.085	0.354
A4	1	9994249	9989934	9989907	18986	119	0.050	0.219
	2	9994249	9989927	9989900	19017	119	0.050	0.219
	3	9994249	9989923	9989898	19034	110	0.047	0.202
A5	1	10015745	10010787	10010711	21815	334	0.124	0.263
	2	10015745	10010776	10010701	21864	330	0.122	0.259
	3	10015745	10010781	10010703	21842	343	0.127	0.269
A6	1	10003187	9989904	9989652	58445	1109	0.153	1.092
	2	10003187	9989771	9989607	59030	722	0.099	0.704
	3	10003187	9989690	9989570	59387	528	0.072	0.512

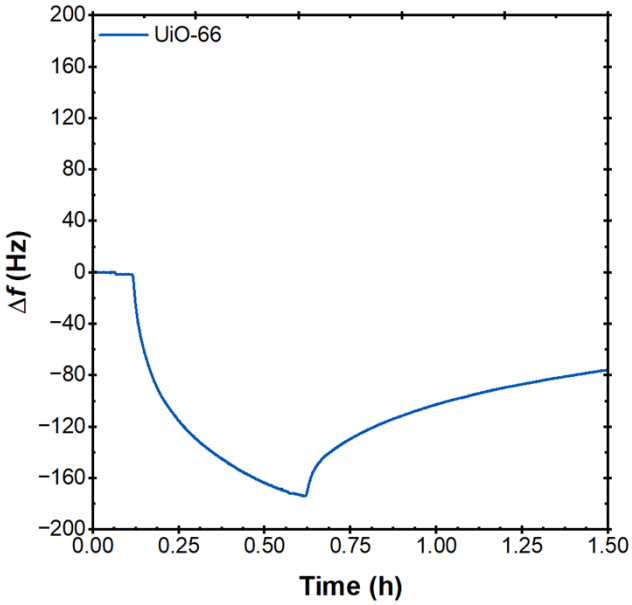

Figure S100. QCM data following the adsorption of DMMP in UiO-66.

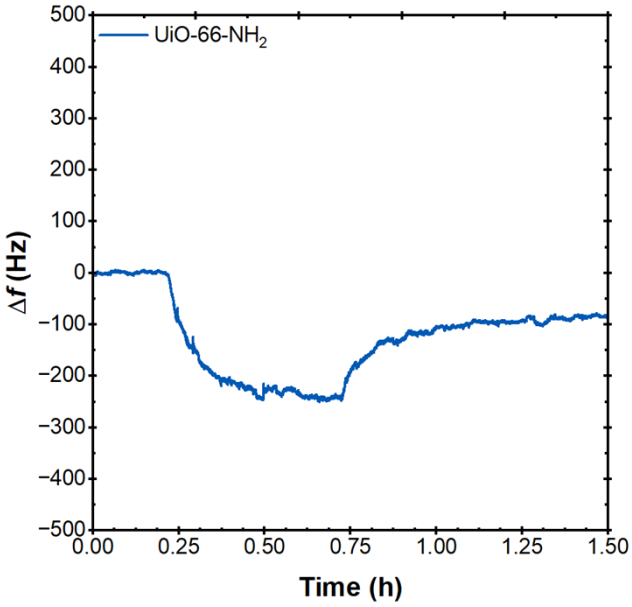

Figure S101. QCM data following the adsorption of DMMP in UiO-66-NH_2.

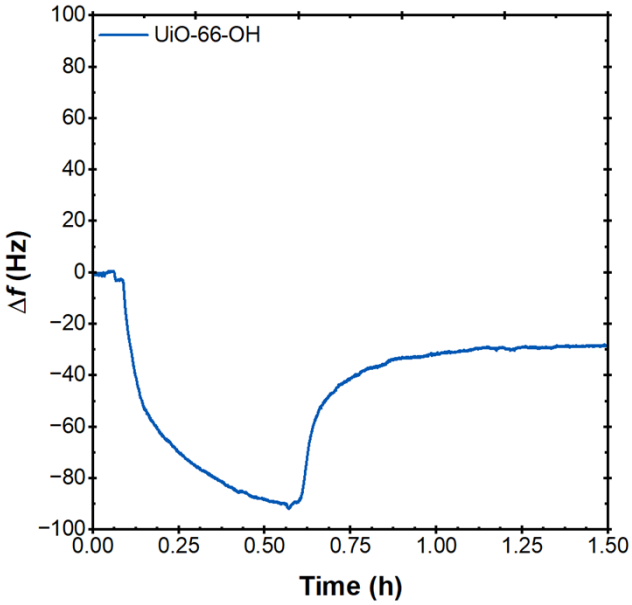

Figure S102. QCM data following the adsorption of DMMP in UiO-66-OH.

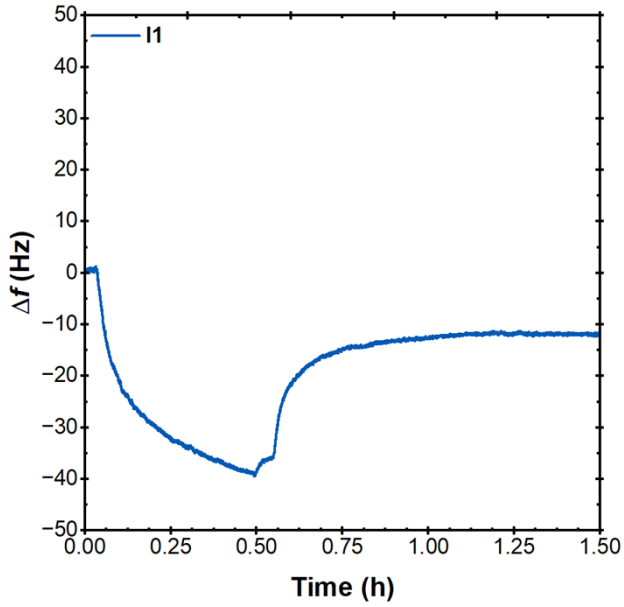

Figure S103. QCM data following the adsorption of DMMP in **I1**.

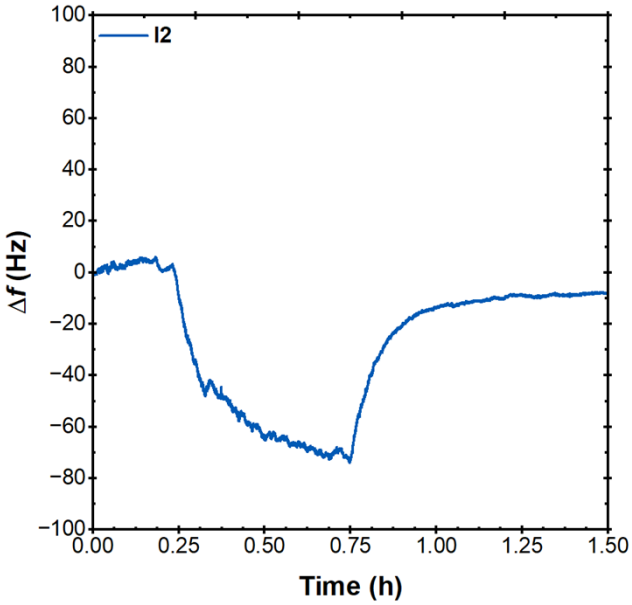

Figure S104. QCM data following the adsorption of DMMP in **I2**.

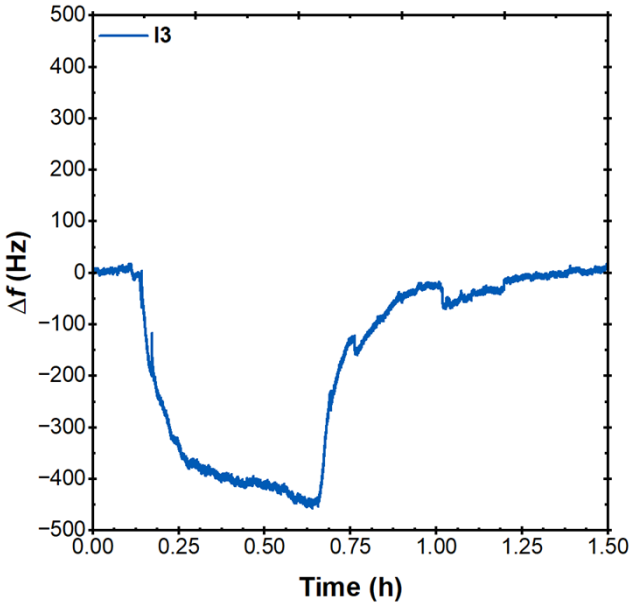

Figure S105. QCM data following the adsorption of DMMP in **I3**.

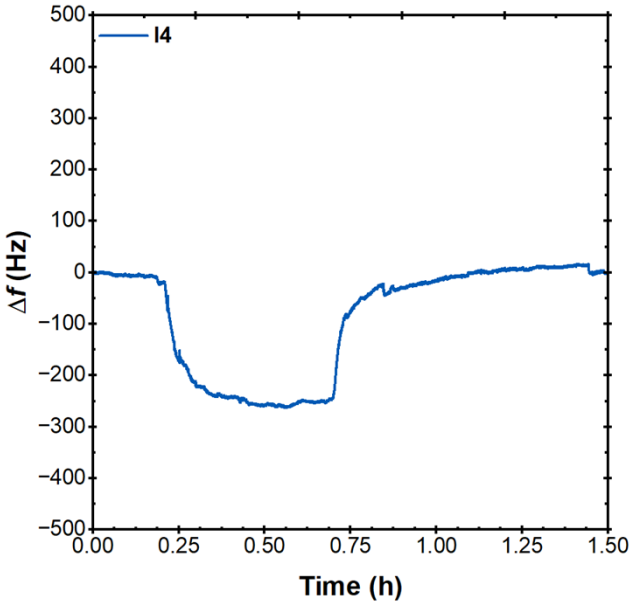

Figure S106. QCM data following the adsorption of DMMP in **I4**.

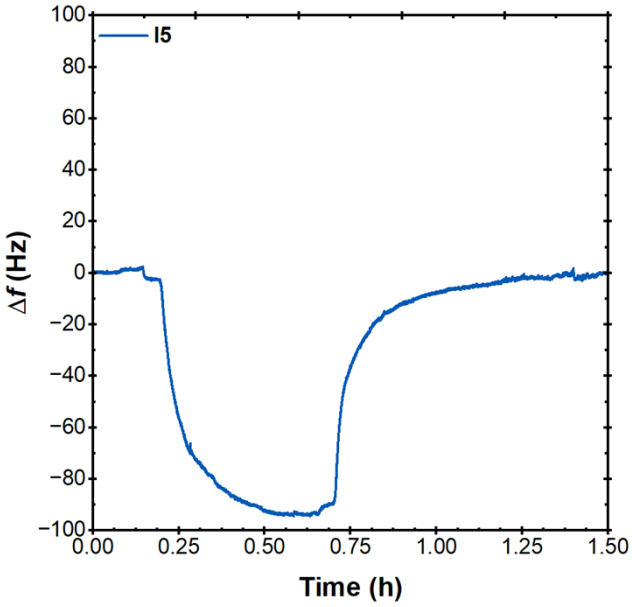

Figure S107. QCM data following the adsorption of DMMP in **I5**.

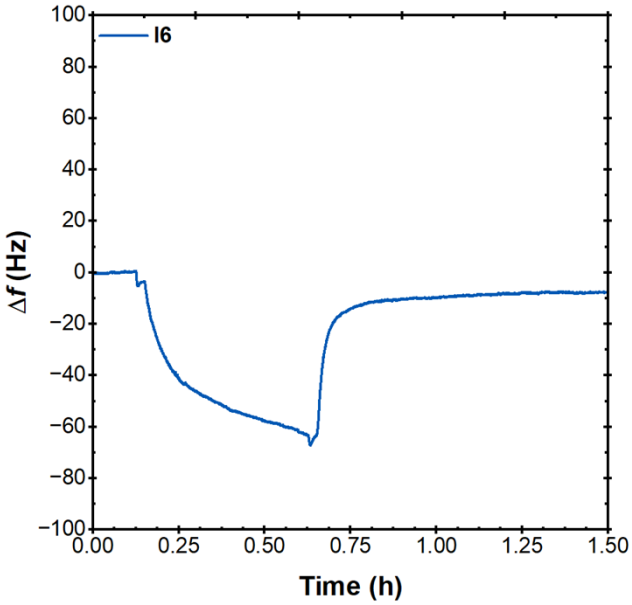

Figure S108. QCM data following the adsorption of DMMP in **I6**.

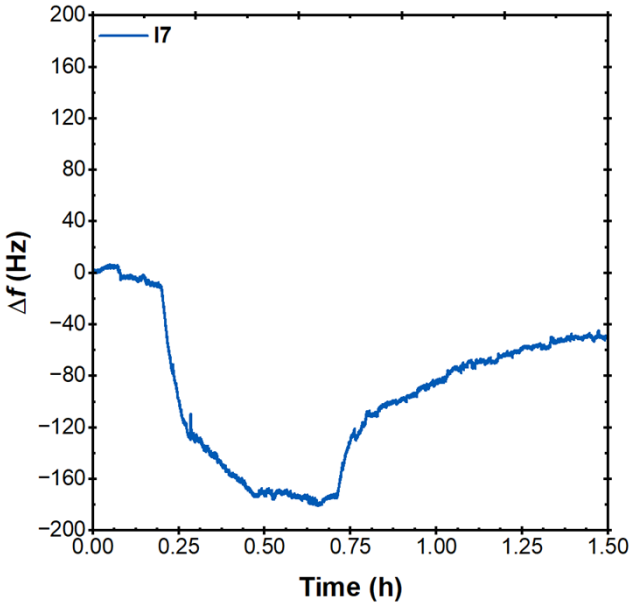

Figure S109. QCM data following the adsorption of DMMP in **I7**.

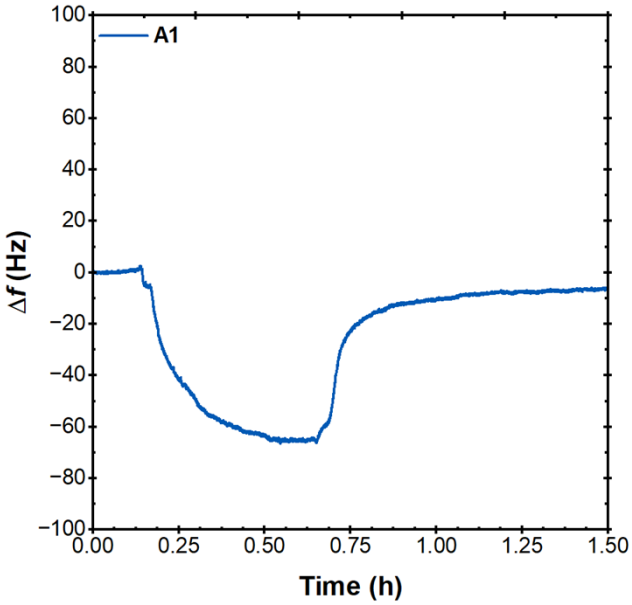

Figure S110. QCM data following the adsorption of DMMP in **A1**.

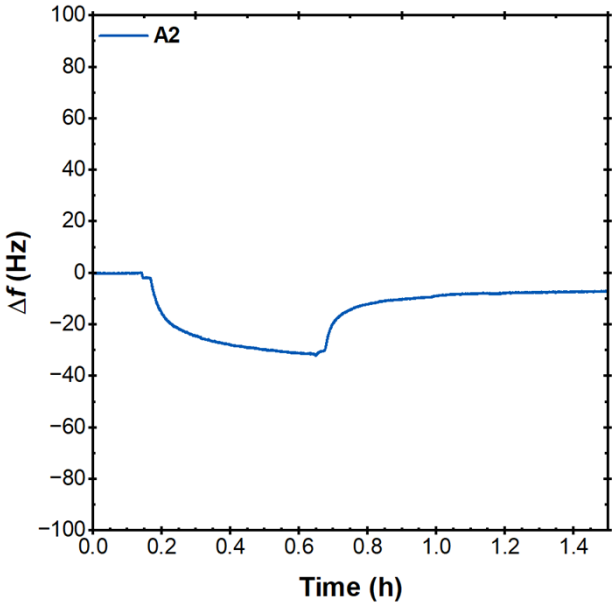

Figure S111. QCM data following the adsorption of DMMP in **A2**.

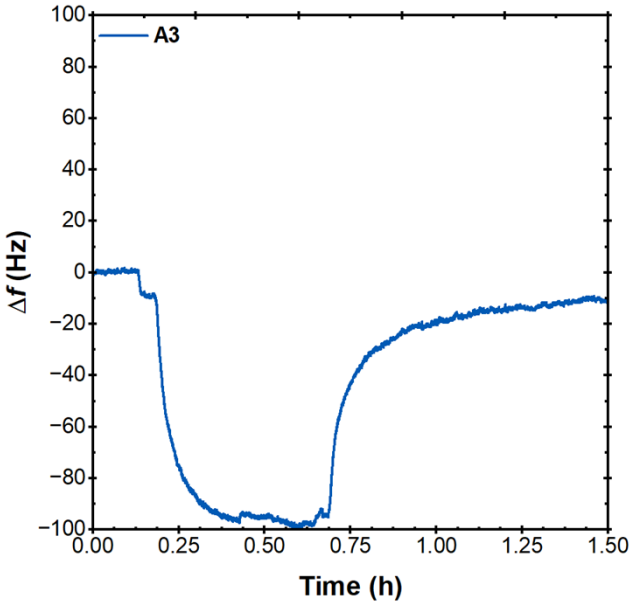

Figure S112. QCM data following the adsorption of DMMP in **A3**.

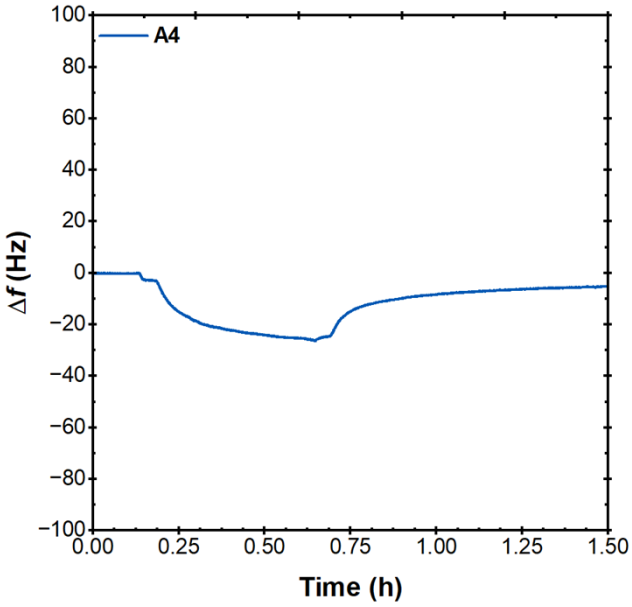

Figure S113. QCM data following the adsorption of DMMP in **A4**.

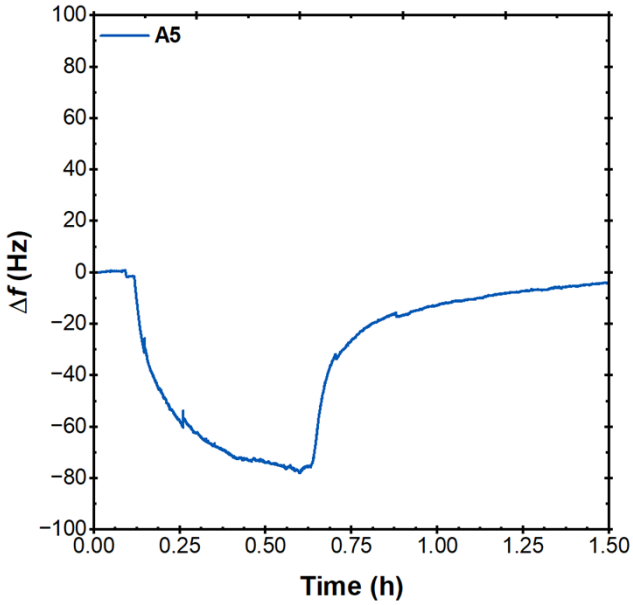

Figure S114. QCM data following the adsorption of DMMP in **A5**.

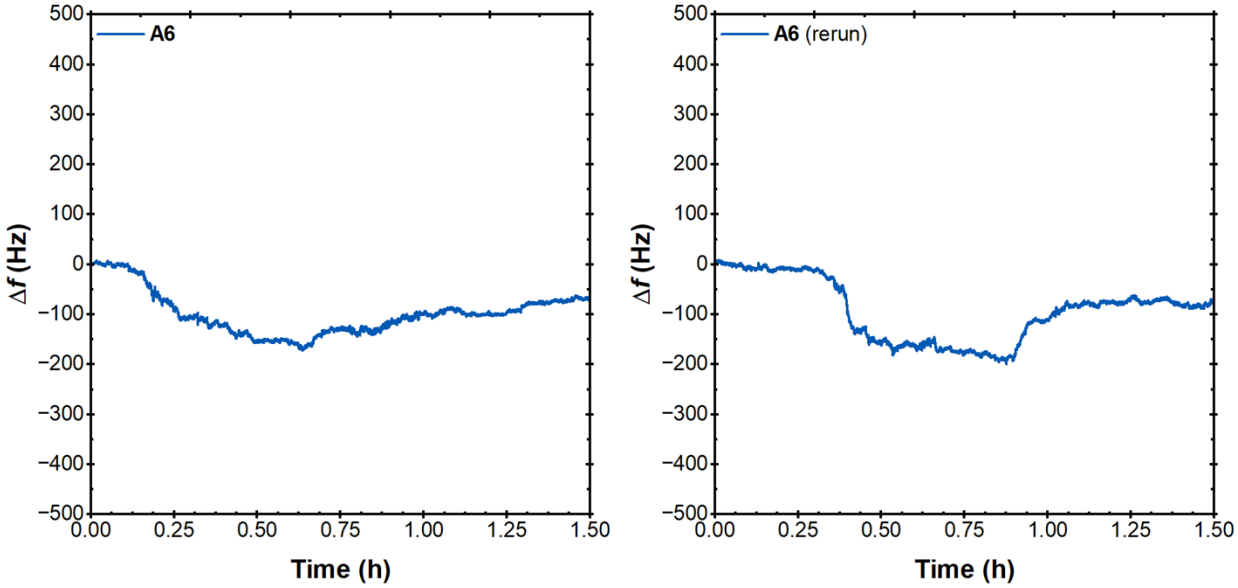

Figure S115. QCM data following the adsorption of DMMP in **A6** (left). Data was recollected on a separate day to confirm reproducibility (right).

Measurement of Henry's Law Binding Constants

QCM sensors (5 MHz) were cleaned by first treating them in an oxygen plasma chamber on a high setting for 10 minutes. The sensors were then placed in a solution of 5:1:1 DI water, 25% aqueous NH_4OH, and 30% H_2O_2. The solution was heated to 75 °C and the sensors allowed to soak for 5 min. The sensors were washed immediately washed with DI water and dried under compressed air. A final treatment in an oxygen plasma chamber was performed on a high setting for 10 minutes, and the sensors were stored in sealed containers until further use.

Prior to coating the sensors, their oscillation frequencies were measured under dry air flow. Coating of the sensors with each MOF was then performed according a modified published literature procedure.[6] Suspensions of each MOF were prepared by sonicating 15 mg mL^{-1} in dimethylformamide for several hours. A small amount (10 μL) was dropped onto each sensor and spin-cast starting at 500 rpm for 4 seconds, then 2000 rpm for 1 min, and finally 300 rpm for 9 min. The coated sensors were dried in a vacuum oven overnight at 120 °C and their oscillation frequencies remeasured to determine the quantity of each MOF deposited. Sensors were then stored in a vacuum oven at 120 °C prior to DMMP exposure experiments. The raw data (change in oscillation frequency, Δf) was converted to mass change (Δm) by use of the modified Saurbrey equation (Eq. 1).[7] A value of 17.7 ng cm^{-2} was used for the mass sensitivity constant (C) of the 5 MHz QCM sensors, and the third harmonic (n=3) was used.

Vapor delivery was achieved by flowing dry air (~10 mL min^{-1}) through a series of bubblers containing DMMP, which was held at 20 °C using a thermostatted water bath. The concentration of the saturated gas stream was confirmed to be ~750 ppm by adsorption to activated carbon traps and gravimetric analysis. The saturated gas stream was then diluted twice prior to being introduced to the QCM sensors. In the first dilution stage, the saturated gas stream was mixed with dry air at a flow rate of ~ 1490 mL min^{-1}, resulting in [DMMP] ~ 5 ppm. This diluted vapor stream was then split, and a stream at 10 mL min^{-1} was diluted again in a second stage with dry air at a flow rate of ~50 – 500 mL min^{-1} to achieve [DMMP] in the ppb range. Prior to every experiment, the flow rate of each gas stream was recorded and used to manually calculate the real-time [DMMP], which is reported in the data below. The QCM sensor signals were finally stabilized under dry air at an equivalent flow rate to that used in the experiment, after which the experiment was commenced by switching to the desired vapor stream. Experiments were run with 4 replicates, where DMMP exposure lasted 5 min followed by 10 min of dry air flow. Throughout the experiment, the temperature of the QCM sensors was maintained at 25 C.

Following completion of the experiment, the mass of sorbent on each sensor, along with the free volume of the MOF determined using N_2 gas adsorption (Table S2), was used to calculate the volume of the sorbent. Along with the quantity of DMMP adsorbed, this value allowed for calculation of the [DMMP] in the sorbent. The value of K_H was calculated at each [DMMP] was then calculated according to Equation 2.

$$K_H = \frac{[DMMP]_{sorbent}}{[DMMP]_{headspace}} \qquad \text{Eq. 2}$$

To obtain the Henry's Law binding constant, a plot of $\log(K_H)$ vs. $[DMMP]_{headspace}$ was then prepared and fit with a linear trend line. The Henry's Law binding constant at infinite dilution was determined from the y-intercept of this plot.

Table S2. MOF free volumes determined from N_2 gas adsorption data

MOF	Free Volume ($cm^3\ g^{-1}$)
UiO-66	0.582
UiO-66-OH	0.201
UiO-66-NH_2	0.467
I1	0.190
I2	0.284
I3	0.228
I4	0.260
I6	0.246
I7	0.218
A1	0.079
A2	0.301
A3	0.127
A4	0.114
A5	0.218
A6	0.078

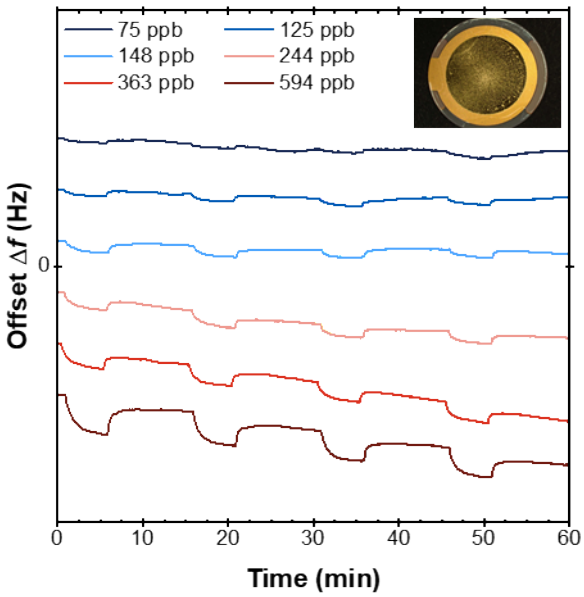

Figure S116. Frequency response curves for UiO-66 exposed to different concentrations of DMMP. The figure inset shows a photograph of the coated sensor used in these experiments.

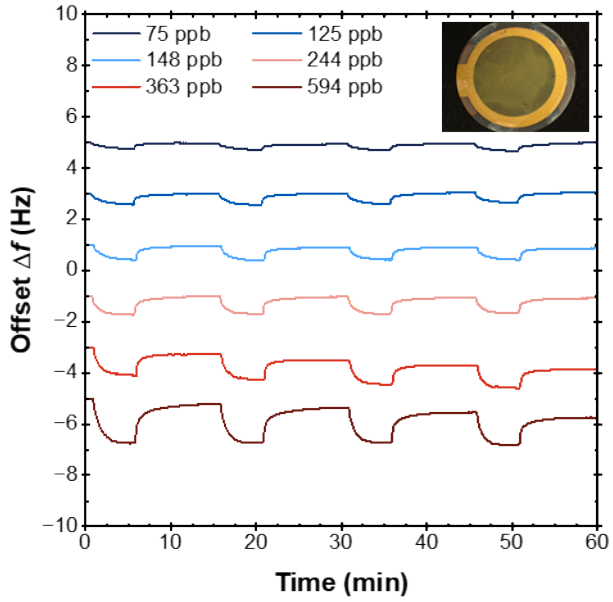

Figure S117. Frequency response curves for UiO-66-OH exposed to different concentrations of DMMP. The figure inset shows a photograph of the coated sensor used in these experiments.

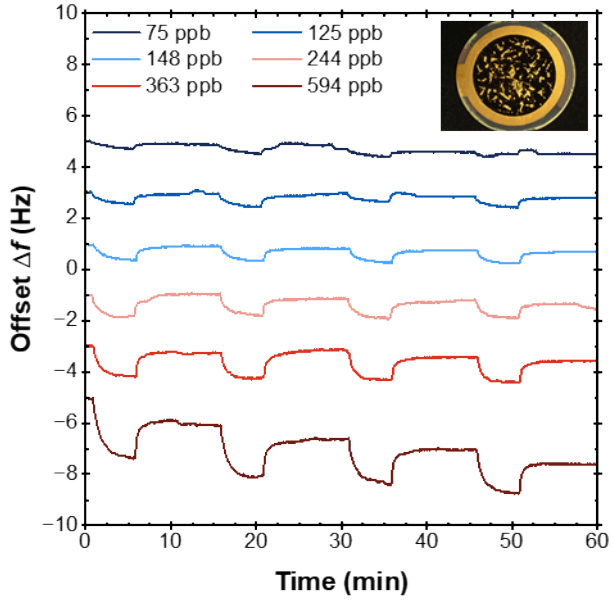

Figure S118. Frequency response curves for UiO-66-NH_2 exposed to different concentrations of DMMP. The figure inset shows a photograph of the coated sensor used in these experiments.

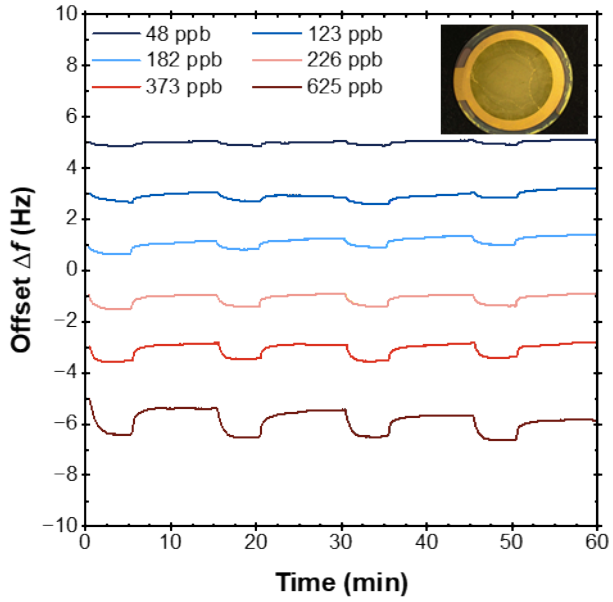

Figure S119. Frequency response curves for **I1** exposed to different concentrations of DMMP. The figure inset shows a photograph of the coated sensor used in these experiments.

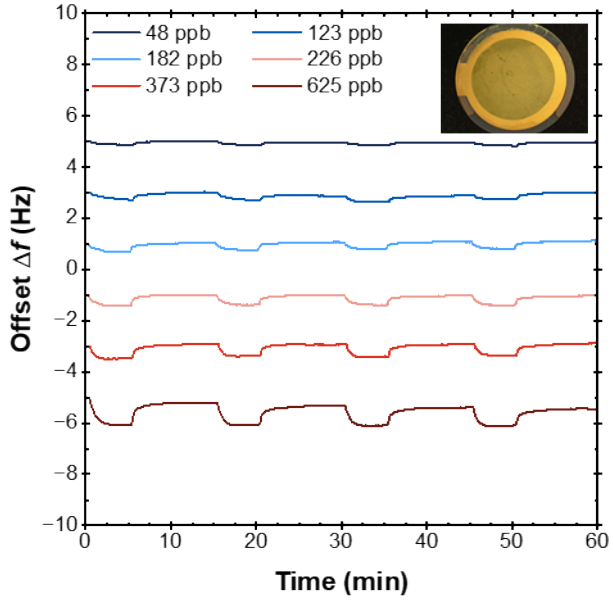

Figure S120. Frequency response curves for **I2** exposed to different concentrations of DMMP. The figure inset shows a photograph of the coated sensor used in these experiments.

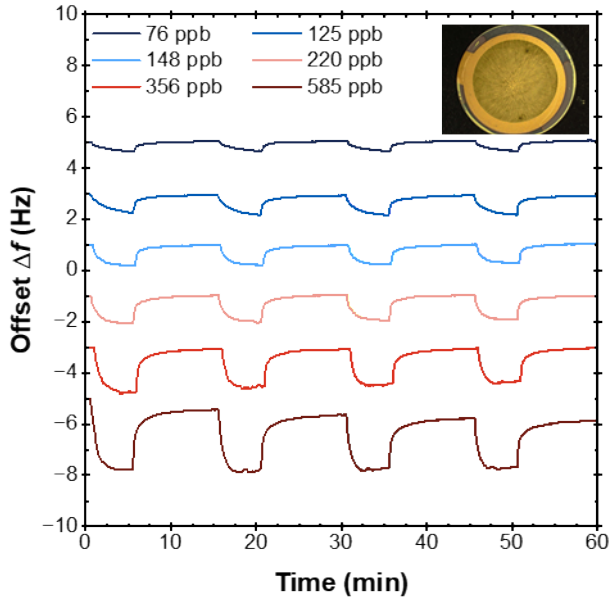

Figure S121. Frequency response curves for **I3** exposed to different concentrations of DMMP. The figure inset shows a photograph of the coated sensor used in these experiments.

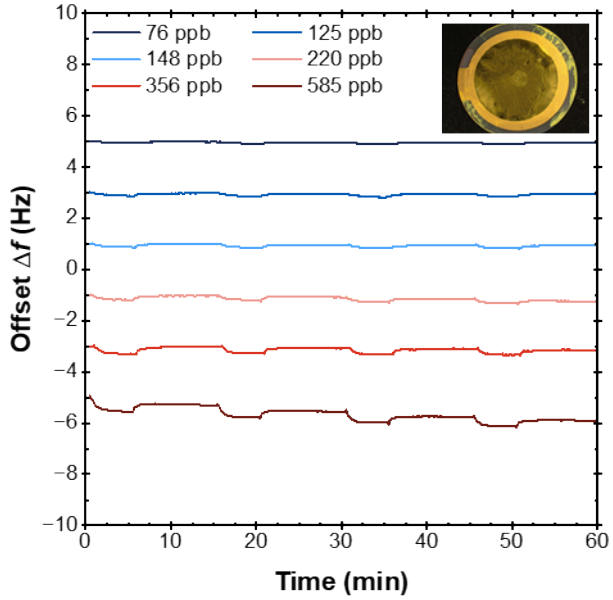

Figure S122. Frequency response curves for **I4** exposed to different concentrations of DMMP. The figure inset shows a photograph of the coated sensor used in these experiments.

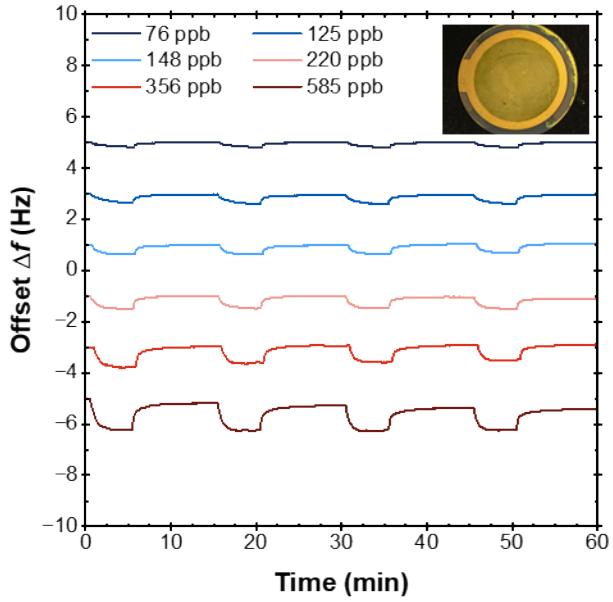

Figure S123. Frequency response curves for **I5** exposed to different concentrations of DMMP. The figure inset shows a photograph of the coated sensor used in these experiments.

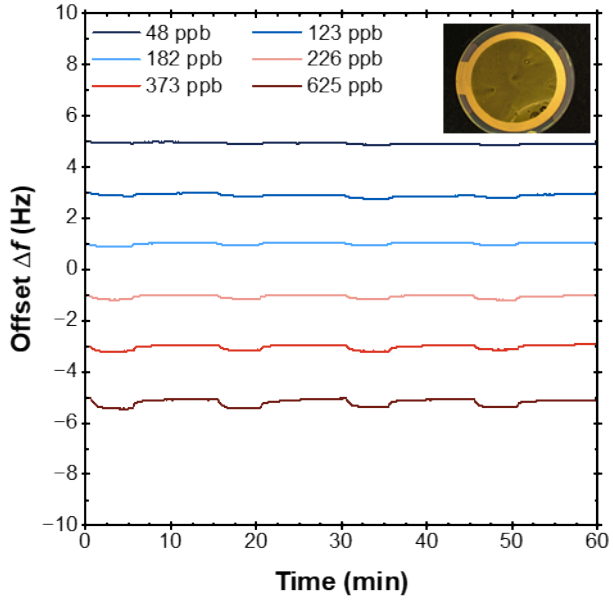

Figure S124. Frequency response curves for **I6** exposed to different concentrations of DMMP. The figure inset shows a photograph of the coated sensor used in these experiments.

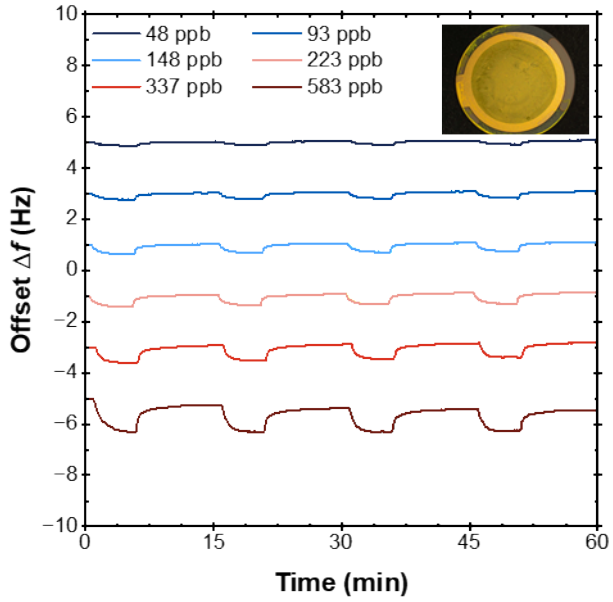

Figure S125. Frequency response curves for **I7** exposed to different concentrations of DMMP. The figure inset shows a photograph of the coated sensor used in these experiments.

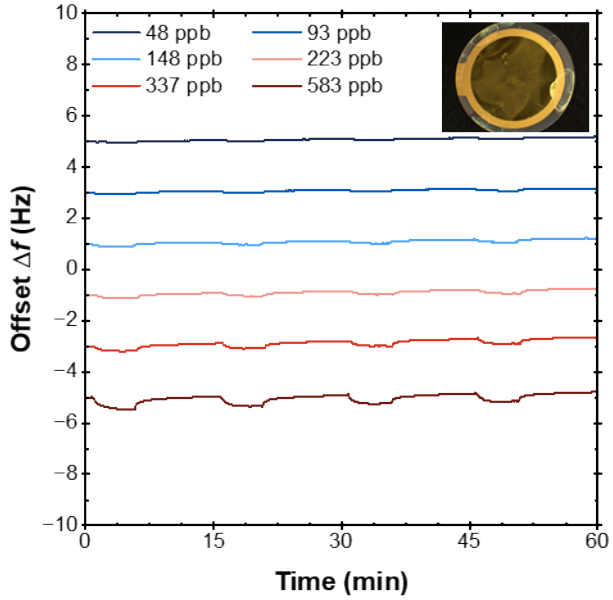

Figure S126. Frequency response curves for **A1** exposed to different concentrations of DMMP. The figure inset shows a photograph of the coated sensor used in these experiments.

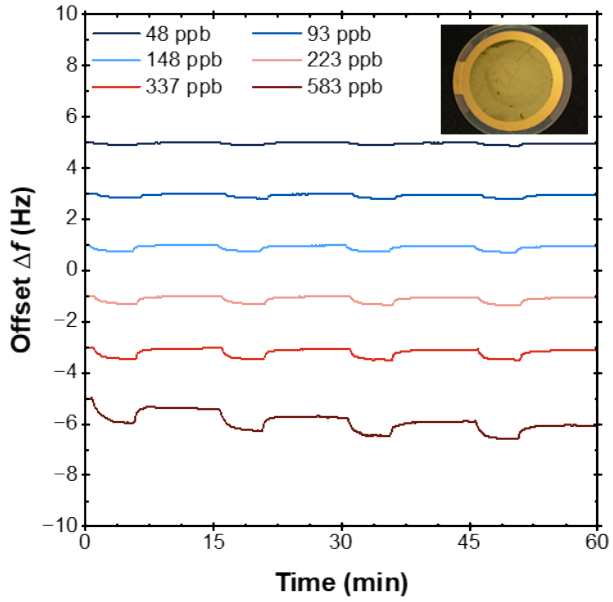

Figure S127. Frequency response curves for **A2** exposed to different concentrations of DMMP. The figure inset shows a photograph of the coated sensor used in these experiments.

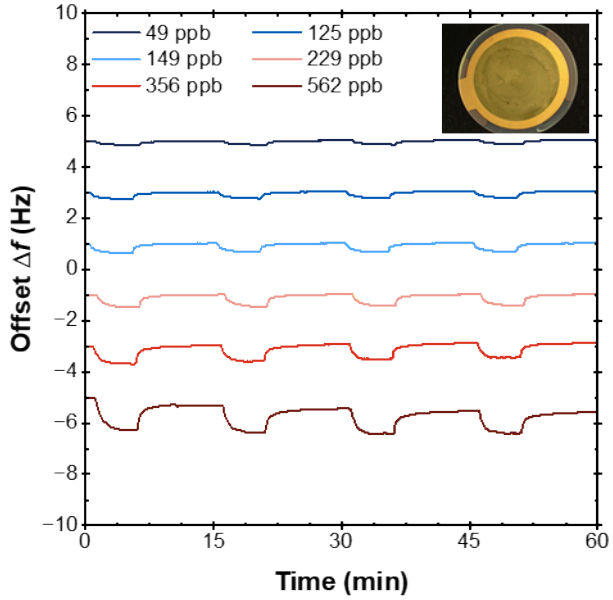

Figure S128. Frequency response curves for **A3** exposed to different concentrations of DMMP. The figure inset shows a photograph of the coated sensor used in these experiments.

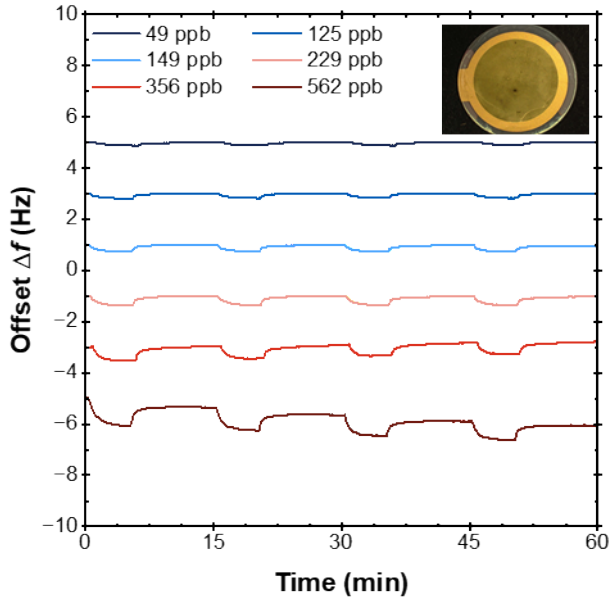

Figure S129. Frequency response curves for **A4** exposed to different concentrations of DMMP. The figure inset shows a photograph of the coated sensor used in these experiments.

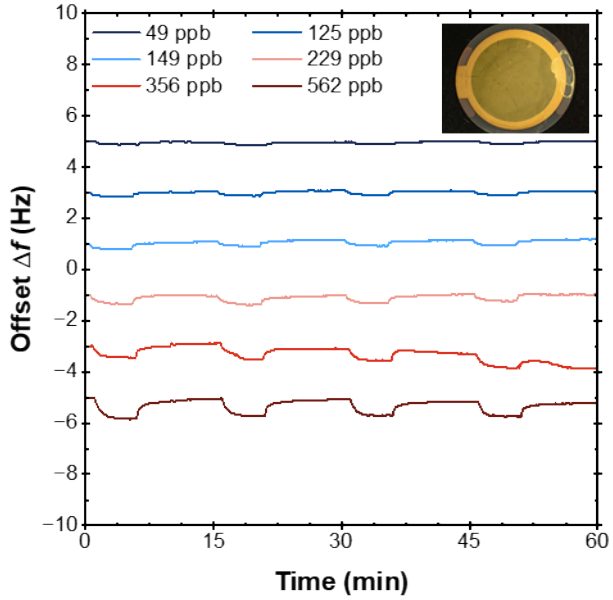

Figure S130. Frequency response curves for **A5** exposed to different concentrations of DMMP. The figure inset shows a photograph of the coated sensor used in these experiments.

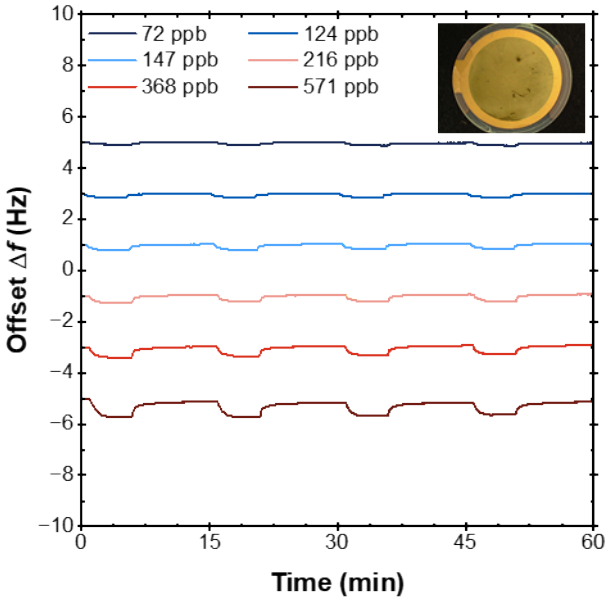

Figure S131. Frequency response curves for **A6** exposed to different concentrations of DMMP. The figure inset shows a photograph of the coated sensor used in these experiments.

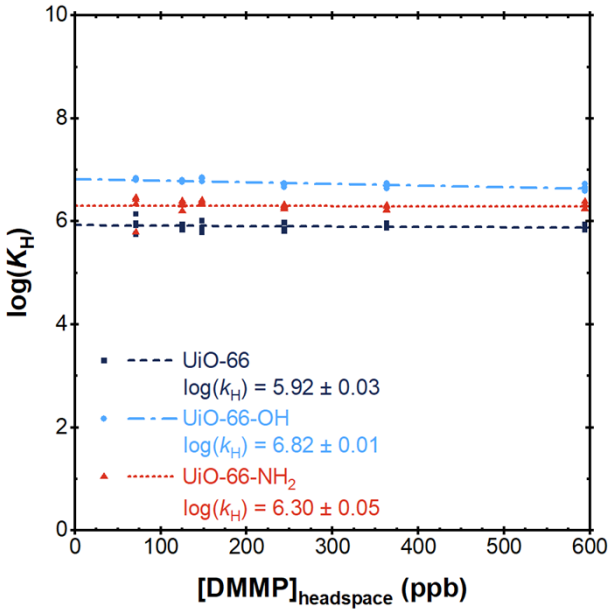

Figure S132. Henry's Law plots for UiO-66, UiO-66-OH, and UiO-66-NH_2 with DMMP.

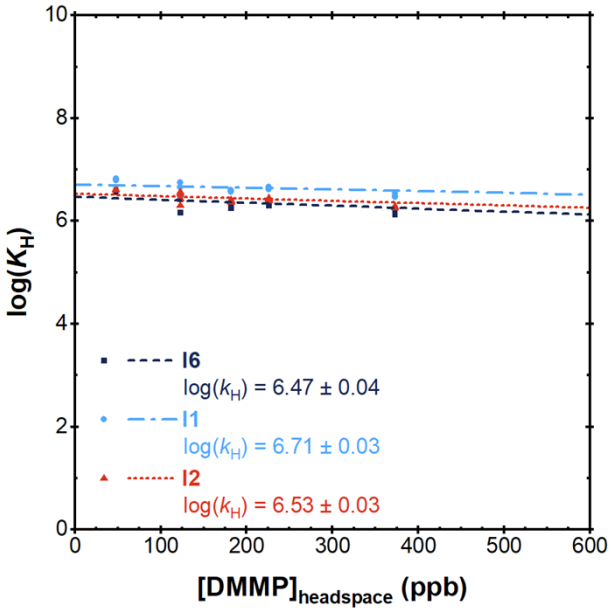

Figure S133. Henry's Law plots for **I6**, **I1**, and **I2** with DMMP.

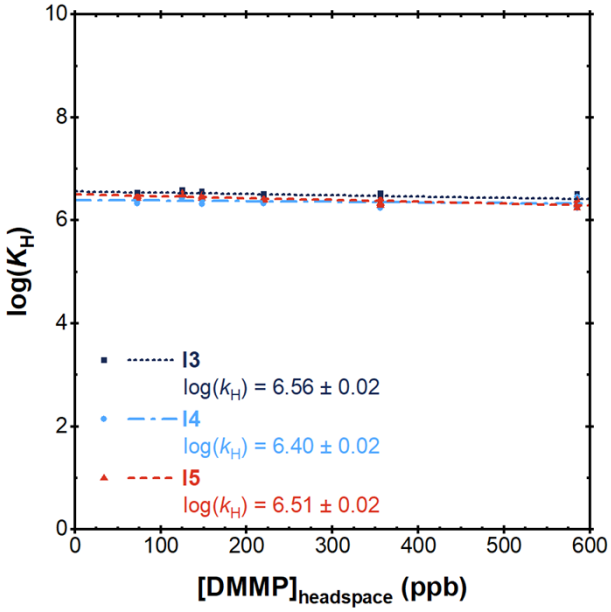

Figure S134. Henry's Law plots for **I3**, **I4**, and **I5** with DMMP.

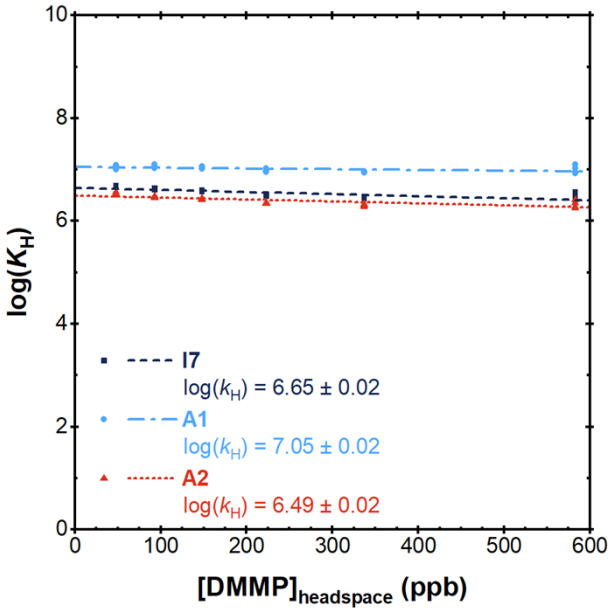

Figure S135. Henry's Law plots for **I7**, **A1**, and **A2** with DMMP.

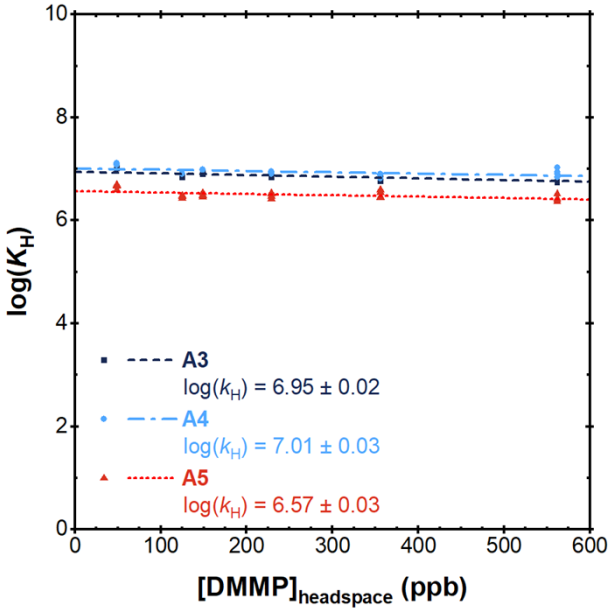

Figure S136. Henry's Law plots for **A3**, **A4**, and **A5** with DMMP.

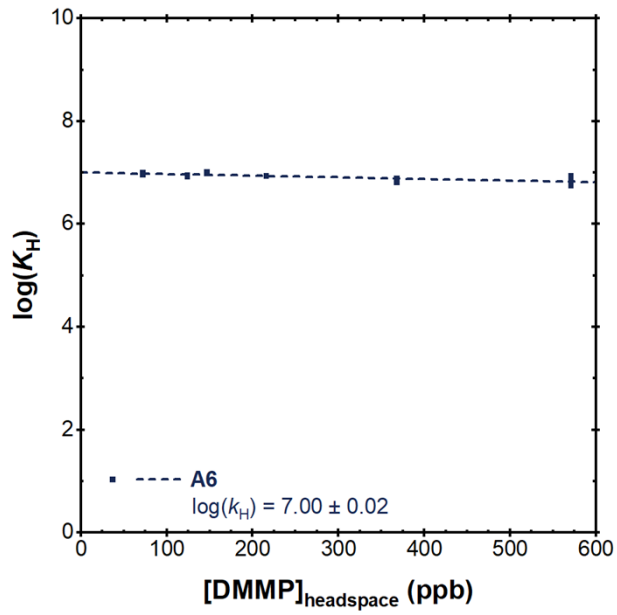

Figure S137. Henry's Law plot for **A6** with DMMP.

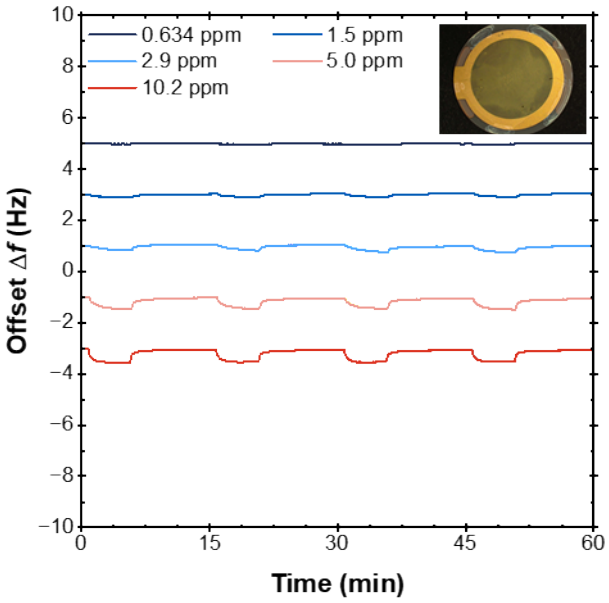

Figure S138. Frequency response curves for UiO-66-OH exposed to different concentrations of toluene. The figure inset shows a photograph of the coated sensor used in these experiments.

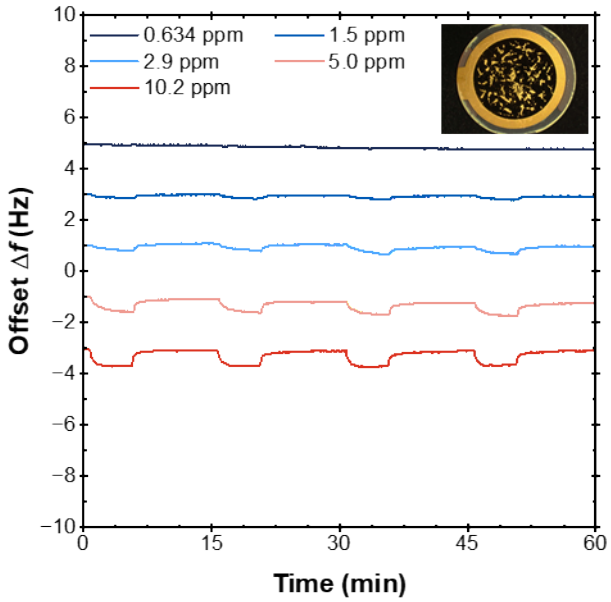

Figure S139. Frequency response curves for UiO-66-NH_2 exposed to different concentrations of toluene. The figure inset shows a photograph of the coated sensor used in these experiments.

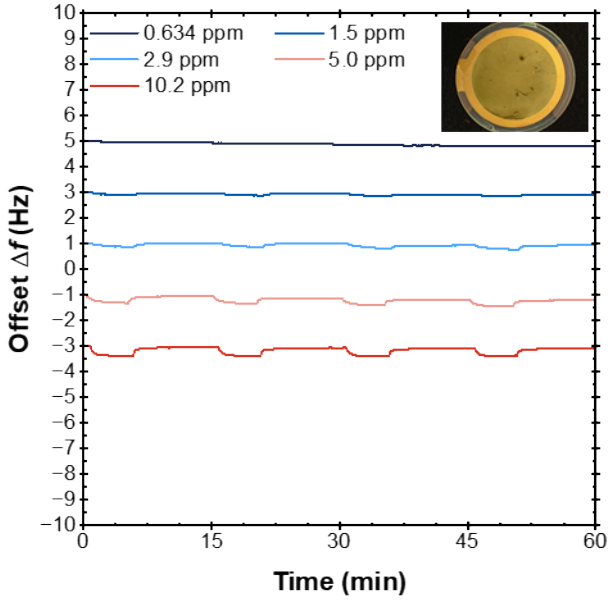

Figure S140. Frequency response curves for **A6** exposed to different concentrations of toluene. The figure inset shows a photograph of the coated sensor used in these experiments.

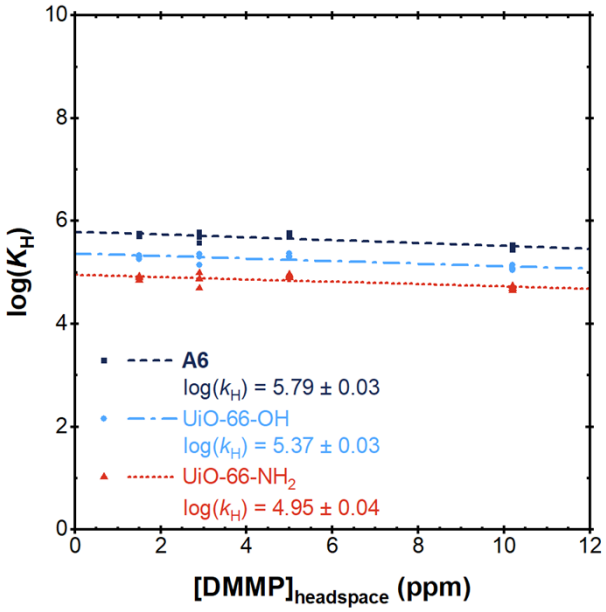

Figure S141. Henry's Law plot for UiO-66-OH, UiO-66-NH_2, and **A6** with toluene.

4. References

1. J. H. Cavka, S. Jakobsen, U. Olsbye, N. Guillou, C. Lamberti, S. Bordiga, K. P. A. Lillerud, A new zirconium inorganic building brick forming metal organic frameworks with exceptional stability, *J. Am. Chem. Soc.* 2008, **130**, 13850–13851.
2. M. J. Ingleson, J. P. Barrio, J.-B. Guilbaud, Y. Z. Khimyak, M. J. Rosseinsky, Framework functionalisation triggers metal complex binding, *Chem. Commun.* 2008, 2680.
3. C. J. Doonan, W. Morris, H. Furukawa, O. M. Yaghi, Isoreticular metalation of metal−organic frameworks, *J. Am. Chem. Soc.* 2009, **131**, 9492–9493.
4. J. S. Costa, P. Gamez, C. A. Black, O. Roubeau, S. J. Teat, J. Reedijk, Chemical modification of a bridging ligand inside a metal–organic framework while maintaining the 3D structure, *Eur. J. Inorg. Chem.* 2008, **2008**, 1551–1554.
5. Z. M. Soilis, T. H. Choi, J. Brennan, R. R. Frontiera, J. K. Johnson, N. L. Rosi, Ligand chromophore modification approach for predictive incremental tuning of metal–organic framework color, Chem. Mater. 2023, 35, 7741–7749.
6. S. Gaikwad, Y. Kim, R. Gaikwad, S. Han, Enhanced VOC adsorption capacity on MOF thin layer with reduced particle size by cryogrinding and microwave method, *J. Environ. Chem. Eng.* 2022, **10**, 107567.
7. G. Sauerbrey, Verwendung von Schwingquarzen zur Wägung dünner Schichten und zur Mikrowägung. *Zeitschrift für Physik* 1959, **155**, 206–222.